THE UNIVERSITY OF CHICAGO

MODELING AND CREATING CAVITY RYDBERG POLARITONS FOR ACHIEVING STRONGLY CORRELATED PHOTONIC MATERIALS

A DISSERTATION SUBMITTED TO
THE FACULTY OF THE DIVISION OF THE PHYSICAL SCIENCES
IN CANDIDACY FOR THE DEGREE OF
DOCTOR OF PHILOSOPHY

DEPARTMENT OF PHYSICS

BY
ALEXANDROS GEORGAKOPOULOS

CHICAGO, ILLINOIS
DECEMBER 2018

To my parents and Anita

TABLE OF CONTENTS

LIST OF FIGURES

LIST OF TABLES

ACKNOWLEDGMENTS

Working with Jon has been an absolute pleasure. He has taught me so much, not only about physics but how to be a better scientist and communicator. His enthusiasm and persistence have been a great inspiration to me since day one in lab and I can only hope i picked up even a small fraction of that for the rest of my life. I am definitely lucky that we both chose to work at the University of Chicago.

I have learned as much from working with everyone else in lab as I have from Jon. Ariel Sommer, our first postdoc, is a fantastic scientist in every sense of the word. He has a deep understanding of physics and was always incredibly clear while explaining various topics, from physics to making circuits, to us. Even though he just started his career in academia, I know he will do great things. Albert Ryou is, along with me, the first of Jon's students. We quickly ended up focusing on different aspects of the experiments but still interacted constantly. The vast majority of my early cavity knowledge came from Albert and I can say with the utmost certainty that he probably is the only person more persistent than Jon; he never gave up when confronted with any obstacle and kept going at it until he has it all figured out. Ningyuan Jia has done too much around the lab to mention here. He is an extremely hard-working person and, when he finally opened up to the rest of us, a great guy to spend time in lab with. Nathan Schine was in some sense the successor to Albert: he worked a lot on our optical resonators and extended our work into really exciting territory. Talking to him has always been extremely helpful in terms of my work in lab but more than that, Nathan always has an abundance of random, interesting facts to share. The latest additions to our experiment have not been there as long but they are as important. Our new postdoc Logan Clark, who I am pretty sure has claimed our experiment as his own by now, Claire Baum and TianXing Zheng are working extremely hard on the existing setup and constantly making improvements. I have no doubt that they will perform great physics in the coming years.

Clai Owens, Mark Stone and Aziza Suleymanzande might not be part of the cavity Rydberg polariton experiment but they are as much a part of the Simon lab as anyone else. I have spent countless hours talking to them, both about physics and anything else, and I can say they have only made a better physicist and person.

Over the years, the Simon lab has had some extraordinary undergrads at work. I want to thank Aaron Krahn, Michelle Chalupnik, Aman LaChappelle, Graham Greve and Michael Cervia for making it even more fun to be in lab. Special thanks goes to Tahoe Scrader; he was my mentee and in teaching him, I ended up learning a lot myself, not just about physics but also how to be a better teacher.

Finally, I want to thank my family for always supporting me in my very long pursuit of physics and Anita Yuen for putting up with me over the past three years.

ABSTRACT

Designing materials with specific properties has been a long-time goal of the physics community. Optical photons have recently emerged as a promising candidate for such metamaterials due to their fast dynamics and available manipulation toolkit. In conjunction with carefully engineered optical resonators, it is possible to precisely control the properties of individual photons through the resonator Hamiltonian. The only missing ingredient to photonic materials is strong photon-photon interactions.

This thesis describes the characterization of cavity Rydberg polaritons and the emergence of strong interactions in such a system. Electromagnetically induced transparency (EIT) is used to create quasiparticles that inherit the properties of both photons and Rydberg atoms: fast dynamics and trapping from the photons and long-range dipole-dipole interactions from the Rydberg atoms. The emergent polaritonic properties are characterized and controlled through the dark-state rotation angle and agree very well with theoretical predictions.

We then expand upon this understanding of polaritons by putting them inside a zero-dimensional quantum dot. Confining the polaritons in such an object allows for strong interparticle interactions to manifest. We observe these interactions through the temporal auto-correlation intensity function $g_2(\tau)$ and verify the dimensionality of the quantum dot itself by measure the polariton Rabi oscillations.

With the experimental demonstration of strong photonic interactions, a complete understanding of Rydberg atoms and polaritons is needed to allow for better control of the system. To this effect, the properties of Rydberg atoms are analytically and numerically understood and the full formalism needed to describe resonator Rydberg polaritons is developed, along with their interactions and various sources of decoherence. Furthermore, a renormalized effective field theory for single mode cavities is developed and tested against full numerical models, paving the way for the simulation of the physical phenomena of manybody states in multi-mode cavities.

Strongly interacting cavity polaritons can be utilized in quantum gate and repeater protocols for quantum information processing. Furthermore, combining the experimental and theoretical work here with non-planar resonators presents a clear path to non-trivial topological synthetic materials and strongly correlated quantum states.

CHAPTER 1

INTRODUCTION

Quantum mechanics changed how we view and understand the world. Introducing particle and wave duality, it ushered in a new era of physics, predicting and explaining phenomena such as superconductivity [1] and quantum phase transitions [2, 3], that are still cutting edge research topics.

At the same time, quantum mechanics laid the foundation for efforts in creating new, artificial phases of matter. The culmination of this experimental push was the demonstration of the Bose-Einstein condensate (BEC) [4, 5], a many particle ground state matter wave.

The invention of the laser [6] has only added to the vast and unexplored areas of quantum physics. The direct manipulation of the optical properties of materials through the electric field of light [7] has paved the way for more exotic forms of photon manipulation such as squeezed states of light [8] and entanglement between photons [9].

Control over photons has only grown over the past decades as the understanding of optical resonators has advanced. Starting with the ability to engineer mode spacing and degeneracies [10], more exotic resonator geometries allow us to imbue photons with mass [11], creating a direct analogy to a quantum harmonic oscillator, and to introduce effective magnetic fields [12].

A direct result of this experimental effort has been the use of photons as building blocks of "matter", creating the field of synthentic photonic materials. Photons in optical cavities have been observed to thermalize, creating a photonic BEC [13, 14] and have been proposed as a platform to simulate glassy physics [15]. Other efforts have focused on emergent crystallinity through long-range interactions [16, 17] and optomechanics [18]. Despite all this work, photon-photon interactions have remained elusive and are the main obstacle to true photonic materials.

A parallel effort in quantum simulation and synthetic materials is through the use of

ultracold atoms. Various tools exist for manipulating atoms, such as lattice trapping [19] and tuning [20] and Feschbach resonances [21]. Furthermore, ultracold atoms exhibit strong interactions, excellent coherence and high-fidelity readout [22–24]. Ions possess even stronger interactions and are ripe for quantum computing; work in ion traps has demonstrated up to six particle entanglement [25].

1.1 Synthetic materials with polaritons

Our group chose to take a combined approach, using the advantages of both cold atoms and photons, while at the same time allowing for strong photon-photon interactions. Our work on topological metamaterials utilizes a particle having the character of both matter and light: the polariton. Polaritons have to behave as both of their constituent particles; as a result, we have to access to all the tools available to manipulate ultracold atoms and photons. Long-range interactions are imbued on these particles by coupling photons to Rydberg-level excited atoms. Rydberg atoms, due to their single excited valence electron, exhibit strong interactions that have already been demonstrated to be a perfect method of creating quantum gates [26] and accessing novel phase transitions [27].

Rydberg polaritons, and their interactions, have been experimentally observed in free-space [28–31]. These 1D free space systems are rich in physics, exhibiting exotic effects such as different longitudinal and transverse (not necessarily real) masses [32] and bound photon states [33].

Our system builds on such experimental efforts by combining Rydberg polaritons with optical resonators. The resulting cavity Rydberg polariton has a photonic component that has to obey any resonator symmetry and can only live in the supported modes. As a result, we can easily chose to confine the particles down to 0D [34]: a single resonator mode restricts transverse motion and slicing along the longitudinal axis reduces the last degree of freedom. At the same time, we can choose to allow for multiple degenerate resonator modes; this

creates a manybody regime suitable for quantum fluids and fractional quantum Hall effects.

1.2 Overview of the thesis

This thesis is divided into a few parts to create a natural progression for the results presented. Before the experiment is discussed, the various properties of Rydberg atoms are reviewed and numerically modeled. Combining this with the full formalism of cavity Rydberg polaritons allows us to understand, design and predict the relevant parameters and behavior of the system. The experimental setup, along with the sample preparation, is then discussed. Finally, I present our experimental results, consisting of two generations of optical resonators. The first one allowed us to observe cavity Rydberg polaritons and understand their quantitative behavior, limited by the polariton decoherence produced by stray electric fields. The second, more well-designed and sophisticated, version proved fruitful for the observation of strong interactions, paving the way for future work in manybody physics.

Chapter 2 introduces Rydberg atoms and all their properties that make them both great and problematic to work with. Their wavefunctions and similarities to hydrogenic atoms are introduced, since that lone outermost electron is the source of their infamy. Their large dipole matrix elements and sensitivity to electric fields are discussed and numerically computed. Then I introduce the long-range interactions of Rydberg atoms. While the off-resonant dipole interaction is the relevant quantity throughout my experimental work, I also briefly discuss the resonant C_3 interactions and analytically compute it and its transition to the off-resonant case.

Chapter 3 introduces cavity Rydberg polaritons. Starting with the photonic Hamiltonian, I will proceed to show the Rydberg-dressed states and how they retain characteristics of both of their constituents. Their polaritonic operators will be introduced and then interactions will be formalized in both the weakly- and strongly-interacting regime. For the case of strong interactions specifically, I will talk about a renormalized effective field theory. This

is of huge practical importance as it allows for extremely fast theoretical predictions and can be easily extended to account for many modes and many particles without a significant increase in computational time. Finally, I compute the effect of atomic motion on cavity Rydberg polaritons and discuss the regimes where each of these decoherence channels might be important.

Chapter 4 is about the experimental setup. It describes the vacuum system we have built and the cavity design, along with the constraints and design parameters it had to satisfy. After that, the various components of the laser setup are discussed. Finally, I go over the necessary steps for preparing our atomic sample, such as trapping and cooling, transporting and slicing.

Chapter 5 is a collection of our first experimental results dealing with cavity Rydberg polaritons. I discuss what the expected cavity transmission should look like and why and then go on to explain how we probed the behavior of the created polaritons and their dependence on the various tuning knobs we can control. Next, I talk about our first major obstacle regarding our quasiparticles: stray electric fields. I present our experimentally observed broadening and provide a theoretical basis for it. Lastly, I briefly discuss two-mode EIT as a gateway to future resonator designs and physics.

Chapter 6 presents the most exciting results of our experiment. By realizing a zero-dimensional quantum dot, which means confining the polaritons transversely, by using a single cavity mode, and longitudinally, by slicing the atomic cloud, and forcing them to live within a single blockade volume, strong interactions between the quasiparticles can be observed. Furthermore, I present data that confirms that the quantum dot is indeed a 0D object; this is done by observing tunnelling between zero and one particles at increasing probe powers. The section concludes by discussing the directions available for the experiment now that strong interactions have been achieved.

Section 7 summarizes the thesis and provides an outlook for future experimental work.

The references follow.

CHAPTER 2

RYDBERG ATOMS

The Rydberg series was discovered as an empirical explanation to the spectral lines of atomic hydrogen and allowed for the binding energy to be written as [35]:

$$W = -\frac{\mathrm{Ry}}{n^2},$$

where Ry is a fitting parameter and n is an integer. Shortly after, the development of the Bohr model [36] showed that Ry was in fact not just a fitting parameter but could be computed from fundamental constants:

$$\mathrm{Ry} = Z^2 \frac{m_e e^4}{8\epsilon_0^2 \hbar^2}.$$

At the same time, n in the binding energy formula was understood as the principal quantum number. Scaling laws in terms of n were derived from the Bohr model for various atomic properties; these were later verified by the emerging quantum mechanics formalism [37].

The most striking property of Rydberg atoms is their large orbital radius, and correspondingly large matrix elements; they both scale as n^2. As a result of this single valence electron orbiting the nucleus at such a large distance, Rydberg atoms exhibit a tremendous response to electric fields and can support long-range dipole-dipole interactions even on a μm scale. Table 2.1 reports the scaling of various properties for Rydberg atoms.

Binding energy W	n^{-2}
Orbital radius	n^2
Lifetime	n^3
Energy spacing	n^{-3}
Scalar polarizability	n^7
Interaction Coefficient C_6	$n^{11/2}$

Table 2.1: **Scaling properties of Rydberg atoms** [38].

2.1 Alkali metal Rydberg states

Alkali metal atoms are similar to hydrogen; a single valence electron orbits the nucleus in a $1/r$ Coulomb potential. Unlike a hydrogen atom however, many more electrons also orbit the core at shorter radii; as a result, the outermost electron typically sees a screened nuclear charge. Low angular momentum states ($l < 4$) deviate even further from the simple hydrogenic model: the valence electron orbit is highly elliptical and can penetrate the inner electron shells. The valence electron is now exposed to the unscreened nuclear charge on one side and the Coulomb repulsion of the inner electrons on the other side and experiences a very different core potential at short distances. At the same time, the closed shell electrons can polarized by the trip of the valence electron. These two effects combined increase the binding energy of low l Rydberg states, relative to the corresponding hydrogenic states. The alkali metal binding energy can be expressed as:

$$W = -\frac{\mathrm{Ry}}{(n - \delta_{nlj})^2},$$

where δ_{nlj} is the quantum defect. We can now write an effective principal quantum number $n^* = n - \delta_{nlj}$ for alkali Rydberg states; this new principal quantum number simply replaces n in the scaling laws presented in Table 2.1.

The values of the various quantum defects for Rb have been obtained through spectro-

scopic measurements [39, 40] and can be calculated through the formula:

$$\delta_{nlj} = \delta_0 + \frac{\delta_2}{(n-\delta_0)^2} + \frac{\delta_4}{(n-\delta_0)^4} + \ldots, \tag{2.1.1}$$

where δ_i depends on both l and j. The quantum defects are the largest for S Ryderg states, as these states penetrate the core the most. As l increases, the quantum defects get correspondingly smaller; any state with $l \geq 4$ has zero quantum defect values and is hydrogenic in the sense that it experiences a Coulombic core potential.

2.2 Rydberg wavefunctions

Schrödinger's equation, in atomic units (a.u.) for the valence electron of a hydrogenic atom is given by:

$$\left[-\frac{1}{2\mu}\nabla^2 + V(r)\right]\Psi(r,\theta,\phi) = W\Psi(r,\theta,\phi),$$

where μ is the reduced electron mass, $V(r)$ is the core potential and r, θ, ϕ are spherical coordinates. The wavefunction Ψ is separable since $V(r)$ only has radial dependence and we can write it as $\Psi(r,\theta,\phi) = R(r)Y_l^{m_l}(\theta,\phi)$. $Y_l^{m_l}(\theta,\phi)$ is a spherical harmonic that depends only on the angular momentum of the Rydberg state and its projection along the quantization axis m_l. The above differential equation can now be rewritten just for the radial part of the wavefunction:

$$\left[-\frac{1}{2\mu}\left(\frac{\mathrm{d}^2}{\mathrm{d}r^2} + \frac{2}{r}\frac{\mathrm{d}}{\mathrm{d}r}\right) + \frac{l(l+1)}{2\mu r^2} + V(r)\right]R(r) = WR(r). \tag{2.2.1}$$

2.2.1 Core model potential

As mentioned in Section 2.1, alkali metal Rydberg atoms typically experience an angular momentum dependent core potential. This means that $V(r)$ cannot be simply a $1/r$ potential and has to be modified accordingly. Instead of a Coulomb potential, we will use a modified core potential [41] that accounts for core penetration and closed shell electron polarization:

$$V_c(r) = -\frac{Z_{nl}(r)}{r} - \frac{\alpha_c}{2r^4}\left(1 - e^{-(\frac{r}{r_c})^6}\right). \tag{2.2.2}$$

The first term is a modified Coulomb potential that accounts for core penetration through the radial charge $Z_{nl}(r)$ defined as:

$$Z_{nl}(r) = 1 + (Z-1)e^{-\alpha_1 r} - r(\alpha_3 + \alpha_4 r)e^{-\alpha_2 r}. \tag{2.2.3}$$

The second term describes the effect of electron polarization; its strength is captured by the core polarizablity α_c, which increases with the number of electrons present in the core. Values for the above parameters can be found in [41].

Additionally, the spin-orbit coupling potential $V_{so}(r)$, which breaks the degeneracy of l states has to be included [42]:

$$V_{so}(r) = \frac{\alpha^2}{2r^3}\mathbf{L}\cdot\mathbf{S}, \tag{2.2.4}$$

where α is the fine structure constant and $\mathbf{L}\cdot\mathbf{S}=\frac{j(j+1)-s(s+1)-l(l+1)}{2}$. We can now combine these two potentials and write $V(r) = V_c(r) + V_{so}(r)$ in Equation 2.2.1.

2.2.2 Numerical modeling

While analytical solutions for Rydberg wavefunctions exist, they tend to break down at high n. A much better approach is to solve Equation 2.2.1, using the new form of the core potential, numerically. This can be done using Numerov's method [43, 44], which converts the familiar radial wavefunction equation to the much simpler form $\frac{\mathrm{d}^2}{\mathrm{d}x^2}X(x) = g(x)X(x)$. To simplify matters even further, the substitution $x = \ln(r)$ [45] is performed; this allows for numerical solutions decaying to zero at large r to be stable near $r = 0$. To ensure that the wavefunction does not diverge near the core, where the model potential is no longer physically correct, the numerical integration is truncated at $r_i = \sqrt[3]{\alpha_c}$.

Figure 2.1 shows the numerically calculated $15S_{1/2}$ wavefunctions for both Rb and H. The Rb wavefunction decays faster, as a result of the higher binding energy compared to H. An alternative way of thinking about this is that the quantum defects due to the modified core potential in Rb cause phase shifts in the wavefunction.

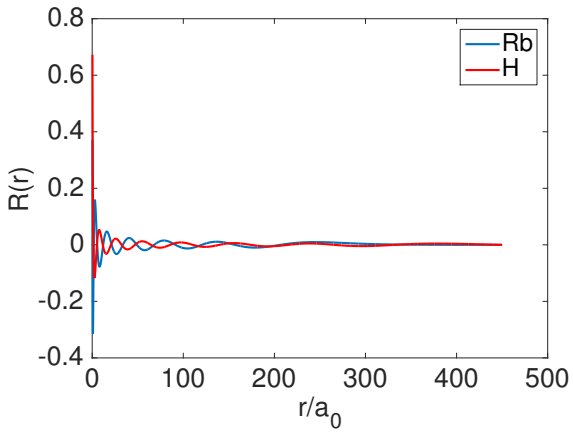

Figure 2.1: **Comparison of the Rb and H wavefunctions**. The computed wavefunctions of both Rb and H are shown for the $15S_{1/2}$ Rydberg state. The blue curve is Rb and the red one is H.

2.3 Dipole Matrix Elements

Matrix dipole elements can be addressed now that a reliable way of computing Rydberg wavefunctions exists. The coupling between two Rydberg states $|nlm_l\rangle$ and $|n'l'm'_l\rangle$ is given by the dipole matrix element $\langle n'l'm'_l|\mu|nlm_l\rangle$, where μ is the electric dipole moment; we can ignore the magnetic dipole coupling, since it is signifantly weaker. Being able to calculate matrix dipole elements is very important as most of the Rydberg atom properties (lifetime, polarizability, interactions) can be related to them.

The electric dipole moment operator is defined as $\vec{\mu} = e\vec{r}\cdot\hat{e}$, where is $\hat{e}$ is a unit vector along the electric field polarization axis. The familiar dipole transitions are π and $\sigma^{\pm}$; moving to spherical coordinates allows us to work in this basis. The dipole operator can be written as:

$$\begin{aligned} \mu_{-1} &= \frac{1}{\sqrt{2}}(\mu_x - i\mu_y), \\ \mu_0 &= \mu_z, \\ \mu_{+1} &= \frac{1}{\sqrt{2}}(\mu_x + i\mu_y), \end{aligned} \tag{2.3.1}$$

where the indices [-1,0,+1] correspond to [σ^+,π,σ^-]. These operators can be related to the spherical harmonic functions by:

$$\mu_q = er\sqrt{\frac{4\pi}{3}}Y_l^q(\theta,\phi).$$

The calculation of dipole matrix elements can further be streamlined by separating them into angular and radial only parts:

$$\langle n'l'm'_l|\mu_q|nlm_l\rangle = (-1)^{l-m_l}\begin{bmatrix} l & 1 & l' \\ -m_l & q & m'_l \end{bmatrix} \times$$
$$(-1)^l\sqrt{(2l+1)(2l'+1)}\begin{bmatrix} l & 1 & l' \\ 0 & 0 & 0 \end{bmatrix}\langle n'l'|er|nl\rangle, \tag{2.3.2}$$

where the brackets denote the Wigner-3j symbol, and $\langle n'l'|er|nl\rangle = e\int_{r_i}^{r_o} \mathrm{d}r r^2 R_{nl}(r) r R_{n'l'}(r)$ [38, 46] is the radial matrix element, representing the spatial overlap of the dipole moment with the two Rydberg wavefunctions.

With the addition of the spin-orbit coupling term V_{so} to the core potential, fine structure becomes important and the degeneracy of the l states is broken and now $j = l + s$ is the new "good" quantum number. Since the electric fields can only couple to the angular momentum of the electron, and not its spin, we need to perform a transformation to an uncoupled basis to allow for the computation of the dipole matrix element:

$$\langle n'l'j'm'_j|\mu_q|nljm_j\rangle = (-1)^{j-m_j+s+j'+1}\sqrt{(2j+1)(2j'+1)(2l+1)(2l'+1)} \times$$
$$\begin{Bmatrix} j & 1 & j' \\ l' & s & l \end{Bmatrix}\begin{bmatrix} j & 1 & j' \\ -m_j & q & m'_j \end{bmatrix}\begin{bmatrix} l & 1 & l' \\ 0 & 0 & 0 \end{bmatrix}\langle n'l'j'|er|nlj\rangle, \tag{2.3.3}$$

where the curly brackets indicate the Wigner-6j symbol.

Hyperfine interactions can further break the degeneracy of the j states, coupling the total angular momentum of the electron, j, to that of the nucleus, i. In the case of Rydberg atoms, any hyperfine splittings are exceedingly small [47] and the fine-structure basis is typically more than sufficient for the purposes of modeling Rydberg properties.

2.3.1 Exciting from the P-state

Up until now, I have detailed the procedure to calculate Rydberg state matrix elements by using a modified core potential. There is one more matrix element that has not been covered so far and is as important for the work presented here: the matrix element for the $|5P_{3/2}\rangle \rightarrow |nS, D\rangle$ transition. This dipole matrix element controls the Rabi frequency $\Omega = -\frac{\vec{\mu}\cdot\vec{E}}{\hbar}$ of the Rydberg transition, determining, or even limiting, experimental sequence times and even controlling our Rydberg polaritons through the dark-state rotation angle (Section 3.3). As such, it is necessary to have a way to predict the coupling strength of the P-state to any Rydberg state. This can be done by using a core potential and energy of $5P_{3/4}$ state that allows for the construction of the $5P$ wavefunction and the calculation of transition radial matrix elements. These elements can be written as [48]:

$$\langle 5P_{3/2}|er|nlj\rangle = C_l(n^*)^{-3/2}, \tag{2.3.4}$$

where C_l is a coefficient dependent on l, with the values $C_S = 4.502\ ea_0$ and $C_D = 8.457\ ea_0$ for the Rydberg S and D states respectively.

2.4 Rydberg atoms in electric fields

A DC electric field E along the z-axis (as defined by the field) will cause the Rydberg states to mix, resulting in energy level shifts relative to the energy levels of a bare atom. This effect is called the Stark shift. This new $E\hat{z}$ term is effectively an electric dipole π transition and creates new eigenstates from the original Rydberg levels. To compute this effect, we have to extend the bare energy hamiltonian [45]:

$$H_{Stark} = H_{atom} + E\hat{z}$$

and compute its eigenvalues. The added electric field term produces off-diagonal couplings between all the states under the selection rule $\delta m_j = 0$. When the eigenvalues of H_{Stark} are plotted for all values of E for a set of Rydberg states with a given $|m_j|$, the resulting energy level diagram is called a Stark map.

Figure 2.2 shows a Stark map centered around the $100S$ state for $|m_j|$=1/2. The closest set of states to $100S$ is the hydrogenic manifold of the $n = 97$ level, showing the effect of quantum defects on the energy levels of the Rydberg atoms. These high angular momentum states are degenerate at zero field, leading to a first-order linear Stark shift. The lower l states exhibit stronger mixing and avoided crossings can be seen.

2.4.1 Scalar polarizability

At low fields (dependent on the Rydberg level) the Stark effect does not shift the energy of the atoms appreciably, acting as a second-order perturbation. This quadratic energy shift can be expressed as [45]:

$$\delta W = -\frac{1}{2}\alpha_0 E^2, \tag{2.4.1}$$

where α_0 is the static polarizability. This quantity can be related to the Rydberg dipole matrix elements through second-order perturbation theory:

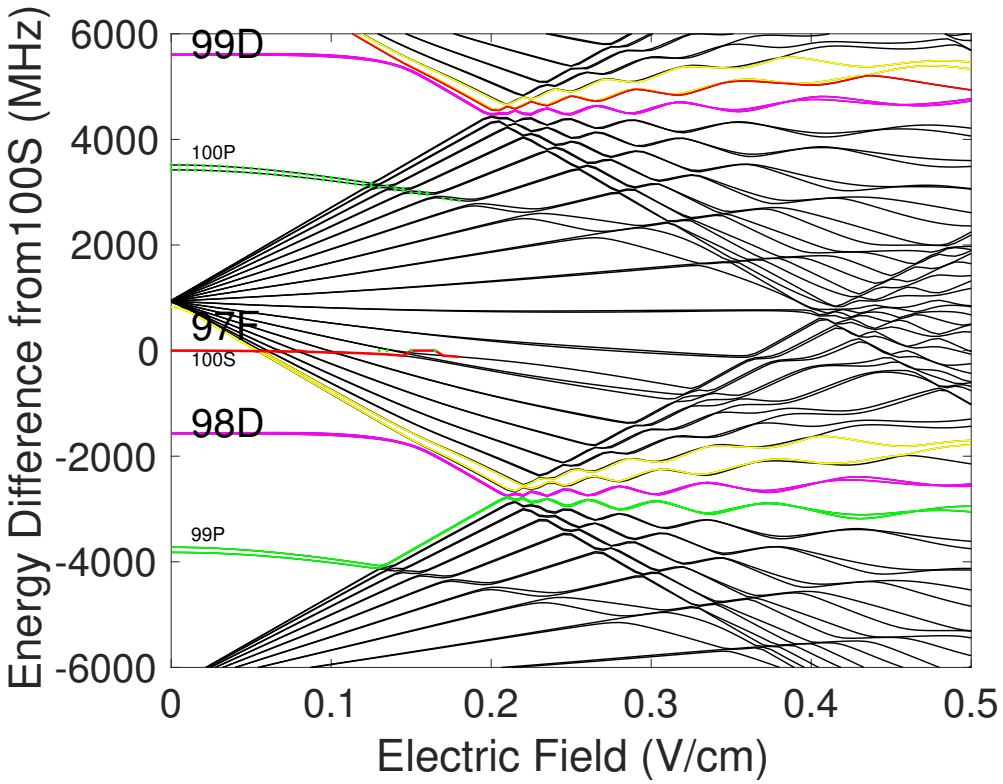

Figure 2.2: **Stark map of the 100S Rydberg state**. The Stark map is computed by diagonalizing H_{Stark} and plotting its eigenvalues for different values of the electric field. The $100S$ Rydberg state (red) can be seen mixing due to the Stark effect, until it has so heavily hybrizided with P states that it loses most of its character. The closest state to $100S$ is the $l > 4$ manifold for $n = 97$; this is a direct result of the quantum defects. The $98D$ state has a very small positive energy shift, until it starts mixing more strongly with F states, at which point its energy shift becomes negative.

$$\alpha_0 = \sum_{nlj \neq n'l'j'} \frac{|\langle n'l'j'm_j|\mu_0|nljm_j\rangle|^2}{W_{n'l'j'} - W_{nlj}}. \tag{2.4.2}$$

From this expression, the rapid scaling of polarizability with principal quantum number becomes evident: $\alpha_0 \propto \frac{\mu^2}{W} = (n^*)^4/(n^*)^{-3} = (n^*)^7$. This makes Rydberg atoms extremely sensitive to electric fields, a physical result of their large orbital radius as discussed at the start of the chapter.

Comparison of the theoretically computed polarizabilites with experimental data obtained by fitting the low-field energy shift of Rydberg atoms yield very good agreement [49]. Furthermore, an empirical scaling of the form $\alpha_0 = \beta_1 n^{*6} + \beta_2 n^{*7}$ has been discovered [49]. Rydberg S states have a consistenly positive polarizability, resulting in red Stark shifts. On the other hand, the behavior of D states is more complicated: their polarizability starts off positive at low fields until eventually an avoided crossing with the hydrogenic manifold of F states is encountered (shown in Figure 2.2) and the energy shifts become negative.

2.5 Rydberg interactions

Rydberg atoms have strong, long-range dipole-dipole interactions making them a suitable platform for manybody physics and quantum information processing. These interactions are highly-tunable: their strength, sign and angular dependence can all be precisely controlled.

2.5.1 Dipole-Dipole Interactions

Let us consider a pair of atoms, both in Rydberg state $|r\rangle$, separated by a distance $\vec{R}$. The dipole-dipole interaction (in atomic units) of this system can be written as [50]:

$$V(\vec{R}) = \frac{\vec{\mu}_1 \cdot \vec{\mu}_2}{R^3} - 3\frac{\left(\vec{\mu}_1 \cdot \vec{R}\right)\left(\vec{\mu}_2 \cdot \vec{R}\right)}{R^5},$$

where $\vec{\mu}_i$ is the dipole moment of the atoms associated with each available state they can couple to. In the simple case where both dipoles are aligned along the quantization axis (z-axis for notational convenience), the above expression for the dipole-dipole coupling becomes:

$$V(R) = \frac{\mu_{1-}\mu_{2+} + \mu_{1+}\mu_{2-} - 2\mu_{1z}\mu_{2z}}{R^3}, \tag{2.5.1}$$

μ_{iq} is the dipole moment operator of atom i for the q dipole transition. For on-axis dipole alignment, the total angular momentum $M = m_{j1} + m_{j2}$ of the pair state is conserved.

The dipole-dipole interactions manifest by coupling the initial two Rydberg states to all other available states. As such, it is more convenient to move the system from an atomic to a pair state basis. For two Rydberg atoms in state $|rr\rangle$, the dipole-dipole interaction $V(R)$ couples them to pair state $|r'r''\rangle$. The energy separation of the pair states is:

$$\delta W = W_{|r'\rangle} + W_{|r''\rangle} - 2W_{|r\rangle}.$$

The energy shift resulting from this interaction (shown in Figure 2.3) can be calculated by diagonalizing the interaction Hamiltonian [51, 52]:

$$H_{int} = \begin{pmatrix} 0 & V(R) \\ V(R) & \delta W \end{pmatrix}. \tag{2.5.2}$$

The spatial dependence of the resulting eigenvalues can be shown in two distinct regimes:

1. Short range ($V(R) \gg \delta W$)

$$\Delta W = \pm V(R) = \pm \frac{C_3}{R^3}. \tag{2.5.3}$$

   This is the resonant dipole-dipole regime, indicated by the $\frac{1}{R^3}$ spatial dependence that static dipoles exhibit. The strength of the interaction scales as $C_3 \propto \mu^2 \propto n^{*4}$.

2. Long range ($V(R) \ll \delta W$)

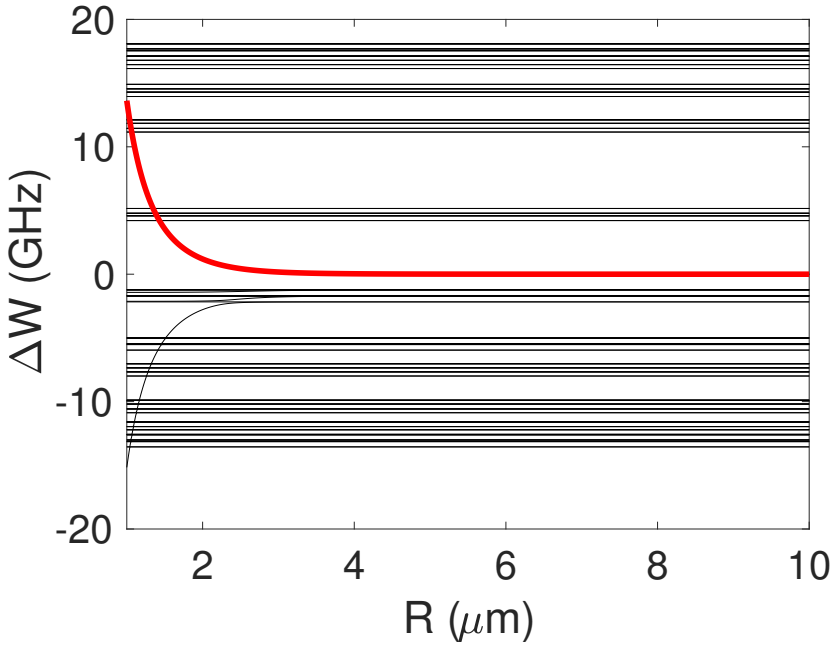

Figure 2.3: **60S60S interaction potential**. 60S60S pair state (red curve) energy as a function of distance, calculated using all pair states with $\delta W < 25$ GHz. The biggest contribution is from 60P59P pair state, which is repelled by the coupling. The shift from resonant to off-resonant dipole dipole interactions happens at about 2 μm for this pair state.

$$\Delta W = -\frac{V(R)^2}{\delta W} = -\frac{C_6}{R^6}. \tag{2.5.4}$$

This is the van der Waals, or off-resonant dipole-dipole, regime. The sign of the interaction is controlled by the sign of δW and the strength of the interaction scales as $C_6 \propto \frac{\mu^2}{\delta W} \propto \frac{n^{*4}}{n^{*-3}} \propto n^{*11}$.

2.5.2 Angular dependence of interactions

Typically, the dipoles producing the Rydberg-Rydberg interactions will not be aligned with the quantization axis and so the simple expression of Equation 2.5.1 for the interactions cannot be used. Instead, the relevant expression is the more generalized version of the

dipole-dipole coupling [53], which is a function of both R and θ:

$$\begin{aligned} V(R,\theta) &= \frac{\mu_{1-}\mu_{2+} + \mu_{1+}\mu_{2-} + (1-3\cos^2\theta)\mu_{1z}\mu_{2z}}{R^3} \\ &+ \frac{3\sin^2\theta(\mu_{1+}\mu_{2+} + \mu_{1+}\mu_{2-} + \mu_{1-}\mu_{2+} + \mu_{1-}\mu_{2-})}{2R^3} \\ &+ \frac{3\sin 2\theta(\mu_{1z}\mu_{2+} + \mu_{1z}\mu_{2-} + \mu_{1+}\mu_{2z} + \mu_{1-}\mu_{2z})}{2\sqrt{2}R^3}. \end{aligned} \tag{2.5.5}$$

For dipoles not aligned along the quantization axis, the interactions no longer conserve the total angular momentum of the pair state, mixing states of different M.

Due to their spherical orbital shape, S-states have a very small angular variation and so this effect can be neglected during our experiments.

2.6 Summary

In this chapter I presented the simple scaling laws of Rydberg atoms for properties such as transition frequencies and scalar polarizability in terms of the principal quantum number. A core model potential was introduced that allows for the numerical calculation of Rydberg state wavefunctions and consequently their electric dipole matrix elements. These dipole moments are the most interesting property of Rydberg atoms: they lead to both large polarizabilities and produce very strong interactions. The dipole-dipole interactions of Rydberg atoms can be divided into two spatial regimes: (i) short range, where the dipole-dipole interaction dominates the energy spacing of the pair states and has a $1/R^3$ dependence and (ii) long range, the regime where van der Waals interactions dominate, scaling as $-\frac{C_6}{R^6}$.

CHAPTER 3
THEORY OF INTERACTING CAVITY RYDBERG POLARITONS

3.1 Introduction

Current efforts to produce and explore the properties of synthetic quantum materials take numerous forms, from ultracold atoms [54] to superconducting circuits [55–57] and electronic heterostructures [58, 59] and superlattices [60]. Cold atom techniques allow for precise control through lattice tuning [20] and Feshbach resonances [21, 61]. Superconducting quantum circuits present an opportunity to create materials from strongly interacting microwave photons, as they exhibit excellent coherence [62], strong interactions [63], and have recently been shown to be compatible with low disorder lattices [64], low loss lattice gauge fields [65], and interaction and dissipation driven phase transitions [66].

In parallel, there is now growing interest in creating materials from optical photons. Non-interacting photons have been Bose-condensed in a resonator using a dye as a thermalization medium [13]; photons have been made to interact weakly and subsequently Bose condense by coupling them to interacting excitons [59]. To explore strongly interacting photonic materials, it has previously been proposed to marry Rydberg electromagnetically induced transparency (EIT) tools developed to induce free-space photons to interact [28, 33, 67, 68] with multimode optical resonators [69] to control the properties of individual photons [11], thereby introducing a real mass for 2D photons, and effective magnetic fields [12], in conjunction with Rydberg mediated interactions. It was recently experimentally demonstrated that individual cavity photons do indeed hybridize with Rydberg excitations to form "cavity Rydberg polaritons," quasiparticles [70–72] that collide with one another with high probability [34].

Formal modeling of these complex systems is incomplete. The properties of interacting

free-space Rydberg polaritons have been explored in the dispersive regime [73], as well as the resonant regime for Van der Waals [30, 74] and dipolar interactions [75]. Effective models of strongly interacting two-level cavity polaritons have been developed [76], along with blockade "bubble" approximations that qualitatively reflect the physics of three-level polaritons [77], but to date no effective theories of three-level cavity Rydberg polaritons exist which quantitatively reproduce the observed strong interactions, as a consequence of the intricate renormalization of the two-polariton wavefunction once the polaritons overlap in space.

In this chapter, I will formalize and extend the theory developed in [34, 69]. The starting point is formally defining the various Hamiltonians that are relevant to Rydberg polaritons in a resonator and deriving the polaritonic creation operators and interaction form. The development of a single-mode renormalized effective theory is motivated and realized and has excellent agreement with full numerics employed in previous works. A discussion on momentum-space interactions follows; an extension of how familiar position dependent Rydberg-Rydberg interactions change in the fourier plane. Finally, the impact of atomic motion on polariton coherence is explored.

More specifically, cavity Rydberg polaritons at large separations are described by the Hamiltonian $H_{pol} \sim \cos^2 \frac{\theta_d}{2}\ H_{phot} + \sin^4 \frac{\theta_d}{2}\ H_{int}$, where H_{phot} is the Hamiltonian describing the bare cavity-photon dynamics, determined through the resonator geometry; and H_{int} is the Hamiltonian describing the Rydberg-Rydberg interactions. The polaritons thus inherit properties from both photonic and atomic constituents, with the proportion of each contribution determined by the dark state rotation angle θ_d [78], providing an interaction tuning knob akin to an atomic Feshbach resonance [61]. The limitations of this model are examined, providing quantitative refinements to various aspects of it.

3.1.1 Chapter Overview

In section 3.2 we begin with the Floquet Hamiltonian for non-interacting resonator photons [11] and formally couple these photons to an ensemble of Rydberg-dressed three-level atoms residing in a waist of the resonator [69]. In section 3.3 we explore the physics of an individual photon in the resonator, discovering one long lived dark polariton (with renormalized mass relative to the bare photon) and two short-lived bright polaritons. In section 3.4 we generalize to the case of two dark polaritons in the resonator, derive the form of the low-energy polariton-polariton interaction potential, investigate scattering into bright-polariton manifolds as well as the regime of validity of the two polariton picture in the face of interactions and loss, focusing in section 3.5 on collisional loss of polaritons by dark→bright scattering. Once the interaction energy becomes larger than the dark/bright splitting the simple polaritonic picture breaks down, so in section 3.6 we explore the maximally challenging case of two dark polaritons in single mode optical resonator, developing a properly renormalized effective theory of interacting polaritons (with first principles calculable parameters) that we benchmark against a complete, but numerically intensive, microscopic theory. We find excellent agreement in experimentally relevant parameter regimes, pointing the way to a fully renormalized effective field theory of multimode cavity Rydberg polaritons. In section 3.7 we demonstrate that a properly situated Rydberg-dressed atomic ensemble produces interactions between polaritons that are local in momentum-space. In section 3.8 we relax the assumption of stationary atoms and investigate the effect of atomic motion on polariton coherence in both single- and multi- mode regimes. Finally, in section 3.9 we conclude with a discussion of applications of cavity Rydberg polaritons to quantum information processing and strongly-correlated matter.

Table of Results		
Polariton Projected Hamiltonian	Eqn. 3.4.2	Page 35
Renormalized Theory	3.6.1, 3.6.2, 3.6.3	43
Role of Atomic Motion	3.8.1	47
Doppler Decoherence	3.8.3	50
Crossmode Thermalization	3.8.4	50

3.2 Coupling the Photons to an Atomic Ensemble

Here we explore how the coupling to an ensemble of three-level atoms impacts the physics of non-interacting 2D photons in multi-mode resonators. We find the emergence of long lived "dark" polaritons, with dynamics similar to those of a resonator photon but renormalized mass and harmonic trapping. Off-resonant, nonadiabatic couplings to "bright" polaritons limit the lifetime of the dark polaritons. We operate in the limit that the light-matter coupling energy scale is much larger than the energy scale of the photonic dynamics within the resonator, making the polaritonic quasiparticles a nearly "good" basis for describing the physics, with corrections that we derive.

The second quantized Hamiltonian for photons within a single longitudinal manifold of a resonator is given by [11]:

$$H_{phot} = \int \mathrm{d}x \; a^\dagger(x) h_{phot} a(x),$$

where $a^\dagger(x)$ creates a photon at transverse location x and h_{phot} is the single particle Hamiltonian for a photon within the resonator, typically given by $h_{phot}(x) = \frac{\mathbf{\Pi}^2}{2m_{phot}} + \frac{1}{2} m_{phot} \omega_{trap}^2 |x|^2 - i\frac{\kappa}{2}$. Here x runs over the plane transverse to the resonator axis, κ parametrizes the (mode independent) resonator loss, and $\mathbf{\Pi} \equiv i\hbar\nabla - e\mathbf{A}$ is the mechanical momentum; the parame-

ters of this photonic "Floquet" Hamiltonian are determined by resonator geometry: mirror locations and curvatures, plus the twist of the resonator out of a single plane [11, 12].

We now insert a Rydberg-dressed atomic ensemble into the resonator as a tool to mediate interactions between the photons. To this end, the lower (S→P) transition of this ensemble is coupled to the quantized resonator field, while the upper (P→Rydberg) transition is coupled to a strong coherent field (see Fig. 3.1a). Before exploring the resulting photon-photon interactions, we must first understand how the Rydberg-dressed atoms impact the linear dynamics of individual photons. The light-matter coupling induced by the introduction of the atomic ensemble takes the form (in the frame rotating with the resonator- and Rydberg-dressing fields):

$$\begin{aligned} H_{at} = \int \mathrm{d}x^2\mathrm{d}z \; \{&\phi_r^\dagger(x,z)\phi_r(x,z)\left(\delta_2 - i\frac{\gamma_r}{2}\right) \\ &+\phi_e^\dagger(x,z)\phi_e(x,z)\left(\delta_e - i\frac{\gamma_e}{2}\right) \\ &+\phi_r^\dagger(x,z)\phi_e(x,z)\frac{\Omega}{2}(x,z) + \text{h.c.} \\ &\phi_e^\dagger(x,z)a(x)\frac{G(x,z)}{2} + \text{h.c.}\}. \end{aligned} \tag{3.2.1}$$

Here $\phi_r^\dagger(x,z)$ and $\phi_e^\dagger(x,z)$ are the bosonic creation operators for atomic excitations at 3D location (x,z) in the Rydberg and excited (P) states respectively, from the "vacuum" of ground state atoms. γ_r and γ_e are the FWHM of the Rydberg and excited states respectively. δ_e is the detuning of an untrapped, zero-transverse-momentum resonator photon from the atomic line and δ_2 is the two-photon detuning from EIT resonance. $\Omega(x,z)$ is the laser induced Rabi coupling between excited (P) and Rydberg states, while $G(x,z)$ is the vacuum-Rabi coupling strength between a resonator photon localized at transverse location x and a collective atomic excitation localized at longitudinal location z, and therefore must reflect the atom density. It does not reflect the transverse spatial structure of any particular resonator

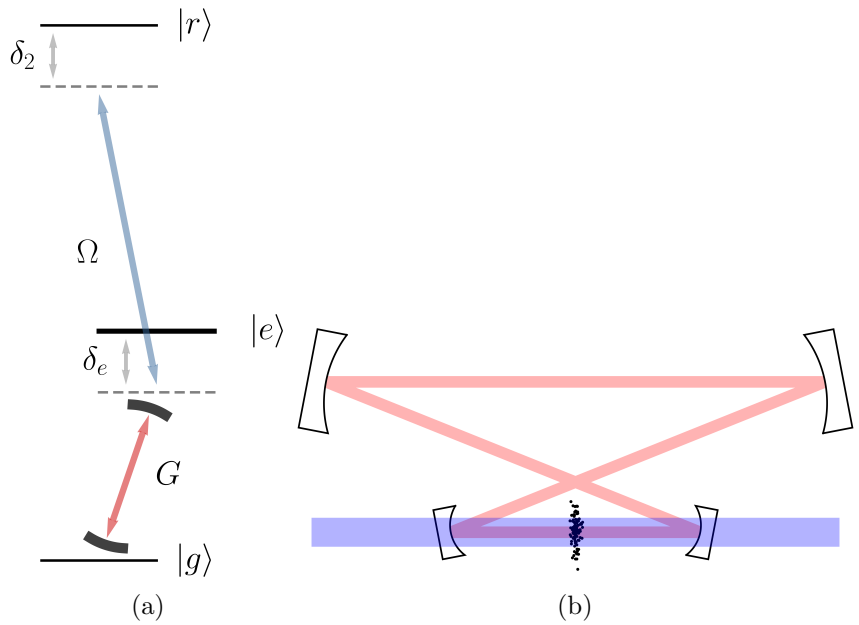

Figure 3.1: **Resonator Rydberg polariton three-level system and setup schematic.** **(a)** The atomic ground state $|g\rangle$ is coupled to the excited state $|e\rangle$ through the cavity mode, with detuning δ_e and collective coupling strength G. The control beam then excites the atoms to the Rydberg state $|r\rangle$, with Rabi frequency Ω and two-photon detuning δ_2.The horizontal displacement of the energy levels indicates a change in circular polarization. **(b)** The four mirror resonator supports running wave modes and two waists, allowing for both real and momentum space interactions. The primary (real space) atomic ensemble sits in the lower waist, where it mediates photon-photon interactions by admixing in a Rydberg state using the blue control field.

mode, as $a^\dagger(x)$ creates a transversely localized photon. Indeed it may be written as $G(x,z) \approx d_{ge}\sqrt{\frac{L}{L_{res}}\frac{\rho(x)\hbar\omega_{ge}}{\epsilon_0}}$, where L is the length of the atomic ensemble along the resonator axis, L_{res} is the length of the resonator itself, d_{ge} is the dipole moment of the atomic transition coupled to the optical resonator, ω_{ge} is the angular frequency of this transition, and $\rho(x)$ is the number density of atoms at location x.

Here and throughout, we incorporate losses through non-Hermitian Hamiltonians rather than through Lindbladian master equations. This allows us to identify the imaginary part of one- and two- particle eigenstates with quasi-particle decay rates ([79] III.B.2).

In this section, we have shown the photonic and atomic Hamiltonians (H_{phot} and H_{at} respectively) and defined the photonic and bosonic operators necessary to couple photons

to an atomic ensemble. This is a general result that is valid for both single- and multi-mode resonators, evident in the fact that all the operators and Rabi couplings are position dependent, to reflect the different mode shapes and atomic distribution over them.

3.2.1 Resonator Degeneracies and Photon Localization

We generally treat photons as objects that can occupy a completely arbitrary spatial mode in the 2D plane transverse to the resonator axis. In practice, resonator geometry can impose additional symmetries on the allowed photon wave-functions, and limit the permissible degree of photon localization. In what follows we explore the wave-function constraints imposed by various resonator configurations.

It is convenient to begin by considering a general non-degenerate spherical mirror Fabry-perot resonator [10], whose modes are enumerated with three indices l, m, n; the first index l, is the longitudinal mode number, while m, n index the transverse mode:

The most extreme case is degeneracy of all the transverse modes of a resonator, $\omega_{lmn} = \omega_l$, achieved in planar and concentric cavities [10] (note that we have re-indexed the longitudinal modes of the concentric resonator). Planar resonators are constructed with flat mirrors (radius of curvature $\to \infty$) very close together, while concentric cavities consist of two mirrors separated by the sum of their radii of curvature. In both configurations the space of allowed photon wave-functions is not constrained by any symmetries, and arbitrarily small spots can be created at any point in 2D space (see Figure 3.2b).

The next most extreme case is families of degenerate modes that still require two indices to enumerate, but with restrictions on the indices. An example of this is the confocal resonator: two mirrors with radii of curvature R placed a distance R apart. Such a resonator exhibits $\omega_{lmn} = \omega_{l,mod(m+n,2)}$. The constraint that $m + n$ is either even or odd imposes a reflection symmetry across the origin: the photon may be arbitrarily well localized in space at any location, but must *simultaneously* exist at this mirror-image location (see Figure 3.2c).

The next case is degenerate families that may be indexed with only a single parameter, which may themselves be further broken down into two sub-categories: (1) families in which the index takes on only a finite number of values; and (2) families in which the index takes on a countably infinite number of values. A spherical mirror Fabry-Perot falls into the first category; $\omega_{lmn} = \omega_{l,m+n}$; another example is an astigmatic resonator whose length is tuned to enforce degeneracy such as $\omega_{lmn} = \omega_{l,m+2n}$ [72] (see Figure 3.2d). The latter category could be achieved in an astigmatic resonator tuned to confocality on only one axis: $\omega_{lmn} = \omega_{l,m,mod(n,2)}$, or in a non-planar resonator by imposing twist which is a rational fraction of 2π, as in [12]:$\omega_{lmn} = \omega_{l,m,mod(n,3)}$ (see Figure 3.2e). The reduced degeneracy strongly constrains the wavefunctions which may be represented by the family, to the point that the physical interpretation of these families is often quite unclear. Indeed, the twisted resonator explored in [12] exhibits three-fold rotational symmetry, and quantum geometry, meaning that has a minimum spot size; this system may be understood as a Landau level on the surface of a cone, quite an exotic manifold indeed.

3.3 Polariton Basis

The atomic density distribution exists in three dimensions, while the manifold of nearly-degenerate resonator modes to which the atoms couple is two-dimensional (here we assume $G \ll \frac{c}{L_{res}}$, ensuring that the atoms couple to only a single longitudinal manifold of the resonator). In order to develop a formalism of two-dimensional polaritons, we define longitudinally delocalized, transversely localized collective atomic excitation operators (for k_{laser} and k_{cav} the wave-vector magnitudes of the coupling-laser and resonator fields, respectively), normalized to ensure a mode-independent bosonic commutation relation. To this end we choose the minimal case of an atomic ensemble of uniform density, and a uniform coupling-field that propagates counter to the resonator field:

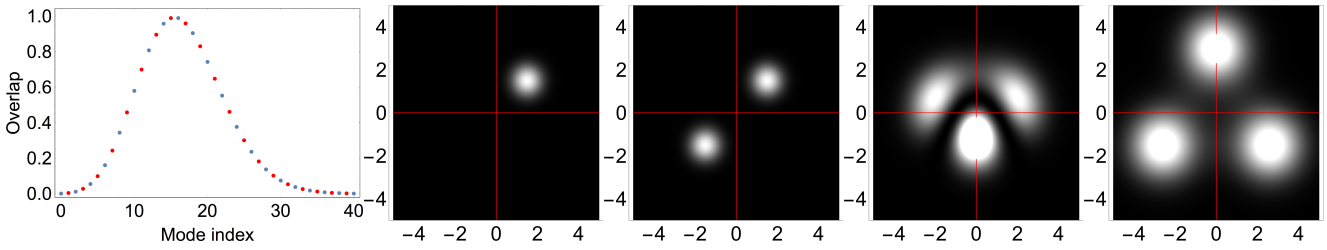

Figure 3.2: **Resonator degeneracies and their effects on photon localization and spot size.** **(a)**Decomposition of an off-center Gaussian into 1D HG modes. A Gaussian at any arbitrary location can be written as the sum of 1D HG modes, by taking the spatial overlap of the Gaussian with each mode. The overlaps are shown in the plot, with even modes represented as blue dots and odd modes as red dots. **(b)**Localization of a photon in a planar or concentric cavity. When all resonator modes are degenerate, we can create a photon at any location inside the resonator and of any spot size. This can be understood as a generalized version of the decomposition in (a), but in general it is done in a two dimensional parameter space. The red lines in the plot signify $x = 0, y = 0$, showing than an off-center spot has been created. **(c)**In a confocal resonator, we have degeneracy within the even and odd mode manifolds only. As such, a decomposition of any spot would include either the even (blue) or odd modes (red dots) only. Any spot size at any location can still be created but now we pick up reflections through the origin, resulting in a mirrored spot. **(d)**Superposition of TEM_{20} and TEM_{01}. This is an example of a finite one parameter family. The resonator mirrors and mirror positions are picked in such a way as to make these two modes energetically degenerate. The result is interference between the two modes, resulting in a new mode shape [72]. **(e)** Threefold symmetry in a resonator. In a countably infinite single parameter family of degenerate modes where every third LG mode is degenerate (LG_l,LG_{l+3},LG_{l+6},...), a localized spot can be created at any point but must satisfy a threefold rotational symmetry, resulting in three copies, each of which cannot be smaller than the LG_0 waist size of the resonator [12].

$$\phi_e^\dagger(x) \equiv \sqrt{\frac{1}{L}} \int_{-\frac{L}{2}}^{\frac{L}{2}} \mathrm{d}z \; \phi_e^\dagger(x,z) e^{-ik_{cav}z}$$

$$\phi_r^\dagger(x) \equiv \sqrt{\frac{1}{L}} \int_{-\frac{L}{2}}^{\frac{L}{2}} \mathrm{d}z \; \phi_r^\dagger(x,z) e^{i(k_{laser}-k_{cav})z}.$$

We can now rewrite the atomic Hamiltonian in the single-longitudinal-mode-projected manifold as:

$$H_{at} = \int \mathrm{d}x^2 \; [W^\dagger(x)][h_{at}][W(x)]$$
$$\text{where } [W^\dagger] \equiv (a^\dagger(x) \; \phi_e^\dagger(x) \; \phi_r^\dagger(x))$$
$$\text{and } [h_{at}] = \begin{pmatrix} 0 & \frac{G}{2} & 0 \\ \frac{G}{2} & \delta_e - i\frac{\gamma_e}{2} & \frac{\Omega}{2} \\ 0 & \frac{\Omega}{2} & \delta_2 - i\frac{\gamma_r}{2} \end{pmatrix}.$$

Here $G \approx d_{ge}\sqrt{\frac{L}{L_{res}}\frac{\rho\hbar\omega_{ge}}{\epsilon_0}}$, where L is the length of the atomic ensemble along the resonator axis. Note that $[h_{at}]$ has no position dependence, because we are assuming no atomic motion (covered in section 3.8), no inhomogeneous electric fields, and that the coupling field is large enough transversely that variations in the control-field Rabi frequency Ω are negligible. In the basis where $[h_{at}]$ is diagonal, the resulting creation operators are the generators of three varieties of polaritons: one dark (with little to no excited state participation, depending on κ and γ_r), sandwiched between two bright (with large excited state participation). In the simplest case of no detunings or cavity loss, we can express the polaritonic creation operators in the atomic basis as follows:

$$\begin{aligned} d^\dagger &= \frac{\Omega}{\sqrt{G^2+\Omega^2}}a^\dagger(x) - \frac{G}{\sqrt{G^2+\Omega^2}}\phi_r^\dagger(x), \\ b_\pm^\dagger &= \frac{1}{\sqrt{2}}\left(\frac{G}{\sqrt{G^2+\Omega^2}}a^\dagger(x) \pm \phi_e^\dagger(x) + \frac{\Omega}{\sqrt{G^2+\Omega^2}}\phi_r^\dagger(x)\right). \end{aligned}$$

We are primarily concerned with the long-lived and strongly interacting dark polaritons, but will include off-resonant couplings to the bright polaritons to accurately model dark-polariton lifetime.

More formally, we diagonalize $[h_{at}] = \sum \mu_m \tilde{\mu}_m \epsilon_m$, where m is an element of [d,b$_-$,b$_+$], meaning [dark, lower bright, upper bright], ϵ_m is the energy of (ket) μ_m and (bra) $\tilde{\mu}_m$ and

the $\mu_m, \tilde{\mu}_l$ satisfy the generalized orthogonality condition (due to the non-hermicity of h_{at}): $\tilde{\mu}_l \cdot \mu_m = \delta_{lm}$. Note that because of the non-hermicity of h_{at}, $\tilde{\mu}_m \neq \mu_m^\dagger$.

The resulting polariton creation and annihilation operators are thus:

$$\begin{aligned} \chi_j^\dagger(x) &= [W^\dagger] \cdot \mu_j, \\ \chi_j(x) &= \tilde{\mu_j} \cdot [W]. \end{aligned}$$

For notational convenience *only* have we named the polariton creation/annihilation operators "$\chi_j^\dagger(x)$" and "$\chi_j(x)$"; these operators are *not* precisely Hermitian conjugates of one another, but are instead defined to preserve the bosonic commutation relations: $[\chi_j(x), \chi_k^\dagger(x')] = \delta_{jk}\delta(x - x')$. We may now write H_{at} as:

$$H_{at} = \sum_m \int \mathrm{d}x \; \chi_m^\dagger(x)\chi_m(x)\epsilon_m.$$

The last step in writing H_{tot} in the polariton basis is to decompose $a^\dagger(x), a(x)$ into polariton field operators:

$$\begin{aligned} a^\dagger(x) &= \sum_j c_j \chi_j^\dagger(x), \\ a(x) &= \sum_j \tilde{c}_j \chi_j(x), \end{aligned}$$

where the $c_j, \tilde{c}_j$ are elements of the inverse $\mu, \tilde{\mu}$ matrices: $c_j \equiv \mu_{cav,j}^{-1}, \tilde{c}_j \equiv \tilde{\mu}_{cav,j}^{-1}$ and the index "cav" denotes the photonic slot of $\mu^{-1}, \tilde{\mu}^{-1}$. H_{tot} can now be written as:

$$H_{tot} = \sum_{ij} \int \mathrm{d}x \; c_i \tilde{c}_j \chi_i^\dagger(x) h_{tot}^{ij}(x) \chi_j(x),$$

where $h_{tot}^{ij}(x) \equiv \delta_{ij}\epsilon_i + h_{phot}(x)$.

We will operate in the limit that the difference of the eigenvalues of h_{at} (the "dark"-"bright" splitting) is much larger than the spectrum of h_{phot}, making the $[d, b_+, b_-]$ basis that diagonalizes the atomic Hamiltonian a near-diagonal basis for the multimode system. This is equivalent to the statement that a particle oscillating in the trap is more accurately described as a polariton rather than a photon if the light-matter coupling is much greater than the transverse optical mode spacing. To first order in h_{phot}/ϵ, the Hamiltonian projected into the dark polariton manifold is:

$$H_{tot}^{pol} = \int \mathrm{d}x \; c_d \tilde{c}_d \chi_d^\dagger(x)(\epsilon_d + h_{phot}(x))\chi_d(x).$$

For $\gamma_r = \delta_2 = 0$: $\epsilon_d = 0$ and $c_d\tilde{c}_d = \frac{\Omega^2}{\Omega^2+G^2} = \cos^2\frac{\theta_d}{2}$, where θ_d is the dark state rotation angle [78]. We then have:

$$H_{tot}^{pol} = \cos^2\frac{\theta_d}{2} \int \mathrm{d}x \; \chi_d^\dagger(x) \left[\frac{\mathbf{\Pi}^2}{2m_{phot}} + \frac{1}{2} m_{phot} \omega_{trap}^2 |x|^2 - \frac{i\kappa}{2} \right] \chi_d(x). \tag{3.3.1}$$

Thus, we see that to lowest order in ratio of the photonic dynamics energy scale to the atomic coupling energy scale $\frac{\omega_{trap}^2}{\Omega^2+G^2}$, the atoms simply slow down all photonic dynamics and loss by a factor of $\cos^2\frac{\theta_d}{2}$. The dominant correction to this story is a second-order resonator (h_{phot}) -induced dark$\rightarrow$bright coupling, producing an effective Hamiltonian [79] (in the above limits):

$$\delta H_{tot} \approx \sum_{j\in[b_-,b_+]} \int \mathrm{d}x \frac{H_{phot}\chi_j^\dagger(x)\chi_j(x)H_{phot}}{\epsilon_j - \epsilon_d}$$

To compute this effect for a dark-polariton in an eigenstate with energy $E = \frac{\Omega^2}{G^2+\Omega^2}\delta \ll \sqrt{\Omega^2+G^2}$,where δ is the two-photon detuning from EIT resonance, we take the first eigenvalue of h_{at} by solving the equation $\det(h_{at} - \lambda\mathbb{1}) = 0$ and Taylor expanding to first order in λ and then to second order in δ and κ. The correction is largely imaginary (assuming for simplicity that $\delta_e = 0, g, \Omega \gg \gamma_e$):

$$\delta\Gamma_{pol} \equiv -i\langle\delta H_{tot}\rangle \approx 2\frac{\Omega^2\delta^2}{\Omega^2+G^2}\gamma_e = 2\frac{E^2}{\Omega^2}\gamma_e. \tag{3.3.2}$$

Thus we see that loss is suppressed by the control field.

Additional contributions to polariton loss arise from inhomogeneous broadening of the Rydberg manifold, e.g. atomic motion and electric field gradients (to which Rydberg atoms are susceptible due to their large DC polarizability [80]). Such processes generate a ladder of couplings from the collective Rydberg state, that shares the spatial configuration of the resonator mode, into collective states orthogonal to it (which therefore are bright). We explore how (random) atomic motion induces polariton decoherence in Sec 3.8; for inhomogeneous E-fields, the coupling rate to the bright manifold is $\gamma_b \approx \alpha E\delta E$, where α is the DC polarizability of the Rydberg state, E is the DC electric field at the atomic sample, and δE is the field-variation across it. The resultant broadening of the dark manifold is then (in the limit $\Omega \gg \gamma_e$) [72]:

$$\delta\Gamma_{pol} \sim \gamma_e\frac{\gamma_b^2\sin^2\frac{\theta_d}{2}}{\Omega^2}. \tag{3.3.3}$$

It is instructive to compare this result with the loss induced by detuning a resonator mode out of the EIT window (Eqn. 3.3.2). Both channels are quadratically suppressed, but the suppression factor is different, emphasizing the distinction between the underlying physical processes: detuning from the EIT window couples to bright polariton manifolds that live in the resonator and are thus suppressed by both the light-matter-coupling- and control- fields, while inhomogeneous broadening couples to non-resonator bright polariton manifolds that "see" only the control- field.

Having formalized the notion of a resonator polariton, it is instructive to note some differences between resonator and free-space polaritons. Cavities provide a true 2D system (for a single longitudinal mode and in the limit of small sample length L), where the single particle dispersion is controlled through the resonator geometry [81]. On the other hand, free space polaritons exhibit more rigid dispersion relations. They possess different longitudinal and transverse masses, and the transverse mass may even be complex [32].

To summarize, we have derived the polaritonic creation and annihilation operators and reformulated the polaritonic Hamiltonian in second quantized form for arbitrary multi-mode resonators. With the introduction of the dark state rotation angle, we have a way to quantify the character and behaviour of the quasi-particles. Finally, we have derived a second order correction to the dark polariton lifetime arising from dark to bright polariton coupling and inhomogeneous Stark shifts; both processes result in additional polariton decoherence and are quadratically suppressed.

3.4 Polariton-polariton Interactions

The interaction between Rydberg atoms will result in an interaction between polaritons, much as in the 1D free-space situation [28–31]. In the limit that the interaction length-scale is comparable to the mode-waist of the resonator, there can be a substantial renormalization of the collective atomic excitation which we investigate in Sec 3.6. For now, we assume

sufficiently weak interactions that photonic- and collective-atomic- components of the polariton wave-function share the same spatial structure; note that these interactions can still dominate over kinetic and potential energies, as well as particle decay rates, so this need not be a "weakly interacting" polaritonic gas in the traditional (mean-field) sense.

The bare 3D interaction between two Rydberg atoms takes the form $V(x-x') = \frac{c_r(\theta)C_6}{|x-x'|^6}$ [40], where $c_r(\theta)$ is the angular dependence of the interaction. S-Rydberg atoms have radially symmetric wavefunctions and so $c_r(\theta) \approx c_r \equiv 1$. In the second quantized picture, for a thin atomic cloud (thickness $L \ll d$, where d is the cavity analog of the blockade radius [68]; this restriction is needed to ensure the polariton separation is well defined in the 2D plane) the 2D-projected interaction takes the form (with $\tilde{V}(x) = V(x; z = 0)$):

$$H_{int} = \frac{1}{2}\iint \mathrm{d}x\ \mathrm{d}x' \phi_r^\dagger(x)\phi_r^\dagger(x')\tilde{V}(x-x')\phi_r(x')\phi_r(x).$$

$\phi_r^\dagger(x)$ may be written in the polariton basis in analogy to the way $a^\dagger(x)$ was written in the polariton basis in the preceding section:

$$H_{int} = \frac{1}{2}\sum_{ijkl\in[d,b_-,b_+]} d_i d_j \tilde{d}_k \tilde{d}_l \iint \mathrm{d}x\ \mathrm{d}x'\ \chi_i^\dagger(x)\chi_j^\dagger(x')\tilde{V}(x-x')\chi_k(x')\chi_l(x). \quad (3.4.1)$$

Here $d_i, \tilde{d}_j$ are matrix elements of the inverse $\mu, \tilde{\mu}$ matrices: $d_j \equiv \mu^{-1}_{ryd,j}, \tilde{d}_j \equiv \tilde{\mu}^{-1}_{ryd,j}$ and the index "ryd" denotes the Rydberg slot of $\mu^{-1}, \tilde{\mu}^{-1}$. In the absence of Rydberg loss and 2-photon detuning, $d_d = \sin\frac{\theta_d}{2}$.

If the interaction energy $\tilde{V}$ is small compared to the splitting between dark- and bright-polariton branches (Sec. 3.5 explores the couplings and loss that violate this condition), the diagonal elements of H_{int} dominate, yielding a lowest-order polariton-projected effective Hamiltonian:

$$\boxed{\begin{aligned}\hat{P}_d(H_{tot}+H_{int})\hat{P}_d = \cos^2\frac{\theta_d}{2}\Big(\int \mathrm{d}x\chi_d^\dagger[\frac{\mathbf{\Pi}^2}{2m_p}+\frac{1}{2}m_p\omega_t^2|x|^2-\frac{i\kappa}{2}]\chi_d\Big)\\ +\frac{1}{2}\sin^4\frac{\theta_d}{2}\left(\iint \mathrm{d}x\mathrm{d}x'\hat{n}_d(x)\hat{n}_d(x')\tilde{V}(x,x')\right),\end{aligned}} \tag{3.4.2}$$

where $\hat{P}_d$ is dark-polariton projection operator, and we have defined the dark polariton number density operator $\hat{n}_d(x) = \chi_d^\dagger(x)\chi_d(x)$.

By tuning the dark-state rotation angle θ_d (via atomic density and control-field intensity) it is possible to move from a weakly interacting gas of "nearly-photonic" polaritons (for $\theta_d \approx 0$) to a strongly interacting gas of "nearly-Rydberg" polaritons (for $\theta_d = \pi$) and explore the correlations which then develop [69]. In this latter limit it is likely that the interactions $\tilde{V}$ become comparable to the dark-bright splitting, so the interaction potential must be renormalized as explored in section 3.6.

Using the formalism developed in prior sections, we have now expressed the Rydberg polariton interactions in the general context of an arbitrary multi-mode resonator. The new polaritonic interaction term in the Hamiltonian assumes only that the sample is "thin" (in the sense that all atoms are longitudinally within the Rydberg blockade volume) and depends heavily on how Rydberg-like the polariton is, as expressed by the dark state rotation angle.

3.5 Interaction Driven Polariton Loss

The polariton-projected field theory of the preceding sections neglects loss from collisional coupling to bright manifolds. To make the impact of these processes apparent we work in the minimal model of a single-mode resonator (specifically the TEM_{00} mode), and simplify from long-range to δ interactions. The interaction between dark polaritons is then $\tilde{V}(x,x') = U_{eff}\delta(x-x')$, where U_{eff} is a phenomenological interaction strength. Such an interaction couples the two dark polariton state $|dd\rangle$ to a final two-polariton state $|f\rangle$ with Rabi frequency $\Omega_{dd\to f} = \langle f|\tilde{V}|dd\rangle$. We consider two final states: (1) one each upper and

lower bright polaritons ($|b_+b_-\rangle$), which is energetically degenerate with $|dd\rangle$, and (2) dark- and (upper/lower) bright- polariton ($|db\rangle$), which is off-resonant, but sufficiently spectrally broad that its enhanced matrix element makes it important.

In a frame rotating with the cavity and control fields ($\delta_e = \delta_2 = 0$), the dark polaritons have zero energy and the upper/lower bright polariton branches are energetically shifted by $\pm\frac{\sqrt{G^2+\Omega^2}}{2}$ (Fig. 3.3). The process $|dd\rangle \rightarrow |b_+b_-\rangle$ is thus energy conserving, with collisional Rabi coupling given by:

$$\begin{aligned}\Omega_{dd\rightarrow bb} &= \langle b_+b_-|\tilde{V}|dd\rangle = \sqrt{2}\sin^2\frac{\theta_d}{2}\cos^2\frac{\theta_d}{2}U_{eff} \\ &= \frac{1}{2\sqrt{2}}\sin^2\theta_d U_{eff}.\end{aligned}$$

Because this is a resonant scattering, it induces a loss $\Gamma_{dd\rightarrow bb} = \frac{\Omega_{bb}^2}{\Gamma_{bb}}$, where $\Gamma_{bb} = 2\frac{\gamma_e}{2}$ is the intrinsic loss of the bright polariton branches which are predominantly composed of the lossy P-state. Plugging in, the loss rate is:

$$\Gamma_{dd\rightarrow bb} = \frac{\sin^4\theta_d U_{eff}^2}{8\gamma_e}. \tag{3.5.1}$$

This loss depends heavily on the interaction strength between the Rydberg atoms and the dark state rotation angle. Making the particles more Rydberg-like creates stronger interactions and increases the loss rate; similarly, using a higher principle quantum number increases U_{eff}, further enhancing the loss.

We now investigate the second scattering process, $|dd\rangle \rightarrow |db\rangle$ (upper or lower bright polariton). Following the same procedure, the collisional Rabi frequency is:

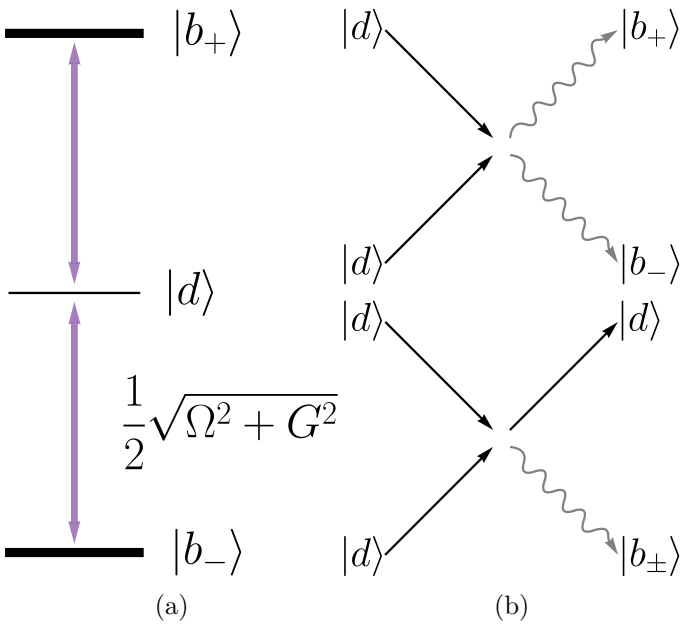

Figure 3.3: **Interaction driven loss. (a)** In the rotating frame, the dark polariton $|d\rangle$ has zero energy. The upper and lower bright polariton branches ($|b_+\rangle$ and $|b_-\rangle$ respectively) are separated in energy from the dark polariton by the coupling and control lasers, giving a detuning of $\pm\frac{\sqrt{G^2+\Omega^2}}{2}$. **(b)** Two dark polaritons that experience a contact interaction U_{eff} can become a pair of bright polaritons $|b_+b_-\rangle$ (upper diagram) or a dark and (upper- or lower- branch) bright polariton $|db_\pm\rangle$ (lower diagram). Dark polaritons are depicted by a straight black line while the wavy gray lines are bright polaritons. The form of the additional dark polariton loss introduced by these scattering events are determined by how "resonant" the processes are: the ∼energy conserving $|dd\rangle \to |b_+b_-\rangle$ process introduces a loss of $\Gamma_{dd\to bb} = \frac{\sin^4\theta_d U_{eff}^2}{8\gamma_e}$, while the $|dd\rangle \to |db_\pm\rangle$ coupling is "off-resonant" and so its additional loss $\Gamma_{dd\to db} = \sin^6\frac{\theta_d}{2}\sin^2\theta_d\frac{\gamma_e}{G^2}U_{eff}^2$ is suppressed by the light-matter coupling field.

$$\Omega_{dd\to db} \;=\; \langle db|\tilde{V}|dd\rangle = \sqrt{2}\sin^3\frac{\theta_d}{2}\cos\frac{\theta_d}{2}U_{eff}.$$

Since this is an off-resonant process (final and initial state are detuned by $\Delta = \frac{\sqrt{G^2+\Omega^2}}{2}$), the resulting loss rate is $\Gamma_{dd\to db} = \frac{\Omega_{db}^2}{\Delta^2}\Gamma_{db}$, with $\Gamma_{db} = \frac{\gamma_e}{2}$ (we ignore resonator- and Rydberg-loss, as bright-state loss is dominated by p-state loss in alkali metal atom Rydberg cQED experiments [34]). Combining these effects/approximations yields:

$$\Gamma_{dd\to db} = \sin^6\frac{\theta_d}{2}\sin^2\theta_d\frac{U_{eff}^2}{G^2}\gamma_e. \tag{3.5.2}$$

Once again, stronger interactions and a more Rydberg-like character for the polaritons increases the loss from this process but due to the off-resonant nature of this process there is a quadratic suppression from the light-matter coupling which separates the bright- and dark-polaritons in energy.

We can compare the two loss processes:

$$\frac{\Gamma_{dd\to bb}}{\Gamma_{dd\to db}} = \frac{\sin^2\theta_d}{8\sin^6\frac{\theta_d}{2}}\frac{G^2}{\gamma_e^2}. \tag{3.5.3}$$

In the limit $G \gg \Omega, \gamma_e$ ($\frac{\theta_d}{2} \to \frac{\pi}{2} \Rightarrow \sin\frac{\theta_d}{2} \to 1, \sin\theta_d \to 0$), the $|dd\rangle \to |db\rangle$ loss channel will dominate, while in the opposite limit, interaction-driven loss is dominated by the $\sim$ energy conserving process.

In this section, we explored dark→bright conversion through polariton-polariton scattering. For simplicity, we analyzed this physics in a single mode resonator with δ-interacting polaritons (hard sphere approximation of long-range interactions) and showed that there are

in fact two loss channels, with rates exhibiting similar functional forms, each dominating in a region of parameter space.

3.6 Effective Theory for Interacting polaritons

The simple polariton-projected interacting theory introduced in section 3.4 is an accurate description *only* for polaritons whose interaction energy is less than the EIT linewidth [72] for all pairs of atoms comprising the polaritons. As two polaritons approach one another and their wavepackets begin to spatially overlap, some terms in the interaction energy diverge; full numerics (see SI of [34] for details of the approach) reveal that the two-polariton wavefunction is renormalized to suppress such overlap, at the cost of additional (finite) interaction energy, and loss. Physically, at small separations and strong interactions, the pair distribution of Rydberg excitations no longer follows the wavefunction of the cavity field. We now explore the extreme limit of this physics: a single-mode optical resonator that is moderately-to-strongly blockaded, to develop a low-dimensional effective model in the basis of near-symmetric collective states that produces optical correlations in agreement with full numerics.

The "brute force" numerical approach that we have previously employed accounts for the three-level structure of each atom in the atomic-ensemble, and the interactions between atoms. It accurately reproduces observed correlations [34] at the expense of a Hilbert space which grows as N^m, where N is the number of atoms in the atomic ensemble and m the number of polaritons in the system; and quickly becomes computationally intractable when motional dynamics of the polaritons are included by allowing for multiple resonator modes. The problem of an extremely large Hilbert space is exacerbated since many-body physics [69, 82] demands both multiple resonator modes and significantly more than two excitations, which makes numerically computing the behavior of the system completely untenable without a coarse-grained effective theory.

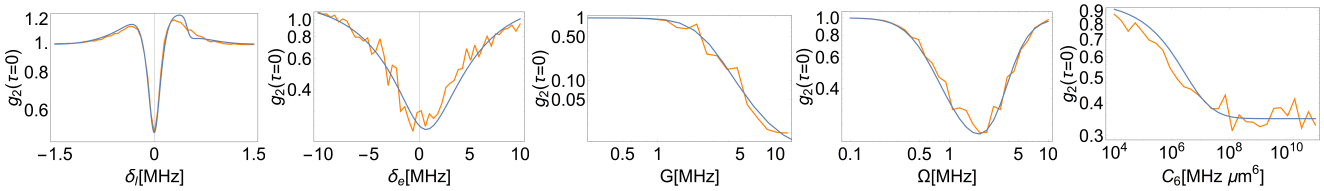

(a) (b) (c) (d) (e)

Figure 3.4: **Comparing the effective field theory to full numerics.** Effective theory renormalized interactions and couplings (blue line) and full numerical model (orange line) are compared by looking at the temporal intensity autocorrelation function $g_2(\tau = 0)$, which characterizes the strength of interactions in the system. Common parameters are (unless varied in the plot or mentioned otherwise): $G = 2\pi \times 6$ MHz, $\Omega = 2\pi \times 2.3$ MHz, $\delta_e = 0$ MHz, $C_6 = 2\pi \times 56$ THz μm^6 (corresponding approximately to the interaction strength of the 100S Rydberg state), $N_{atom} = 700$, $\gamma_e = 2\pi \times 6$ MHz, $\kappa = 2\pi \times 1.6$ MHz, $\gamma_r = 2\pi \times 0.15$ MHz, $\delta_c = 0$ MHz, cavity mode waist $w_c = 14$ μm, transverse atomic sample radius $r_t = 40$ μm, atomic sample length $l_a = 3$ μm, intracavity photon number $\ll 1$. **(a)** $g_2(\tau = 0)$ vs probe laser detuning. Scanning the probe laser frequency affects both the detuning to the P-state and the two-photon detuning to the Rydberg state. **(b)** $g_2(\tau = 0)$ vs P-state detuning δ_e. The detuning of the P-state δ_e is varied while keeping the two photon detuning δ_2 zero. **(c)** $g_2(\tau = 0)$ vs light-matter coupling field strength G, $g_2(\tau = 0)$ vs probe detuning δ_l (inset). The light-matter coupling strength per atom g is varied from $2\pi \times 0.07$ MHz to $2\pi \times 3$ MHz. For the inset, we scan the probe frequency. **(d)** $g_2(\tau = 0)$ vs control field strength Ω. There is good agreement between the full numerics and the renormalized effective theory except for a small region at about $\Omega = 2\pi \times 1 - 3$ MHz. **(e)** $g_2(\tau = 0)$ vs Rydberg-Rydberg interaction coefficient C_6. C_6 is varied from $2\pi \times 10^4$ MHz μm^6 to $2\pi \times 10^{11}$ MHz μm^6, which corresponds to Rydberg states in the range $n \sim$ 48-193S. The upper limit on the strength of the blockade is the cavity enhanced optical depth. Once C_6 is large enough to fully blockade the sample, the interaction strength, and therefore g_2, saturate. A control field of $\Omega = 2\pi \times 1$ MHz was employed for this plot. The first-principles renormalized theory accurately reproduces the blockade from weak- to strong- interactions.

To the extent that "polaritons" are well-defined collective excitations whose atomic spatial structure reflects the cavity mode functions, it should be possible to develop an effective theory whose Hilbert space size is independent of the atom number, making explorations of multimode/many-body physics tractable. In this section we demonstrate, for a single optical resonator mode, an approach to handle the suppression of short-range double-excitation of the Rydberg-manifold, arriving at a coarse-grained effective theory including both dark and bright polaritons whose parameters may be calculated from first principles.

Consider two excitations, either atomic or photonic, in an atomic ensemble coupled to a single-mode resonator. In the absence of interactions, we can explicitly write out the collective states that couple to the resonator field: $|CC\rangle$, $|CE\rangle$, $|CR\rangle$, $|EE\rangle$, $|ER\rangle$, $|RR\rangle$. These states represent two excitations as photons in the resonator, one photon and one p-state excited atom, one photon and one Rydberg atom, two excited p-state atoms, one p-state and one Rydberg atoms and two Rydberg atoms respectively. The Hamiltonian is closed in this basis, and takes the form [83]:

$$H = \begin{pmatrix} |CC\rangle & |CE\rangle & |CR\rangle & |EE\rangle & |ER\rangle & |RR\rangle \\ \hline -i\kappa & \frac{G}{\sqrt{2}} & 0 & 0 & 0 & 0 \\ \frac{G}{\sqrt{2}} & -i\frac{\kappa+\tilde{\gamma}_e}{2} & \frac{\Omega}{2} & \frac{G}{\sqrt{2}} & 0 & 0 \\ 0 & \frac{\Omega}{2} & -i\frac{\kappa+\gamma_r}{2} & 0 & \frac{G}{2} & 0 \\ 0 & \frac{G}{\sqrt{2}} & 0 & -i\tilde{\gamma}_e & \frac{\Omega}{\sqrt{2}} & 0 \\ 0 & 0 & \frac{G}{2} & \frac{\Omega}{\sqrt{2}} & -i\frac{\tilde{\gamma}_e+\gamma_r}{2} & \frac{\Omega}{\sqrt{2}} \\ 0 & 0 & 0 & 0 & \frac{\Omega}{\sqrt{2}} & -i\gamma_r \end{pmatrix}$$

where $\tilde{\gamma}_e \equiv \gamma_e + 2i\delta_e$ is a complex linewidth incorporating the P-state detuning. The above basis and corresponding Hamiltonian no longer accurately describe the physics once the Rydberg-Rydberg interactions become comparable to the dark-bright splitting: under such conditions, the $|RR\rangle$ is renormalized due to Zeno suppression of excitation of Rydberg-atom-pairs at small separation. We posit that the model can be "fixed" by considering coupling to a new collective "two-Rydberg" state $|\widetilde{RR}\rangle$, where the tilde signifies that the relative two-Rydberg amplitudes are renormalized by interaction; furthermore, the coupling from $|ER\rangle$ to $|\widetilde{RR}\rangle$ will no longer be $\frac{\Omega}{\sqrt{2}}$.

To ascertain the form of the state $|\widetilde{RR}\rangle$, we will examine the equations of motion *in the frequency domain* under the non-Hermitian Hamiltonian in the bare-atomic basis within the two- excitation manifold. We work in a frame that rotates with an energy $2\Omega_p$, convenient

for performing scattering experiments of pairs of photons injected by a probe at energy Ω_p. We assume that while the state $|RR\rangle$ is renormalized by the interactions, the state $|ER\rangle$ is *not*, and reflects the non-interacting polaritonic wave-functions of the preceding sections; this is the central assumption of this section, and is validated by numerics. Corrections to $|ER\rangle$ would enlarge the Hilbert space and may be included as higher-order terms in the effective theory.

Following notation from [34] SI L, the equation of motion for the amplitude of two Rydberg excitations in atoms α and β, $C_{RR}^{\alpha\beta}$, is given by $i2\Omega_p C_{RR}^{\alpha\beta} = i\left(U_{RR}^{\alpha\beta} + 2\delta_2 + i\gamma_r\right) C_{RR}^{\alpha\beta} + i\Omega\left(C_{ER}^{\alpha\beta} + C_{RE}^{\alpha\beta}\right)$, where $U_{RR}^{\alpha\beta}$ is the interaction between Rydberg-excited atoms α, β, δ_2 is the two-photon detuning, γ_r is the Rydberg state linewidth and we have assumed that the control field Ω is uniform across the atomic ensemble. Here $C_{ER}^{\alpha\beta}$ and $C_{RE}^{\alpha\beta}$ are the amplitudes to have P- and Rydberg- excitations in atoms α, β and β, α, respectively, and satisfy $C_{ER}^{\alpha\beta} = C_{RE}^{\beta\alpha}$. The assumption that $|ER\rangle$ is not renormalized by the interactions is equivalent to $C_{ER}^{\alpha\beta} = \frac{g_\alpha g_\beta}{\sum_\nu |g_\nu|^2}$, where g_χ is the vacuum-field light-matter coupling strength of atom χ. Plugging this expression into the equation of motion for $C_{RR}^{\alpha\beta}$ yields the un-normalized two-Rydberg state amplitude: $C_{RR}^{\alpha\beta} = \frac{\Omega \frac{g_\alpha g_\beta}{\sum_\nu |g_\nu|^2}}{\left(U_{RR}^{\alpha\beta} + 2\tilde{\delta}_r\right)}$, where we defined the complex detuning $\tilde{\delta}_r = \delta_2 + i\frac{\gamma_r}{2} - \Omega_p$. We can now write the normalized collective state $|\widetilde{RR}\rangle$, its effective interaction energy $\tilde{U}$ and effective coupling $\frac{\tilde{\Omega}}{\sqrt{2}}$ to $|ER\rangle$ as:

$$
\begin{aligned}
|\widetilde{RR}\rangle &= \frac{\sum_{\alpha\beta} \frac{g_\alpha g_\beta}{U_{RR}^{\alpha\beta}+2\tilde{\delta}_r}|R_\alpha R_\beta\rangle}{\sqrt{\sum_{\mu\nu}|\frac{g_\mu g_\nu}{U_{RR}^{\mu\nu}+2\tilde{\delta}_r}|^2}}, && (3.6.1)\\
\tilde{U} &= \langle\widetilde{RR}|U|\widetilde{RR}\rangle \\
&= \frac{\sum_{\alpha\beta}|\frac{g_\alpha g_\beta}{U_{RR}^{\alpha\beta}+2\tilde{\delta}_r}|^2 U_{RR}^{\alpha\beta}}{\sum_{\mu\nu}|\frac{g_\mu g_\nu}{U_{RR}^{\mu\nu}+2\tilde{\delta}_r}|^2}, && (3.6.2)\\
\frac{\tilde{\Omega}}{\sqrt{2}} &= \langle\widetilde{RR}|\sum_j \frac{\Omega}{2}\left(\sigma_{er}^j+\sigma_{re}^j\right)|ER\rangle \\
&= \frac{\frac{1}{\sqrt{2}}\Omega\sum_{\alpha\beta}\frac{|g_\alpha g_\beta|^2}{U_{RR}^{\alpha\beta}+2\tilde{\delta}_r}}{\sqrt{\sum_{\mu\nu}|\frac{g_\mu g_\nu}{U_{RR}^{\mu\nu}+2\tilde{\delta}_r}|^2}\sqrt{\sum_{\mu\nu}|g_\mu g_\nu|^2}}. && (3.6.3)
\end{aligned}
$$

In the extreme limit of strong interactions across all space $U_{RR}^{\alpha\beta} \gg \tilde{\delta}_r$: $\tilde{U} = \frac{\sum_{\alpha\beta}\frac{|g_\alpha g_\beta|^2}{U_{RR}^{\alpha\beta}}}{\sum_{\mu\nu}\frac{|g_\mu g_\nu|^2}{\left(U_{RR}^{\mu\nu}\right)^2}} = \frac{C_6}{w_c^6}\frac{\int \mathrm{d}\tilde{A}\mathrm{d}\tilde{A}' e^{-2(\tilde{r}^2+\tilde{r}'^2)}\tilde{d}^6}{\int \mathrm{d}\tilde{A}\mathrm{d}\tilde{A}' e^{-2(\tilde{r}^2+\tilde{r}'^2)}\tilde{d}^{12}} \approx \frac{1}{120}\frac{C_6}{w_c^6}$, where w_c is the mode waist; the pre-factor makes this interaction substantially weaker than one might naïvely anticipate- the interaction predominantly arises from particles separated by $\sim 2.2 w_c$, and not w_c.

We next benchmark the validity of this effective theory against a full microscopic numerical model [34]. As a figure of merit we have chosen the temporal intensity autocorrelation function $g_2(\tau)$, which compares the rate at which pairs of photons escape the resonator with separation in time of τ to what would be expected for uncorrelated photons escaping at the same average rate; in an experiment where our only access to the Rydberg physics is through photons leaking from the resonator, $g_2(\tau)$ characterizes the strength of polariton interactions, with $g_2(\tau = 0) \ll 1$ indicating strong interactions between intracavity photons. To remove the impact of the probe strength from $g_2(0)$, we consider a very weak probe; when the intracavity photon number is $\ll 1$, $g_2(0)$ is independent of probe strength. We compare

$g_2(0)$ vs. probe detuning δ_l (Fig. 3.4a), $g_2(0)$ vs. p-state detuning δ_e (Fig. 3.4b), light-matter coupling strength G (Fig. 3.4c), Rydberg control field strength Ω (Fig. 3.4d) and van der Waals interaction coefficient C_6 (Fig. 3.4e) between brute-force numerics of many individual three-level atoms and the effective theory developed above. It is apparent that our approach largely agrees with the full numerical model up to "noise" arising from randomness in the atom locations. We expect that residual deviations can be parametrized as corrections to $\tilde{\Omega}$ and $\tilde{U}$ due to coupling to bright-polariton manifolds, and a slight enlargement of the Hilbert space to incorporate the additional states coupled to.

We note that there are qualitative differences between the physical behaviour of resonator and free-space correlation functions, as demonstrated by our recent experimental work [34] and [19, 28, 33]. In a single-mode resonator coupled to Rydbergs, we have observed an effectively 0D environment by restricting the cloud thickness. This is equivalent to tunneling in and out of a zero dimensional quantum dot. On the other hand, free-space systems are intrinsically at *least* 1D; the photons can move longitudinally and avoid each other, experiencing a true position-dependent interaction. This difference in system dimension results in very different quantitative g_2 behavior and parameter scaling.

To explore more complex condensed matter models like Laughlin droplets and crystalline phases, multiple particles and resonator modes are needed. Any brute force analytical approach quickly runs into the obstacle of very large computation times due to the rapid increase of the system's Hilbert space. To circumvent this, we have developed a renormalized single- mode resonator effective field theory that shows very good agreement with numerics and can be extened to the many particle, multi-mode regime, allowing for computationally tractable modeling of larger physical systems.

3.7 Momentum-Space Interactions

A resonator which exhibits manifolds of nearly-degenerate modes may be understood as a self-imaging cavity: a localized spot living within such a manifold is re-focused onto itself after a full transit around the cavity. In-between, the localized spot undergoes diffraction, equivalent to the time-of-flight expansion of a free atomic gas [84]. Indeed, what the optics community calls a "fourier plane" is what a cold-atom experimentalist calls "momentum space": the momentum of the photon in the initial ("reference" or "image") plane has been mapped onto its position in the "fourier plane" [85]. We can formulate h_{phot} for any plane we choose to define as "real space". Placing a Rydberg-dressed atomic sample in that plane will produce real-space (position dependent) interactions in the system; a sample in any other place will result in interactions that are a mix between real- and momentum-space, depending on the exact plane the atoms are placed. Accordingly, it should be possible to realize interactions which are local in momentum-space by placing a Rydberg-dressed atomic-ensemble that mediates these interactions in a fourier- or nearly-fourier- plane of the optical resonator.

We explore this idea formally by extending the cavity Floquet Hamiltonian engineering tools of our prior work [11] to the interacting regime. A thin gas of Rydberg-dressed atoms placed in a plane separated from the "reference"/"image" plane by a ray-propagation matrix $M = \left(\begin{smallmatrix} \mathbf{a} & \mathbf{b} \\ \mathbf{c} & \mathbf{d} \end{smallmatrix}\right)$ produces interactions of the form:

$$H_{int} = \frac{1}{2}\sin^4\frac{\theta_d}{2}\iint \mathrm{d}x\ \mathrm{d}x' \chi_d^\dagger(x)\chi_d^\dagger(x')\tilde{V}\left(\mathbf{a}(x-x') - \frac{\mathbf{b}}{\hbar k}(\hat{p}-\hat{p}')\right)\chi_d(x')\chi_d(x). \quad (3.7.1)$$

In the simple case of a delta-interacting gas of atoms (for overlapping polaritons whose characteristic sizes exceed the blockade radius, an accurate but simplified model considers the long-range interacting polaritons as hard spheres; overlapping pieces of the polaritonic

wavefunction scatter) placed in such an intermediate plane (a distance z from the reference plane), we employ this result to transform an expression where the dark polariton creation/destruction operators and interaction potential are written in the intermediate plane to one where the interaction is transformed and all operators are written in the "reference" plane:

$$H_{int} = \frac{1}{2}\sin^4\frac{\theta_d}{2}\iint \mathrm{d}x\ \mathrm{d}x'\ \chi_d^\dagger(x;z)\chi_d^\dagger(x';z)\delta(x-x')\chi_d(x';z)\chi_d(x;z)$$
$$= \frac{1}{2}\sin^4\frac{\theta_d}{2}\iiint \mathrm{d}x\ \mathrm{d}\delta\ \mathrm{d}\Delta\ \chi_d^\dagger(x+\delta)\chi_d^\dagger(x-\delta)e^{i\frac{k}{2z}(\delta^2-\Delta^2)}\chi_d(x+\Delta)\chi_d(x-\Delta).$$

The resulting polariton interaction is no longer purely local in real-space, and indeed can "instantaneously" transport polaritons through space.

The most extreme example of such an interaction occurs if the mediating gas is placed in a fourier plane of the system, $a = 0, b = f$

$$H_{int} = \frac{1}{2}\sin^4\frac{\theta_d}{2}\iint \mathrm{d}x\ \mathrm{d}x'\ \chi_d^\dagger(x)\chi_d^\dagger(x')\tilde{V}\left(-\frac{f}{\hbar k}\left(\hat{p}-\hat{p}'\right)\right)\chi_d(x')\chi_d(x),$$

an interaction that is local in momentum-space.

3.8 Impact of Atomic Motion

In this section we investigate the effects of atomic motion on the coherence properties of individual Rydberg polaritons in both single- and multi-mode regimes. We relax the assumption, employed to this point in the manuscript, that the atoms remain spatially fixed, and instead allow them to move ballistically through space. The impact of this motion upon the P-state is ignored because the P-state linewidth of an alkali-metal atom ($\sim 2\pi \times 6$MHz) is typically

much larger than any Doppler broadening effect at μK temperatures ($\sim 2\pi \times 100$kHz for Rb), and furthermore, dark polaritons by construction spend very little time in the P-state (they are "dark" to it). In what follows, we will assume the polariton is almost entirely Rydberg-like (the typical experimental situation [34]; if this is not the case, all doppler-induced broadenings and cross-couplings must be multiplied by a factor reflecting the Rydberg-participation of a polariton $\sin^2 \frac{\theta_d}{2}$.

We incorporate atomic motion into the Hamiltonian in the bare-atom basis by allowing each atom to have a time-dependent coupling-phase to the probe and control fields resulting from its time-varying position:

$$\begin{aligned} H &= \omega_c \hat{a}^\dagger \hat{a} |c\rangle\langle c| + \sum_j \omega_e |e\rangle\langle e| + \omega_r |r\rangle\langle r| \\ &+ \sum_j \Big\{ \Big[G_j \left(x_j + v_j t\right) |e\rangle\langle c| + \Omega_j \left(x_j + v_j t\right) |r\rangle\langle e| \Big] + \text{h.c.} \Big\}, \end{aligned}$$

where x_j and v_j are the positions and velocities of the atoms, drawn from a normal distribution reflecting the sample r.m.s. size and temperature. The effect of atomic motion, then, is to mix the collective states that couple to the resonator modes with those that, in the absence of atomic motion, do not couple to it. To see this formally, we write the Hamiltonian in the basis of the instantaneous collective eigenstates, resulting in a Hamiltonian of the form:

$$H = \sum_m E_m(t) |m(t)\rangle\langle m(t)| + |\dot{r}(t)\rangle\langle r(t)|, \tag{3.8.1}$$

where $|m(t)\rangle, E_m(t)$ are the instantaneous polaritonic eigenstates and their corresponding energies, and $|\dot{r}(t)\rangle\langle r(t)|$ is an extra term introduced by this time-dependent change of basis,

capturing the effects of atomic motion in the instantaneous collective Rydberg state $|r(t)\rangle$. In what follows, we examine the form of this final term for the particular case of twisted resonators which produce a Landau level for light [12, 82], so the mode functions are Laguerre-Gauss $\Psi_l(z \equiv x+iy) = \sqrt{\frac{2^{l+1}}{\pi l!}} z^l e^{-|z|^2}$, with angular momentum $L = l\hbar$. For a polariton in a mode with angular momentum $l\hbar$, $|r(t)\rangle = |r_l(t)\rangle$, with $|r_l(t)\rangle = \frac{\sum_j e^{i\vec{k}\cdot(\vec{x}_j+\vec{v}_j t)}\Psi_l\left(\frac{\vec{x}_j+\vec{v}_j t}{w_c}\right)}{\alpha_l(t)}|j\rangle$, where $|j\rangle$ is the state where all atoms are in the ground state except for the j^{th} which is in the Rydberg state, and $\alpha_l(t) = \sqrt{\sum_j |\Psi_l\left(\frac{x_j+v_j t}{w_c}\right)|^2}$ is the normalization factor for mode l. The time derivative $\frac{d}{dt}|r_l(t)\rangle$ is:

$$\begin{aligned} |\dot{r}_l(t)\rangle &= \frac{\sum_j \vec{k}\cdot\vec{v}_j e^{i\vec{k}\cdot\vec{r}}\Psi_l\left(\frac{\vec{r}}{w_c}\right)}{\alpha_l(t)}|j\rangle \\ &+ |r_l(t)\rangle\left(-\frac{\dot{\alpha}_l(t)}{\alpha_l(t)}\right) \\ &+ \frac{\sum_j \frac{e^{i\vec{k}\cdot\vec{r}}}{w_c}\left(\vec{v}_j\cdot\vec{\nabla}_{\vec{r}}\right)\Psi_l\left(\frac{\vec{r}}{w_c}\right)}{\alpha_l(t)}|j\rangle, \end{aligned} \tag{3.8.2}$$

where the index $|j\rangle$ runs over all atoms in the sample, $\vec{r} = \vec{x} + \vec{v}t$, w_c is the resonator mode waist, k is the wavevector defined by the relative orientation of the cavity- and control- fields and $\vec{\nabla}_{\vec{r}}$ refers to the gradient with respect to $\vec{r}$. These terms of H in the instantaneous eigen-basis have three effects: mixing polaritons in modes of different angular momenta, coupling to bright polariton manifolds orthogonal to the resonator field, and random shifts of the energy of the mode in which the polariton resides. We now investigate the extent to which each of the terms above induce each of these effects. We can rewrite eq. 3.8.2 as $|\dot{r}_l(t)\rangle = |T_1\rangle + |T_2\rangle + |T_3\rangle$, where we have defined the following:

$$
\begin{aligned}
|T_1\rangle &= \frac{\sum_j \vec{k}\cdot\vec{v}_j e^{i\vec{k}\cdot\vec{r}_j}\Psi_l\left(\frac{\vec{r}_j}{w_c}\right)}{\alpha_l(t)}|j\rangle, \\
|T_2\rangle &= |r_l(t)\rangle\left(-\frac{\dot{\alpha}_l(t)}{\alpha_l(t)}\right), \\
|T_3\rangle &= \frac{\sum_j \frac{e^{i\vec{k}\cdot\vec{r}}}{w_c}\left(\vec{v}_j\cdot\vec{\nabla}_{\vec{r}}\right)\Psi_l\left(\frac{\vec{r}}{w_c}\right)}{\alpha_l(t)}|j\rangle.
\end{aligned}
$$

Even for a maximally degenerate concentric cavity, most collective Rydberg states that one can generate (for example through atomic motion, above) are orthogonal to all resonator modes, because their spatial form *along* the cavity axis does not match the cavity field (equivalently, their longitudinal momentum is not that of a cavity photon). As a consequence, most of the dynamics generated by coupling to $|T_1\rangle$, $|T_2\rangle$, and $|T_3\rangle$ consists of coupling to bright polariton manifolds with no corresponding dark (resonator-like) mode. We bound these effects by assuming, at zeroth order, that *all* of each coupling is to these bright manifolds. The strength of this coupling is thus the normalization of the corresponding $|T_i\rangle$ and in the case of $|T_1\rangle$:

$$
\begin{aligned}
\langle T_1|T_1\rangle &= \frac{\sum_j k^2 v_j^2 |\Psi_l|^2}{\alpha_l^2}, \\
\langle T_1|T_1\rangle^v_{t=0} &= (kv_{th})^2\frac{\sum_j |\Psi_l|^2}{\alpha_l^2} = (kv_{th})^2.
\end{aligned}
$$

We can now write $|T_1\rangle = kv_{th}\frac{|T_1\rangle}{kv_{th}} = kv_{th}|\tilde{T}_1\rangle$, where $|\tilde{T}_i\rangle$ is the normalized state-vector corresponding to state $|T_i\rangle$. This corresponds to a Rabi-coupling of strength $\sim kv_{th}$ to a bright polaritonic state which is detuned by Ω, and a resulting dark$\rightarrow$bright loss rate of:

$$\delta\Gamma_{T_1} = \frac{(kv_{th})^2}{\left(\frac{\Omega}{2}\right)^2}\frac{\gamma_e}{2} = \frac{2\,(kv_{th})^2}{\Omega^2}\gamma_e. \tag{3.8.3}$$

A small fraction of $|T_1\rangle$ overlaps with other degenerate resonator modes, corresponding to an atomic-motion-induced polaritonic motional diffusion:

$$\langle r_m(t)|T_1\rangle = \frac{\sum_p kv_p \Psi_m^*\left(\frac{r_p}{w_c}\right)\Psi_l\left(\frac{r_p}{w_c}\right)}{\sqrt{\sum_\mu |\Psi_l\left(\frac{r_\mu}{w_c}\right)|^2 \sum_\nu |\Psi_m\left(\frac{r_\nu}{w_c}\right)|^2}}.$$

The expected value of this term is zero since the average atomic velocity is zero: $\langle v_p\rangle_{t=0} = 0$. The r.m.s. coupling, however, is non-zero:

$$\sqrt{\langle|\langle r_m|T_1\rangle|^2\rangle_{p.}^{v.}} \;=\; \frac{kv_{th}}{\sqrt{N_0}}C'_{l\to m}, \tag{3.8.4}$$

where N_0 is the number of atoms in mode l =0 and $C'_{l\to m} = \frac{C_{l\to m}}{\sqrt{\sqrt{lm}}} = \sqrt{\frac{2^{1-l-m}\frac{(l+m)!}{l!m!}}{\sqrt{lm}}}$ is a generalized the Doppler coupling matrix element between modes l and m, incorporating the fact that higher angular momentum modes contain more atoms, and thus provide a smoother atom distribution. We can expand this matrix element for large $l \approx m$ yielding $C_{l\to m} \approx e^{-(l-m)^2/2l^2}\frac{\sqrt{2}}{(\pi l)^{1/4}}$, indicating diffusion only into nearly-adjacent modes.

Last, the r.m.s. energy shift (inhomogeneous broadening) of the collective Rydberg state induced by this term is given by:

$$\sqrt{\langle|\langle r_l|T_1\rangle|^2\rangle_{p.}^{v.}} \;=\; \frac{kv_{th}}{\sqrt{N_0}}\sqrt{\frac{2^{1-2l}(2l)!}{l(l!)^2}}. \tag{3.8.5}$$

The second term of eq. 3.8.2 is:

$$|T_2\rangle = |r_l\rangle \frac{1}{2w_c} \frac{\sum_n \vec{v}_n \cdot \vec{\nabla}_{\vec{r}} |\Psi_l|^2}{\alpha_l^2} = |r_l\rangle \left(-\frac{\dot{\alpha}_l}{\alpha_l} \right).$$

Again, we examine how this term couples a dark polariton to the lossy manifold of bright polaritons:

$$\sqrt{\langle T_2 | T_2 \rangle} = \frac{v_{th}}{2w_c} \frac{\Gamma(l+\frac{1}{2})}{l!} \approx \frac{v_{th}}{2\sqrt{l+\frac{1}{3}} w_c}. \tag{3.8.6}$$

This broadening comes from the time-dependent probe field coupling that the atoms experience as they move within the mode; it is much smaller than kv_{th}. From the functional form of $|T_2\rangle$ we can also see that it does not couple modes of different angular momenta $\left(\langle r_m | T_2 \rangle = \delta_{l,m} \left(-\frac{\dot{\alpha}_l}{\alpha_l} \right) \right)$.

The third term, similar to the first, produces both a broadening and a shift in the dark polariton energy. We can see that this term couples to the bright collective manifold with matrix element:

$$\sqrt{\langle T_3 | T_3 \rangle} \;\; = \;\; \frac{v_{th}}{w_c} \sqrt{3l+1}. \tag{3.8.7}$$

We can similarly evaluate how this term couples to other states in the dark collective-state manifold:

$$\langle |\langle r_m | T_3 \rangle|^2 \rangle_p^v \;\; = \frac{v_{th}^2}{w_c^2} \frac{1}{N_0} \left(C''_{l \to m} \right)^2, \tag{3.8.8}$$

where $C''_{l\to m} = \sqrt{\frac{2^{-l-m}(l+9l^2+m+2lm+m^2)\Gamma(l+m)}{l!m!\sqrt{lm}}}$ is the coupling element between modes of the resonator that captures mode spatial overlaps, coupling induced by atomic motion and increasing mode area. This cross-thermalization coupling element converges for large $l \approx m$ to $C''_{l\to m} \approx \sqrt{\frac{6}{\sqrt{\pi}}} l^{-\frac{1}{4}} e^{-(l-m-\frac{11}{6})^2/8l}$. The l dependence in both the broadening and energy shift terms arises from the more rapid phase accrual of higher angular momentum modes.

The total broadening of a mode with angular momentum l is thus $\Gamma_l^{Doppler} \approx 2\frac{(kv_{th})^2}{\Omega^2}\gamma_e \left(1 + \frac{3l+1}{(kw_c)^2}\right)$; the r.m.s. Rabi-coupling of mode l to mode m is $|\Omega_{lm}| \approx (\frac{4}{\pi})^{\frac{1}{4}} \frac{kv_{th}}{\sqrt{N_0 l_0}} e^{-\delta l^2/2l_0} \sqrt{1 + \frac{\sqrt{9l_0}}{(kw_c)^2}}$, where $2\delta l \equiv l - m$, $2l_0 \equiv l + m$. Noting that $kw_c \approx 100$ for typical experiments [34], approximating further yields: $\Gamma_l^{Doppler} \approx 2\frac{(kv_{th})^2}{\Omega^2}\gamma_e$, $|\Omega_{lm}| \approx (\frac{4}{\pi})^{\frac{1}{4}} \frac{kv_{th}}{\sqrt{N_0 l_0}} e^{-\delta l^2/2l_0}$. In fact, summing over all final states, the net coupling out of mode l is $|\Omega_l| \approx (16\pi)^{1/4} \frac{kv_{th}}{\sqrt{N_0}}$, independent of l.

To summarize, atomic motion results in homogeneous and inhomogeneous broadening of the dark polaritons, along with state diffusion. All effects arise from recoil-induced differential motion of the Rydberg-excited atom, expressed as $\dot{r}_l(t)$: the first couples (eqn's 3.8.3, 3.8.6, 3.8.7) the system to modes that decay into free space due to their spatial symmetry, while the second term (eqn's 3.8.4, 3.8.8) quantifies thermalization of atomic degrees of freedom into the polaritonic degrees of freedom as a result of atomic motion. The former effect is suppressed by the detuning of the uncoupled (and therefore bright) modes from the dark manifold, while the latter effect is suppressed because atomic motion is random, so it is only the shot-noise in the motion of the ensemble comprising the polariton that leads to polaritonic mode coupling.

Doppler decoherence fundamentally arises from the relative motion of the atoms comprising the matter-component of a polariton relative to the field comprising the photonic component; as a consequence, the Doppler decoherence is sensitive to the *canonical* momentum of the optical field, not its *mechanical momentum* [11]. This distinction is particularly important in cavities whose near-degenerate manifolds represent a particle in a magnetic

Doppler Decoherence Summary		
	Broadening	Cross thermalization
T_1	$2\frac{(kv_{th})^2}{\Omega^2}\gamma_e$	$(\frac{4}{\pi})^{\frac{1}{4}}\frac{kv_{th}}{\sqrt{N_0 l_0}}e^{-\delta l^2/2l_0}$
T_2	$\frac{3}{2(3l+1)}\frac{(v_{th}/w_c)^2}{\Omega^2}\gamma_e$	0
T_3	$2(3l+1)\frac{(v_{th}/w_c)^2}{\Omega^2}\gamma_e$	$(\frac{4}{\pi})^{\frac{1}{4}}\frac{v_{th}}{w_c\sqrt{N_0 l_0}}(9l_0)^{\frac{1}{4}}e^{-(\delta l-\frac{11}{12})^2/2l_0}$

Table 3.1: Atomic motion induced homogeneous/inhomogeneous broadening, as well as r.m.s. diffusion/cross-thermalization matrix elements. For broadening terms, the angular momentum of the state under consideration is l; for cross-thermalization we consider nearby angular momentum states with mean l_0 and separation $2\delta l$. Computed broadening and cross-thermalization terms are upper bounds on the respective processes. Note that $kw_c \approx 100$ for typical experiments [34], so kv_{th} terms dominate strongly over v_{th}/w_c terms until l becomes large.

field, because although the Landau level is translationally invariant in a fundamental sense, the choice of gauge arising from resonator twist means that polaritons further from the resonator axis are more susceptible to Doppler decoherence, apparent in the l-dependence of the loss terms above.

3.9 Outlook

In this chapter we have presented a field theory of interacting cavity polaritons in the strongly interacting regime, including a formal treatment of interaction and atomic-motion-induced loss channels, and the development of a renormalized single-mode theory. We also demonstrate that by varying the location of one or more Rydberg-dressed atomic ensembles within the resonator, the interactions can be tuned continuously from local in position-space to local in momentum-space.

A particular non-planar resonator configuration yields a degenerate set of Laguerre-Gaussian eigenmodes which corresponds to a Landau level for photons [12]. Hybridizing these modes with Rydberg atoms to introduce strong interactions between photons makes this is a promising platform to study fractional quantum Hall physics [86–89]. Straightfor-

wardly extending our current single-mode effective field theory to include multiple resonator modes and particles, analogous to its free-space counterpart [73], allows us to model this platform and make quantitative predictions for future experimental explorations of fractional quantum Hall physics.

Furthermore, by combining a renormalized cavity-Rydberg-polariton field-theory with recently demonstrated cavity Rydberg polariton Keldysh-techniques [90], we are now in a position to accurately model the physics of cavity polariton crystals and Laughlin puddles [69], plus quantitative analysis of photonic QIP and quantum repeater protocols [91, 92].

CHAPTER 4

EXPERIMENTAL SETUP

Previous chapters have discussed the properties and interactions of both bare Rydberg atoms and resonator Rydberg polaritons. In this chapter I will describe the experimental setup that has allowed us to see such interactions and is suitable for exploring topological photonic quantum many-body physics. Our experimental system has many constraints; this is due to the intrinsic sensitivity of Rydberg atoms to stray electric fields which makes very precise control of electric fields and gradients an absolute necessity. Furthermore, the design parameters needed to create a resonator that exhibits non-trivial topology for photons and can support strong polariton interactions further constricts the space of available non-planar cavities.

On the other hand, using cavity Rydberg polaritons has its advantages too. The dynamics of our quasi-particles are governed by their photonic components and are therefore very fast. Rydberg atoms are very long-lived (their linewidth is on the order of 100 kHz and still improving) and interparticle effective interactions are on the order of MHz. Comparing these numbers to atoms in an optical lattice which have typical lifetimes of seconds and interactions in the 100 Hz range (S-wave scattering), we see that polariton dynamics happen very fast compared to their lifetime, on the order of nanoseconds. This lifts some of the restrictions on the minimum pressure needed in the vacuum chamber, simplifying its design. Furthermore, any decoherence from atomic motion is fairly negligible, reducing any need for evaporative cooling. This, again, lets us tolerate a higher vacuum pressure and also speeds up the experimental sequence, since evaporative cooling is typically a very slow process on the order of seconds.

This chapter consists of four parts: the vacuum system, cavity design and philosophy, the laser system and sample preparation. The vacuum system describes the vacuum chamber and any special constraints or conditions we had to take into account. The resonator design section describes the cavity and the challenges and reasons that led to its current design.

The laser system section will focus on the general laser setup: the magneto-optical trap, cavity locks, transport lattice and the control laser. Then, I will discuss the procedure of preparing the sample, including compressing, cooling, transporting and slicing.

4.1 The Vacuum system

Cold atom experiments typically require very low vacuum chamber pressures to ensure a long sample lifetime. This is necessary because the lifetime of the atoms depends strongly on background pressure and needs to be significantly larger than the inverse of the interaction energy (neutral atom ground state S-wave scattering typically). This constraint is partially alleviated for us since the long-range Rydberg-mediated interactions in our system are strong enough that the relative lifetime-to-interaction energy requirement is easily satisfied. This means we can effectively work with pressures on the order of nanoTorr, orders of magnitude higher than typical BEC experiments [4].

The vacuum system setup is shown in Figure 4.1. The main chamber itself is an octagonal square: two 8" windows on the large flat sides are used for the horizontal MOT beams and to provide optical access for incoupling/outcoupling to the resonator, while another eight openings are located on the circumference of the chamber, four of them are 4.5" in diameter and the rest are 2.75". All of the 2.75" flanges have been covered with windows and the diagonal beams are passing through them. Two of the 4.5" flanges (top and bottom ones) are also covered with windows and are used to allow for lattice transport of the atoms from the MOT into the optical cavity and for general laser manipulation of the atoms. Finally, the last two horizontal flanges are used for connections to the rest of the vacuum system, including the turbo and ion pumps, ion gauge and various feedthroughs. It bears mentioning that we still have allowed for some optical access through those ports by placing windows at the far ends of the crosses connected to the chamber; while this severely limits the numerical aperture it still sufficient for MOT and lattice loading imaging.

The stringent requirements and complexity of our optical resonator (mounting, sufficient physical distance from the MOT beams and coils, electric field control for intracavity Rydberg atoms) forced us to design a custom flange that sits on top of the main chamber. It consists of a large flange at the top, used for optical access and tubes of various sizes extending radially outwards. The tubes are needed to connect the feedthroughs for the heating wires, cavity piezo and in-vacuum electrodes that let us precisely control atomic and cavity parameters. The custom flange also has some internal structure to aid in mounting the cavity inside the chamber and to allow for good control of any excess cable length.

4.2 The Optical Resonator

4.2.1 Four-mirror Resonator

Traditional two-mirror cavities have been use for a long time and are very well understood. Unfortunately, such resonators turned out to be impractical for us. Our need to have strong interparticle interactions means that our atoms have to be located in a small waist to achieve confinement within a single blockade volume; for the $100S$ Rydberg state this restriction corresponds to $\sim 10^3$ μm^3. Achieving the necessary waist size in a two mirror cavity proved to be impossible due to space constraints inside the vacuum chamber; the resonator would have to either be really long or have very long focal length mirrors, which in turn would make the cavity structure too tall and wide, blocking various beam paths inside the chamber.

The solution to this problem came in the form of a four-mirror cavity. A resonator with four mirrors differs mainly from a two-mirror one due to the fact that the cavity modes are running waves. The advantage of such a configuration is that a small waist suitable for interactions can be achieved at a much shorter cavity length and with reasonable mirror focal lengths. This is due to the bow tie geometry of the resonator; two of the mirrors are convex and their defocus acts as diffractive expansion, allowing for a small waist while keeping the

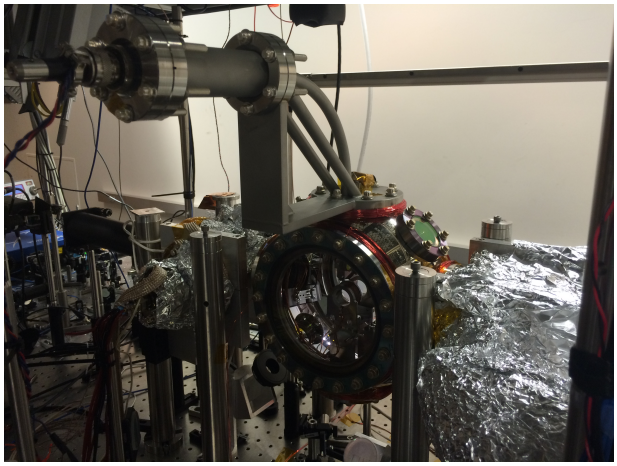

(a)

(b)

Figure 4.1: **Vacuum system Setup. (a)** Picture of the vacuum system. The vacuum chamber and an early iteration of a custom flange are visible. On the left, a connected feedthrough is visible. The right side of the vacuum system is wrapped in aluminum foil due to a recent bake. **(b)** The main chamber is an octagonal square: two 8" windows are located on the flat, short side and eight flanges on the circumference of the chamber, four 4.5" and four 2.75" flanges. The 8" windows and all four of the 2.75" windows are used for the MOT beams and their retroflections (the MOT beams are modeled as the gray tubes that can be seen in the CAD drawing). On the left and right side of the chamber we have electrical connections through feedthroughs and pumping through the turbo and ion pumps. Due to the complexity of the resonator, a custom flange was designed. It sits on the top flange of the chamber, allows for the cavity to be mounted at the right height inside the chamber and provides electrical access for the heating wire and piezo.

cavity length fairly short so it can still fit inside the vacuum chamber.

After a lot of numerical modeling and experimentation, we designed a resonator (shown in Figure 4.2a) with a 12.6 μm waist approximately 1 cm away from any surface. The upper mirrors of this structure are convex with a 50 mm radius of curvature and the two lower mirrors are concave with a 25 mm radius of curvature. A piezo was also attached to one of the lower mirrors to allow for tunable length and cavity locking. Both upper mirrors and the non-piezo lower mirror have a reflectivity of 99.9% at 780 nm and 1560 nm, coated by Layertec GmbH. The last mirror is coated by Advanced Thin Films, with a reflectivity of >99.995%. All mirrors are AR coated and high transmission for 480 nm. The theoretical finesse of the cavity (based on mirror coating specifications) is 2100 but due to contamination of the mirrors during the assembly and alignment procedures, the actual finesse is $F = 1480(50)$. A free spectral range of 2204 MHz has been measured with an EOM sideband and the polarization eigenmodes have a splitting of 3.6 MHz and are mostly linear.

4.2.2 Electric Field Suppression

As mentioned in Section 2.4, Rydberg atoms are very susceptible to electric fields and a good deal of the cavity design focused on both passive and active control and suppression of the electric fields throughout the atomic sample in the resonator. Passive suppression relies on the fact that the atoms are as far away as possible from any surface that can support charges and patch potentials; this includes the mirrors and the cavity structure itself. The resonator used to achieve strong polariton interactions has a distance of about 1 cm between the atoms and the closest surface to them, which is a factor of 10 more than previous iterations of our experimental cavities and is a significant improvement on polariton decoherence [72]. Active control is achieved by the eight screw-head electrodes mounted on the cavity structure around the atoms. On top of that, the cavity structure, which is two separate parts, can also be set to a voltage of our choice. Overall, this gives us ten degrees of freedom to control

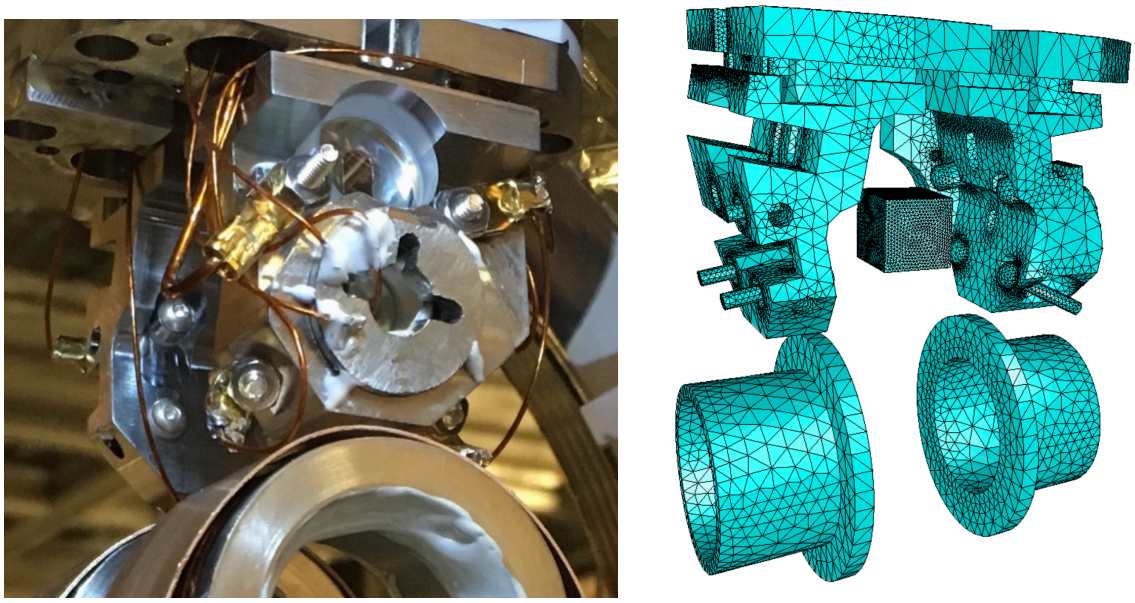

(a) (b)

Figure 4.2: **Cavity Structure. (a)** The cavity structure is mounted inside the vacuum chamber, right above the MOT coils. Two mirrors are clearly visible, one for the upper and one for the lower waist. Various electrode and heating wires are also visible: they are attached to multiple points on the cavity and then are carefully guided through the mounting structure to feedthroughs. **(b)** Finite element analysis model of the cavity. A 3D CAD model of the resonator is imported into a finite element analysis program to allow for electric field modeling and control. The structure itself, all electrodes and their macor (ceramic) spacers, the cavity length tuning piezo and MOT coils are all included in the modeling software. The atom are modeled by a cube that is evenly spaced from both ends of the cavity structure. By setting each invidual component to 1V while keeping everything else grounded and iterating over all components of the system, a transfer matrix is created relating the various voltages to electric fields and gradients at the atomic cloud's location.

eight independent electric fields and gradients, allowing for very precise control. To gain an understanding of how exactly to control the fields, we performed finite element analysis on a 3D CAD drawing of the cavity, shown in Figure 4.2b This allowed us to compute a transfer matrix, relating the voltage on each individual electrode we can control to an electric field or gradient at the atom location. We then computed an optimal set of values for this transfer matrix and experimentally observed the quadratic dependence of the EIT feature on the electric fields to verify we have correctly minimized the electric field environment around the atoms.

4.3 Laser Setup and Cavity Locking

4.3.1 Magneto-Optical Trap

The laser setup for the magneto-optical trap (MOT) is made of three lasers, the frequency reference, MOT beam and repumper laser, and a tapered amplifier. The frequency reference laser, also frequently referred to as the master laser, is a distributed feedback (DFB) diode in a custom mount that allows for fast feedback. An enriched Rb-87 cell is used to lock the laser to the $F = 2 \rightarrow F' = 2'/F = 2 \rightarrow F' = 3'$ crossover (shown in Figure 4.3), which is the most dominant feature in a doppler-free resonance spectrum. Since we want our MOT to use the $2 \rightarrow 3'$ atomic transition, we account for the frequency offset of the crossover locking point. We then lock the MOT and repumper lasers to the master laser using beat note locks. Two separate laser paths, which include both the MOT and repumper lasers, are used for the MOT itself: the horizontal path and the diagonal one, which is further split into two right before entering the chamber. Our path setup allows us to have the same intensity in each separate MOT path by splitting the power early on according to the diameter of each beam. Finally, the tapered amplifier is used to provide more power for the MOT beams; the repumper needs no amplification as very little power is required for it to repump efficiently

and keep the atoms in a closed transition loop.

4.3.2 Cavity Locking

The resonator needs to remain at a certain frequency to constantly match the ground to excited state transition frequency of the atoms; this allows any photon in the resonator to excite the atoms and become part of the polaritons we use. At the same time, Rydberg polaritons have a very narrow linewidth and any intrinsic laser frequency noise can potentially add to polariton decoherence. To solve both problems at the same time, we employ a transfer cavity locking scheme with a ultra narrow probe laser. First, we lock the probe laser to an ultrastable cavity from Stable Laser Systems (the cavity linewidth κ is 55 kHz and 41 kHz at 780 nm and 960 nm respectively); the cavity has been designed with thermal control and vibration isolation in mind. The probe laser is then fed through a fiber coupled electro-optical modulator (EOM) from EOSPACE, which allows for the generation of sidebands, before being coupled into the experimental cavity. The cavity can now be locked to the laser sideband, and in turn to the stable external cavity, and the cavity resonant frequency can be controlled by tuning the sideband frequency.

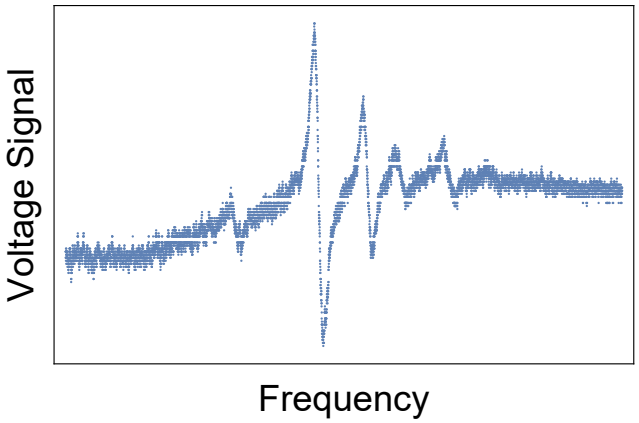

Figure 4.3: **MOT locking signal**. This signal is obtained by demodulating the Doppler-free spectrum of an enriched ^{87}Rb cell. The largest feature is the $F = 2 \rightarrow F' = 2/F' = 3$ crossover, located in frequency halfway between the $F = 2 \rightarrow F' = 2$ and $F = 2 \rightarrow F' = 3$ transitions. The MOT is locked to the zero crossing of the feature's downward slope.

4.3.3 Transport Lattice

A transport lattice is used to collect atoms after they have been prepared in the MOT and to transport them to the lower waist of the resonator. We use a laser that is locked to the ultrastable cavity through Pound-Drever-Hall and provides 700 mW of power at a red-detuning of 4 nm from the Rb D_2 line. The reason for the lock is twofold: as the laser drifts, it can go through multiple photo-association lines [93, 94] resulting in severe atom number loss, and DFB diodes, such as the one used for the lattice laser, are intrinsically broad [95]; electronic narrowing through a lock is needed to avoid parametric heating of the cloud [96]. The beam enters from the bottom of the chamber and is retroflected after exiting the chamber through the top window. The frequency of the reflected lattice beam is modulated before it enters the chamber. which creates a moving lattice that allows for atom transport.

4.3.4 Control Laser

We use a second-harmonic generation (SHG) laser setup to excite Rb atoms to the Rydberg state through a two-photon transition. Specifically, we use a TOPTICA TA-SHG-PRO 480 nm laser with a maximum of 480 mW of output power to excite the atoms. The setup consists of a 960 nm laser outputting 1 W, that gets frequency doubled in a cavity to 480 nm and at the same time retains a fairly large tuning of about 1 nm. A very small fraction of the 960 nm laser power gets picked off before the SHG stage and allows us to lock the laser to the ultrastable cavity. To avoid any inhomogeneous broadening of the polaritons, the waist of the control laser inside the resonator is ~ 45 μm, much larger than the 13 μm mode waist at 780 nm; that way the atoms experience the relatively flat and constant part of the Gaussian intensity profile.

4.4 Sample Preparation

As mentioned in the beginning of the chapter, Doppler broadening is fairly negligible for the polaritons, and so we can tolerate fairly high temperatures of ~ 10 μK. This allows us to get away with a simple polarization gradient cooling (PGC) scheme with no need for any compression or evaporative cooling. At the same time, it is important to mention that such temperatures are the limiting factor in terms of probing time inside the cavity due to cloud expansion.

We start preparing the atomic sample by trapping Rb released from getters in a MOT. We use a standard six beam MOT configuration, with three of the beams being retroflected. The MOT laser is red detuned by 23 MHz from the D_2 $2 \rightarrow 3'$ cycling transition, while the repumper laser is on $1 \rightarrow 2'$ to recover any atoms that off-resonatly scatter from $F' = 2$ to the ground state. The magnetic field of the trap is produced by in-vaccum anti-Helmholtz coils.

To achieve a uniform atom number in the MOT, the experimental sequence is run until the MOT atom number reaches its steady-state value. At this point, we turn off the magnetic fields and ramp the detuning of the MOT laser to 200 MHz away from the $2 \rightarrow 3'$ transition; this allows us to perform PGC [97–99]. It is necessary to have a zero magnetic field at the atoms' location and so three pairs of external bias coils are used to achieve good magnetic field control. The MOT and repumper lasers are on for another 10 μs after the magnetic field and laser detunings have arrived at their correct values. At this point, the cooling is complete and the cloud temperature is ~ 15 μK.

The next stage in getting the atoms ready for the experiment is transporting them up to the resonator. The distance between the MOT and lower cavity waist is 27 mm. While the PGC process is running, the transport lattice is already on; when the cooling is done about 30% of the atoms have been loaded into the lattice. To now move the atoms, two acousto-optical modulators (AOM) from IntraAction shift the frequency of the reflected lattice beam

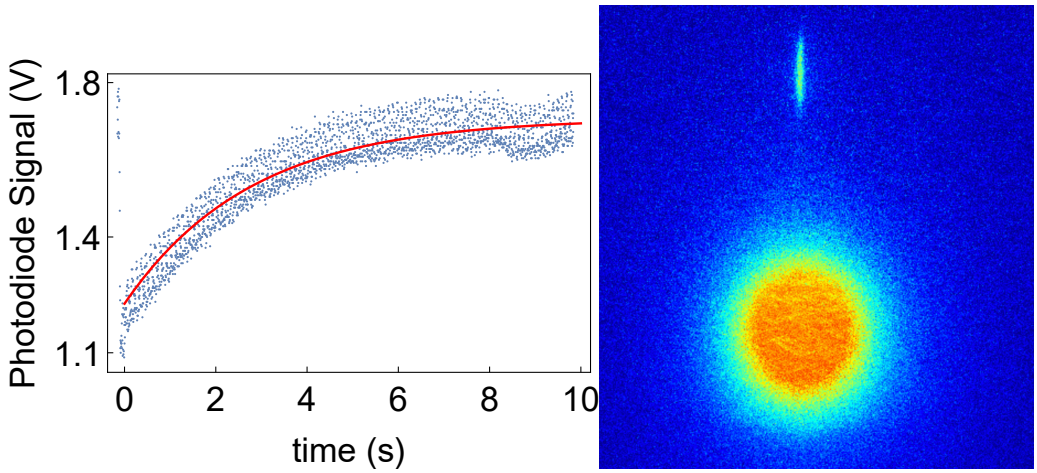

(a) (b)

Figure 4.4: **MOT loading and transport lattice. (a)** Experimental data of the MOT loading is plotted and fit. By collecting the fluorescence of the MOT at different times, the MOT loading can be observed. The blue points are experimental data and the red curve is a theoretical fit of the form $\frac{R-e^{-\gamma t R}}{\gamma}$, where R is the rate of atoms entering the trap and γ is the inverse lifetime of the trapped atoms. Overall this model describes the rate of atoms entering the trap minus the atoms lost due to collisions with background Rb atoms. The fit gives a MOT loading time/lifetime of $\tau = 7.44$ s. **(b)** The lattice is shown trasporting atoms out of the MOT. After loading the MOT and cooling the atoms, the lattice has been sufficiently loaded that it can be probed during transport. Due to the restricted access as we move up higher than the MOT, the MOT was allowed to fall for 3 ms to allow for better separation from the lattice. This image was created by capturing the fluorescence released when a 780 nm beam was shined on the lattice and MOT.

before it enters back into the chamber; this frequency mismatch between the two beams produces a moving lattice that transports the atoms. A frequency detuning of 10 MHz corresponds to an acceleration of $100g$ and a transport speed of 3.9 m/s. Figure 4.4b, obtained through fluorescent imaging, shows atoms being transported out of the MOT towards the cavity waist.

While the atoms are now in the cavity waist, the cloud's length along the cavity axis allows for multiple blockade volumes. As a result, stronger interactions (at the 100S Rydberg level) can only be achieved by trimming down the longitudinal cloud size. This additional confinement forces the atomic sample to exist within a single blockade volume, reducing

interparticle distance and boosting the interaction strength. The slicing procedure is depicted schematically in Figure 4.5. First, we shine a very large (500 μm waist) depump beam on the cloud. This beam is meant to bring all the atoms down to the $|F = 1\rangle$ ground state and is resonant with the $2 \rightarrow 2'$ transition. The next step is to repump only a narrow slice of the cloud. This is done by a repump beam along the vertical axis of the chamber (perpendicular to the cavity axis). This beam is tuned to the $1 \rightarrow 2'$ transition and is on for 2 μs. To finalize the slicing, a second depump beam with the spatial profile of a TEM_{10} mode is shined onto the atoms; the node is located on the cavity waist and so atoms near the waist experience no change in their state. After this final step, the atomic cloud has a thickness of 10 μm, much thinner than the previously 35 μm thick unsliced cloud.

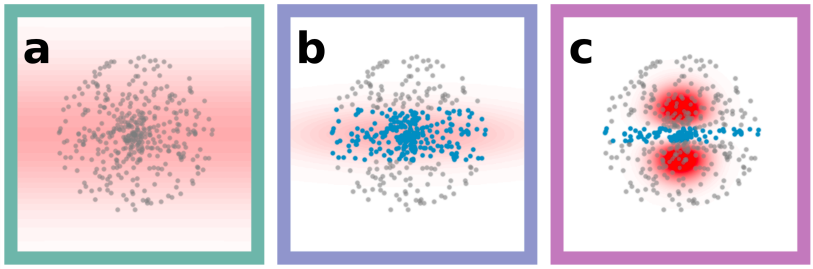

Figure 4.5: **Cloud Slicing Sequence.** **(a)** A large (500 μm waist) depump beam is shined on the atoms and depumps them to the $|F = 1\rangle$ ground state. This beam is on resonance with the $|F = 2\rangle \rightarrow |F' = 2\rangle$ transition. **(b)** A long vertical repump beam is switched on next, resonant with the $|F = 1\rangle \rightarrow |F' = 2\rangle$ transition. This beam is narrow in the resonator axis to only repump atoms in the center of the cloud. **(c)** A TEM_{10} like slicing beam is turned on, tuned to the $|F = 2\rangle \rightarrow |F' = 2\rangle$ transition. The node of the mode is aligned with the center of the cloud and spatially coincides with the resonator waist. After the slicing sequence, the cloud length is reduced to $\sim$ 10 μm. Gray atoms represent the $|F = 1\rangle$ groundstate and blue atoms represent the $|F = 2\rangle$ groundstate.

CHAPTER 5

CHARACTERIZATION OF CAVITY RYDBERG POLARITONS

Rydberg polaritons have emerged as very interesting quasiparticles for nonlinear quantum optics; they combine the tools available for cold atoms, such as lattice tuning [20] and Feshbach resonances [21, 61] with the precise control we can exert over photons and their Hamiltonians [11]. Such particles are a powerful tool for the study of quantum information processing [80, 100] and synthetic materials [56, 101].

Until recently, the only experimental observation of Rydberg polaritons had been in free space, where the polaritons have a longitudinal degree of of freedom [31, 75, 102]. Placing Rydberg polaritons in a resonator allows for trapping [13], synthetic magnetic fields [11, 69] and two-dimensional dynamics.

In this chapter I will go over our early experimental results that were obtained using our first four-mirror resonator. This involves creating and observing cavity Rydberg polaritons, exploring their dispersion and linewidth dependence on various experimental parameters. Then we will see how electric fields broaden the polaritons and can limit how high of a Rydberg state we can operate at, along with a brief discussion of how the situation can be improved. Finally, a proof of concept for multi-mode EIT will be presented, which combined with the right resonator geometry, can pave the way to manybody, multi-mode physics and experiments.

I will redefine the dark-state rotation angle in this chapter, making it inconsistent with the way it was defined in Section 3.3, but consistently so. While the polariton theory community has traditionally used the definition employed before, for our experimental work we have used

$$\tan\theta_d = \frac{G}{\Omega}. \tag{5.0.1}$$

From now on, when I mention θ_d, it will always be calculated using the second definition.

5.1 Rydberg Polariton EIT

Dark polaritons have been formally defined in Section 3.3. Before we start digging into the polariton behavior shown in the data, it might be instructive to look at what a cavity transmission spectrum looks like in the simple case of single-mode cavity Rydberg polariton EIT. This kind of spectrum is the backbone of our probing ability of the quasiparticles and a lot of information is encoded in it.

Rydberg EIT is a three-level system and this remains the case in a resonator as well. The three-level system produces three quasiparticles, the dark $|d\rangle$ and two bright $|b_\pm\rangle$ polaritons. Similarly, when we probe the cavity to look at its transmission spectrum, we expect to see three transmission peaks, corresponding to the three-level system and the three polaritons. Indeed, as is shown in Figure 5.1a, that is exactly the case. Three peaks, each one corresponding to a quasiparticle, are visible and separated in frequency space. In the case of no detunings, the dark polariton resonance is located at zero frequency, while the bright polaritons are evenly spaced around the central peak, separated by the vacuum Rabi splitting $\sqrt{G^2+\Omega^2}$. As explained previously, the dark polariton, being made up by the ground state/resonator photon and Rydberg state, is significantly narrower than the bright polaritons by an amount determined by the dark-state rotation angle (shown schematically in Figure 5.1b), which contain a large amount of the spectrally broad P-state.

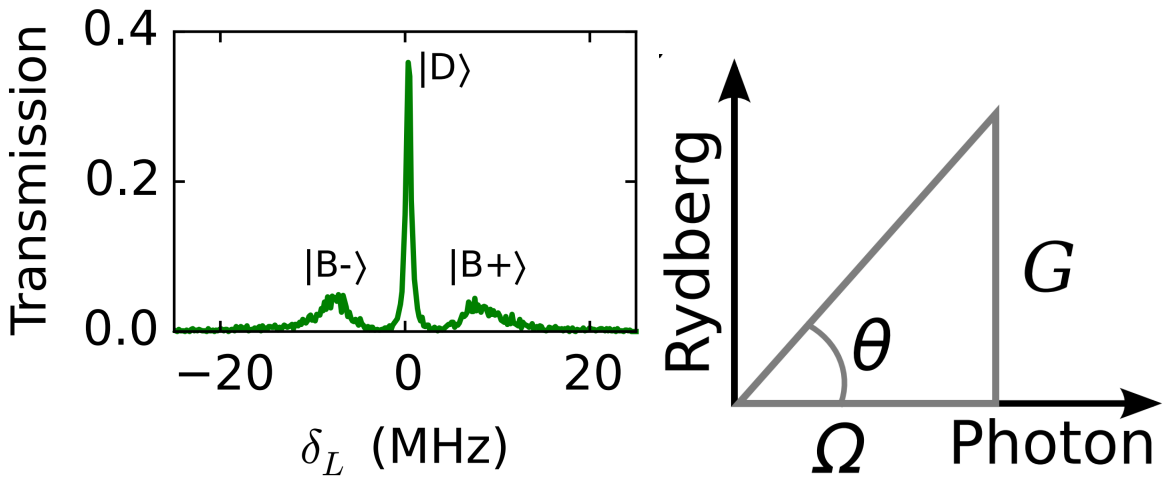

(a) (b)

Figure 5.1: **Cavity transmission spectrum and dark-state rotation angle. (a)** The cavity transmission spectrum as a function of probe detuning is shown as a fraction of the bare cavity transmission. The three peaks are the dark $|D\rangle$ and bright polaritons $|B\pm$. The dark polariton, containing no lossy P-state, is much narrower spectrally than the bright polaritons. Both bright polaritons are well separated from the central EIT peak by the vacuum Rabi splitting $\frac{\sqrt{G^2+\Omega^2}}{2}$. **(b)** The dark-state rotation angle θ_d is set by the light couplings G and Ω and can be used to describe the fraction of photonic and Rydberg components of the polaritons.

5.2 Polariton Dispersion

As mentioned above, cavity transmission spectrum were the most important data sets the first generation resonator produced. All of the polariton information is encoded in such spectra: Rydberg and cavity linewidths, experimental beam Rabi frequencies, dependence of polariton behavior on detunings. Furthermore, the main utility of polaritons depends on their lifetime: single-photon nonlinearities require interactions larger than the inverse lifetime [69] and many-body physics require long-lived polaritons for good resolution [103]. In this section, the slowing of polariton dynamics compared to bare cavity photons will be explored and the linewidth dependence on experimental parameters will be expanded.

To observe the dispersion relation of the polaritons, we probe the system while varying both probe detuning and cavity frequency. This is essentially a 2D version of Figure 5.1a

and allows us to see how the behavior of the polaritons' changes as their constituents change. More specifically, Figure 5.2 shows the dispersion relation as a function of probe and cavity detuning for three different dark-state rotation angles. As the polariton becomes more and more Rydberg-like, it follows the cavity frequency less and becomes flatter, as is expected from the first-order expression for the dark polariton energy [104]:

$$\delta_d = \delta_c \cos^2 \theta_d + \delta_r \sin^2 \theta_d. \tag{5.2.1}$$

At the same time, the cavity photon energy linearly follows the cavity frequency.

The dependence of the particles' lifetime can also be extracted by fitting the transmission spectra at each cavity detuning. To first order, the dark polariton linewidth is:

$$\gamma_d = \kappa \cos^2 \theta_d + \gamma_r \sin^2 \theta_d. \tag{5.2.2}$$

The physical origin of this expression is again the character of the polariton: it decoheres partially as cavity photons leaking out of the resonator or Rydberg atoms decaying back down to the P-state. Both the energy and the linewidth of the polariton as a function of dark-state rotation angle are shown in Figure 5.3a. The data points are in excellent agreement with the theoretical expressions above and the definiton of dark polaritons in Section 3.3, proving that the first order approximations are valid for single-mode, non-interacting polariton physics.

Introducing interactions or multiple resonator modes allowing for transverse dynamics can lead to a detuning away from EIT resonance; this is a decoherence channel that has not been previously experimentally explored. In Figure 5.3b, the polariton linewidth is plotted as a function of detuning from EIT resonance for the three dark-state rotation angles used in Figure 5.2. The results agree very well with the theoretical prediction of the extended

polariton decoherence [104]:

$$\gamma_d = \kappa \cos^2\theta_d + \gamma_r \sin^2\theta_d + a\left(\delta_c - \delta_r\right)^2, \tag{5.2.3}$$

where $a \equiv 4\frac{\Omega^2 G^2}{(G^2+\Omega^2)^3}\gamma_e$ is the strength of the quadratic term. From this expression, we can calculate the amount of detuning Δ needed to double γ_d:

$$\Delta = \frac{1}{2}\frac{\Omega^2}{\gamma_e}\sqrt{\frac{\kappa\gamma_e}{G^2}}\frac{1}{\cos^2\theta_d} = \frac{1}{2}\frac{\Omega^2}{\gamma_e}\frac{1}{\sqrt{OD}}\frac{1}{\cos^2\theta_d}, \tag{5.2.4}$$

where $OD = \frac{G^2}{\kappa\gamma_e}$ is the resonator enhanced optical depth.

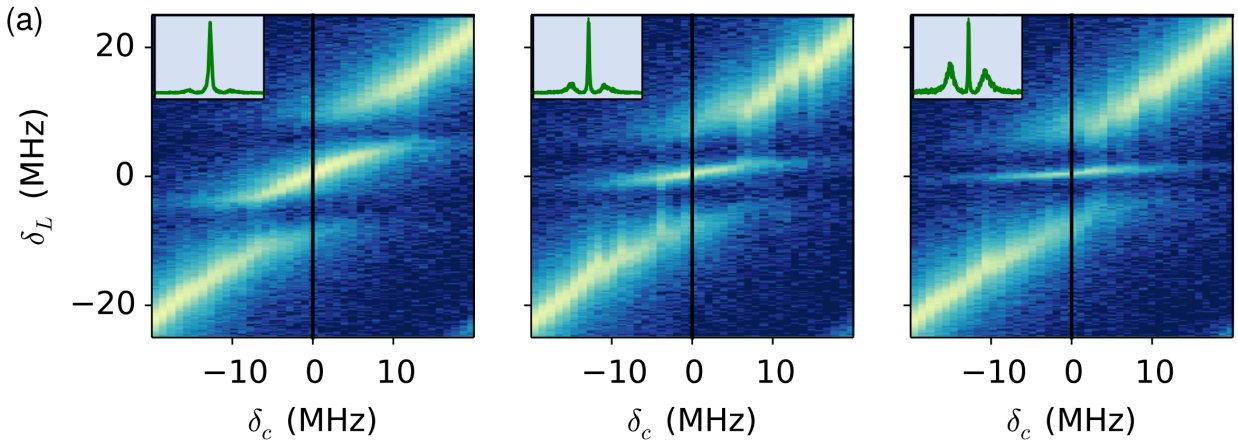

Figure 5.2: **Cavity Rydberg polariton dispersion.** Transmission spectra of the resonator are taken at different cavity detunings for various control laser powers. From left to right, Ω = 13.1(1),6.9(1),4.9(1) MHz and G = 12.3(2), 13.0(1), 14,7(1) MHz; this is equivalent to θ_d(deg)=43,62,72. The insets depict the spectra along the vertical black lines. We can see that from left to right. the dark polariton gets flatter and follows the cavity energy less and less. This is a direct result of its increasingly more Rydberg-like character.

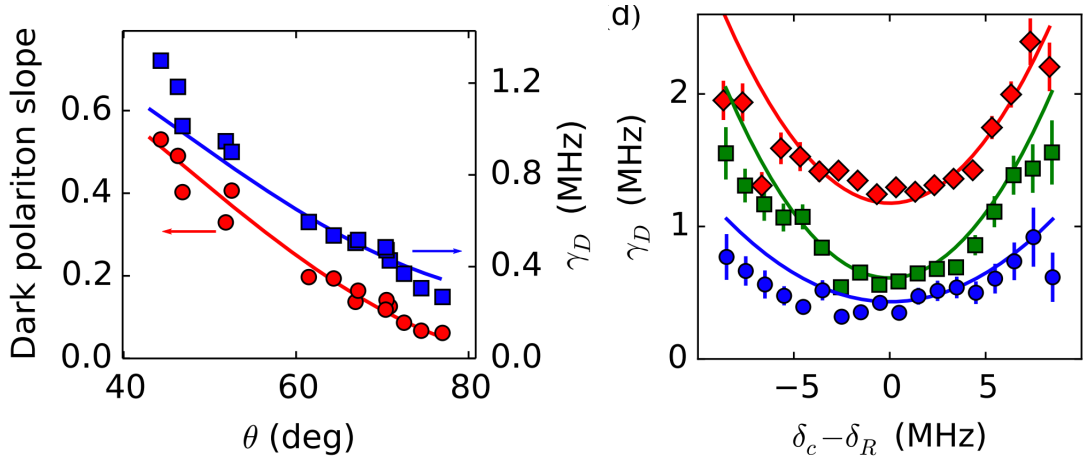

(a) (b)

Figure 5.3: **Dark polariton energy and linewidth.** **(a)** Energy and linewidth of the dark polariton vs dark-state rotation angle θ. The red circles, corresponding to the left axis, are the dark polariton slope $\frac{\mathrm{d}\delta_D}{\mathrm{d}\delta_c}$ and the blue squares, corresponding to the right axis are the dark polariton linewidth γ_D. The solid lines are theoretical predictions that use Ω from the control laser calibration and G from fitting the EIT transmission spectra. **(b)** Dark polariton linewidth dependence on the cavity detuning from EIT resonance. The colors correspond to the dark state rotation angles from Figure 5.2: red, green and blue correspond to left, middle and right respectively. The solid lines are the second-order prediction for the linewidth, with values for G and γ_r obtaining from fitting the transmission spectrum at zero detuning.

5.3 Electric Field Decoherence

As mentioned in Section 2.4, Rydberg atoms are very sensitive to electric fields compared to ground state atoms. Their large polarizability α is a direct result of their outermost electrons orbiting the core at a very large radius and so it scales rapidly with the principal quantum number, $\alpha \propto n^7$. Inhomogeneous electric fields are particularly notorious for inducing large polariton decoherence unless actively controlled; they are especially bad near surfaces due to patch potentials and surface charges [105].

In the case of individual atoms, even a massive inhomogeneous field would not matter much. At most, it would shift the Rydberg state by $\sim \alpha E^2$, where E is the electric field at the atom's location, something easily compensated for by adjusting the laser detunings. In the case of a collective excitation though, such as a cavity Rydberg polariton, each Rydberg

atom comprising the polariton would see a different field and get Stark shifted by a different amount. The end result is additional polariton broadening of the functional form $\gamma_b \sim \alpha E \delta E$, where δE is the electric field gradient across the atomic cloud.

The first iteration of our resonator greatly suffered from this: not only did we not think it important to passively or actively control electric fields near the atoms, the cloud was also located very close (less than 1 mm) to a metal surface surrounding it. Consequently, we very soon ran into really broad EIT peaks as the principal quantum increased, limiting how high of a state we could go to and precluding us from observing any interactions between the quasiparticles. Figure 5.4b shows the Rydberg linewidth vs polarizability, obtained by fitting the EIT spectra, indicating a very rapid increase in the width of the dark polariton. States with higher principle quantum numbers than the ones shown in the plot were so badly broadened that we could not even probe them through EIT.

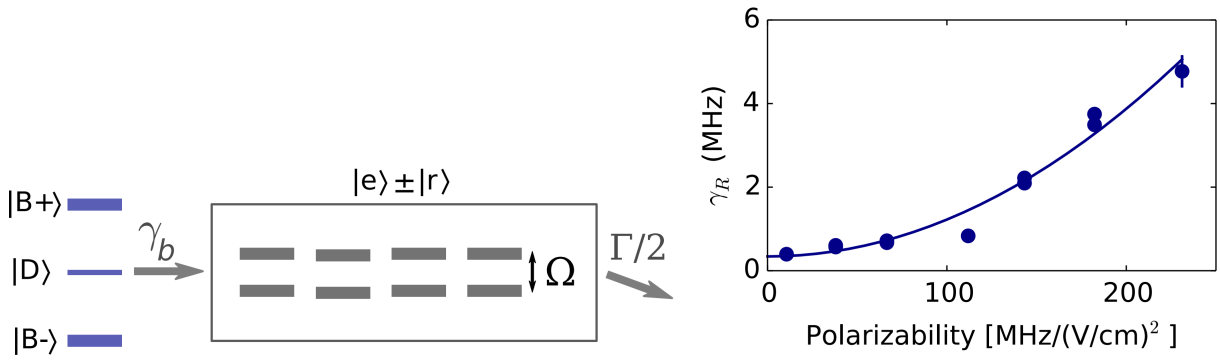

(a) (b)

Figure 5.4: **Control field suppression of electric field decoherence. (a)** Inhomogeneous broadening from background electric fields couples the dark polariton to a manifold of states that do live in the resonator. As such, these states are bright polaritons and share the fast decay of the P-state. The bright polariton manifold is detuned by $\frac{\Omega}{2}$ from the dark polariton and so this coupling is quadratically suppressed by the control field. **(b)** Decay rate of the Rydberg atoms vs polarizability (equivalent to principal quantum number). The quadratic suppression of the inhomogeneous electric field broadening is evident. The states used are n = 40,48,52,56,58,60,62. Ω =7.8(5) MHz, G=12(2) MHz. The solid represents a quadratic fit to the data.

There is one silver lining in this situation and that is how fast the decoherence scales with

polarizability (which can be easily mapped to principal quantum number). From the earlier expression for γ_b, one might expect a linear scaling of the polariton broadening with polarizability. As we can see in the data, the actual scaling during the experiment is quadratic. To understand the source of this suppression, we can look at what happens physically when the polaritons experience an inhomogeneous electric field. As the polaritons dephase, they off-resonantly couple to a continuum of bright polariton states. These polaritons are not the familiar bright polaritons (Equation 3.3.1) typically accompanying the dark polariton; they are instead the type of bright polaritons defined near the end of Section 3.3. This manifold of bright polaritons is a superposition of $|e\rangle$ and $|r\rangle$ states, has no coupling to the ground state/resonator and is detuned by $\pm\frac{\Omega}{2}$ from the dark polariton in the rotating frame. This effect is shown schematically in Figure 5.4a. For $\gamma_b < \gamma_e, \Omega$, the control field quadratically suppresses the polariton dephasing, that has the form $A\frac{\gamma_b^2}{\Omega^2}\gamma_e$; numerical simulations and data fitting show that A is of order unity. This is consistent with the theoretical prediction of Equation 3.3.3, where the extra factor of $\sin^2\theta_d$ signifies that the broadening refers to the polaritons.

5.4 Multi-mode EIT

Strong interactions can fully blockade the waist of a single mode resonator, allowing the creation of only a single polariton; this is explored in Chapter 6. Exciting physical phenomena, such as quantum crystals [69, 106–109] and fractional quantum Hall states [15, 89] are highly correlated state systems; they require multiple interacting quasiparticles. As such, multiple resonator modes are required to accommodate multiple strongly-interacting particles.

This version of the experimental cavity was designed with the TEM_{02} and TEM_{10} modes nearly degenerate [110]. having a separation $\delta_c = 20$ MHz. Tuning the resonator length allows for easy switching between single-mode physics in the TEM_{00} mode and multi-mode physics in the two-mode degenerate manifold, which is well separated from TEM_{00} in fre-

quency. The Floquet formalism [11] we have developed is particularly useful here for modeling and quantifying the behavior of massive photons in this degenerate resonator.

To show that we can have polariton EIT in both modes at the same time, we tune the nearly degenerate manifold to have its modes evenly spaced around the atomic resonance. We then inject light into both modes and collect the cavity output in a multi-mode fiber.

The experimental results are shown in Figure 5.5a. A cavity transmission spectrum has been plotted for the two-mode cavity polariton EIT; at first glance we can see that the dark polariton peaks are separated by much less than 20 MHz, an effect of the strong matter-light coupling. To understand how large the polariton splitting should be, we can consider each cavity mode separately; this is allowed because the atomic density is uniform across the cavity waist for both modes and therefore the modes do not mix and produce transmission spectra independently of each other. The splitting then will be suppressed by the dark state rotation angle:

$$\delta_d = \delta_c \cos^2 \theta_d, \tag{5.4.1}$$

plus higher order corrections in δ_C, as shown in Figure 5.5b.

5.5 Summary

In this chapter I have presented our early experimental results, which led to a great understanding of cavity Rydberg polaritons. The transmission spectrum of the cavity displays the three peaks expected from the three-level system that comprises the polaritons and the peak of interest, the dark polariton, is significantly narrower than the cavity linewidth, consistent with only a fraction of the polariton being photonic. Furthermore, the energy and decoherence of the polaritons shows the expected behavior with cavity and probe detunings and can

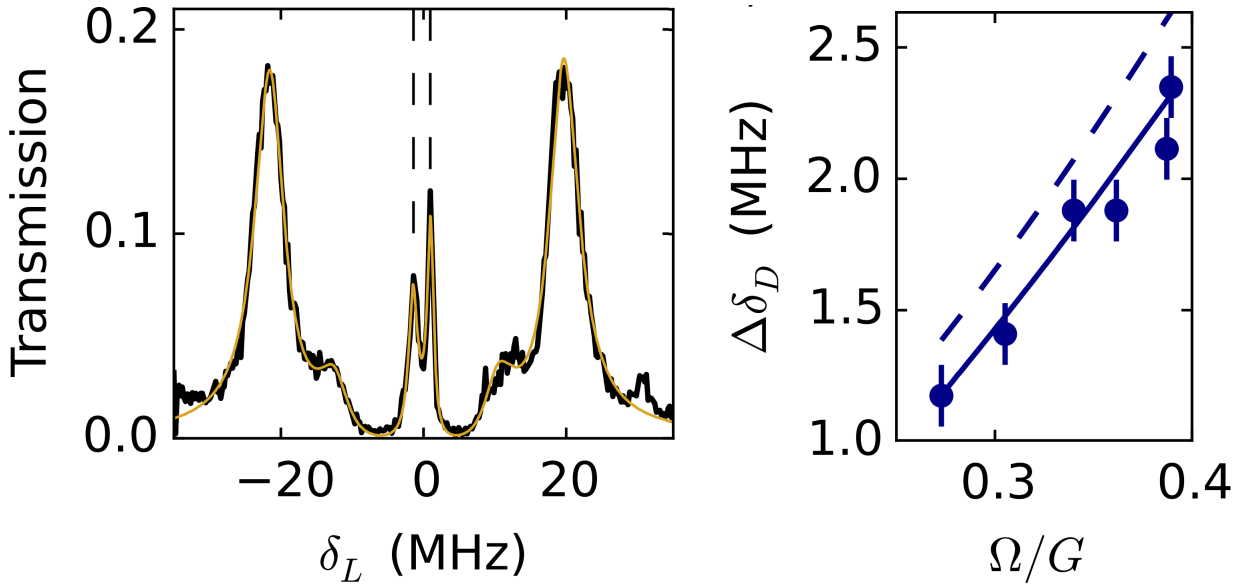

(a) (b)

Figure 5.5: **Multi-mode EIT. (a)** Two-mode EIT cavity transmission spectrum. The TEM_{02} and TEM_{10} modes are tuned to 10 MHz on either side of the EIT resonance. The two dark polariton resonances (dashed lines) are separated $\delta_d = 2.3$ MHz, a significantly smaller separation than the bare modes themselves. This frequency pulling is due to the composite character of the polariton, part photon and part Rydberg atom. The curve is a theoretical fit to a model with two orthogonal collective states. Here we used $\frac{\Omega}{G} = \tan\theta_d = 0.39$. **(b)**. Two-mode EIT dark polariton peak spacing as a function of $\frac{\Omega}{G}$. Changing the control laser power tunes the photonic component of the polaritons, affecting δ_d. The dashed line is a theoretical first-order prediction, while the sold line is the fit to the data points.

be tuned through the dark state rotation angle.

The stray electric fields present in the cavity proved to be detrimental by severely limiting the highest Rydberg state we could excite to and decohering any polaritons before they could interact. At the same time, that allowed us to gain a much better understanding of how the fields broaden the Rydberg atom and we developed a theoretical understanding of the observed quadratic electric field broadening suppression that agrees with the theory presented in Chapter 3.

Finally, a proof-of-concept multi-mode EIT spectrum was shown, which displayed frequency pulling of the polariton resonances. This is again consistent with the polaritons being

partially insensitive to resonator parameters due to their Rydberg constituents.

Combining the results of this chapter with interactions, which can be achieved by improving on the electric field background and going to higher Rydberg levels, and multiple degenerate resonator modes can allow for exotic phases of matter, such as Landau levels, quantum fluids and crystallization.

CHAPTER 6

STRONG POLARITON INTERACTIONS INSIDE A QUANTUM DOT

Recent efforts to overcome the technical challenges associated with producing strong photonic interactions using atoms have branched into two directions. The first involves using free-space Rydberg EIT [29, 111] to bypass the difficulties involved in manipulating atoms inside optical cavities. The second focuses on coupling atoms to the near field of photonic crystal cavities and waveguides [112–114]. The Rydberg EIT approach is particularly promising, as the atomic ensemble can act as a super-atom; it possesses the nonlinear properties of a single atom and the cross-section of the whole cloud. At the same time, such free-space polaritons [19, 28, 33] are limited by their longitudinal degree of freedom.

In this chapter I will describe the creation of a 0D quantum dot (the polaritons are both longitudinally and transversely confined) and the resulting strong polariton intereactions; this is an approach that combines both resonators and Rydberg EIT, using the strengths of each individual approach. The resonator enhances the light-matter coupling, allowing for large optical depths per blockade volume (OD_b) while relaxing the requirement of high atomic densities. This is a very large advantage over other systems, since the optical depth determines the number of scattering events during the polariton's lifetime. At the same time, Rydberg EIT provides very large, and well controlled, single atom nonlinearities.

The rest of the chapter is broken up into five sections: the preparation of the quantum dot and creation of dark and bright polaritons, nonlinear spectrosctopy of the dot, strong interactions between the polaritons, Rabi oscillations indicating that the quantum dot is indeed zero-dimensional and finally an outlook discussing applications and further directions for research.

6.1 Creation of the Quantum Dot

An ensemble of ~ 2500 atoms is loaded into the waist of single-mode optical resonator. The cloud size is $35 \times 41 \times 35$ μm^3, the resonator waist is 12.6 μm $\times$ 14.1 μm and the peak atomic density inside the resonator is 10^{11} cm^{-3}. While the cloud remains unsliced longitudinally for the spectroscopy measurements, it is reduced to a thickness of 10 μm along the cavity axis, as described in Section 4.4, to allow for strong interactions to manifest. The strong light-matter coupling now allows for the atoms and photons to hybridize, creating both dark and bright polaritons; for our typical experimental parameters $\tan\theta_d = 2.9$. Rydberg interactions scale very rapidly with principal quantum number (Section 2.5.1) and it is convenient for us to work with the $100S$ state since the resonator has been designed so that interactions at the Rydberg level make the blockade volume approximately the same size as the TEM_{00} mode waist. Further confining the atoms to a region smaller than the blockade volume inside the mode waist and the presence of only a single mode, which does not allow for transverse degrees of freedom, ensures that the quantum dot is zero-dimensional and will exhibit strong tunneling blockade (Figure 6.1a).

Spectroscopy, ring down and photon arrival times measurements for the autocorrelation function are all performed using a eight channel photon time-tagger, with a very high temporal resolution of 8ns on each channel (Figure 6.1b).

6.2 Spectroscopy of a polaritonic quantum dot

Once the atoms are prepared and loaded into the resonator, we probe the cavity and observe its transmission spectrum. The familiar three-peak is present: a central narrow peak, which corresponds to the dark polariton, and two wider peaks that are offset from zero frequency, the bright polaritons. The separation of the bright polaritons from the central peak indicates that we have indeed strong light-matter coupling, just like in Section 5.1.

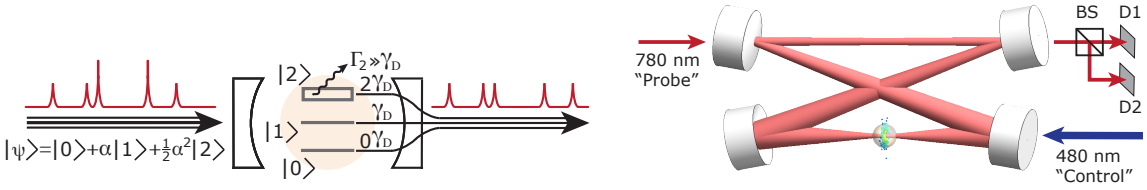

(a) (b)

Figure 6.1: **Strong interactions in a 0D quantum dot. (a)** The system exhibits the properties of a 0D quantum dot, due to longitudinal cloud slicing and transverse confinement through the resonator. The probe light is injected into the dot in the state $|\psi\rangle$; it primarily consists of zero photons, sometimes one and very rarely two. Each photon creates a dark polariton when it enters the cavity and its strong interactions shift the resonance frequency enough so that a second photon cannot enter. As a result, only single photons can leak out of the resonator. **(b)** The atomic cloud is transported into the smaller, lower waist of the resonator, where slicing occurs so that all atoms are within a single blockade volume. As 780 nm photons decay and leak out of the cavity, they are collected on single photon detectors D1 and D2, after passing through a 50:50 beamsplitter cube. The detected photons allow us to observer the strong repulsive interactions of the polaritons inside the resonator.

Even though the cloud is not sliced, the reduction in the electric field background and the high Rydberg state are sufficient to see some interactions. We qualitatively expect that injecting more photons into the resonator will result in more polaritons; even weak interactions can result in broadening and dephasing of the Rydberg polaritons. Indeed that is the case in Figure 6.2: as the probe power is increased, the EIT peak gets wider and shorter. This is a clear signature that the repulsive interactions of the 100S polaritons are not allowing additional photons to enter the quantum dot.

6.2.1 Electric fields in the quantum dot

As stated in Section 5.3, the uncontrolled electric fields dominated the Rydberg linewidth and were enough to dephase the polaritons before any interactions could take place. Our new resonator was designed with electric field considerations in mind: the atoms are located almost a factor of ten farther away from any surface (12 mm vs 1.5 mm for the old design), all dielectric surfaces are covered up as much as possible to reduce line of sight to the atoms

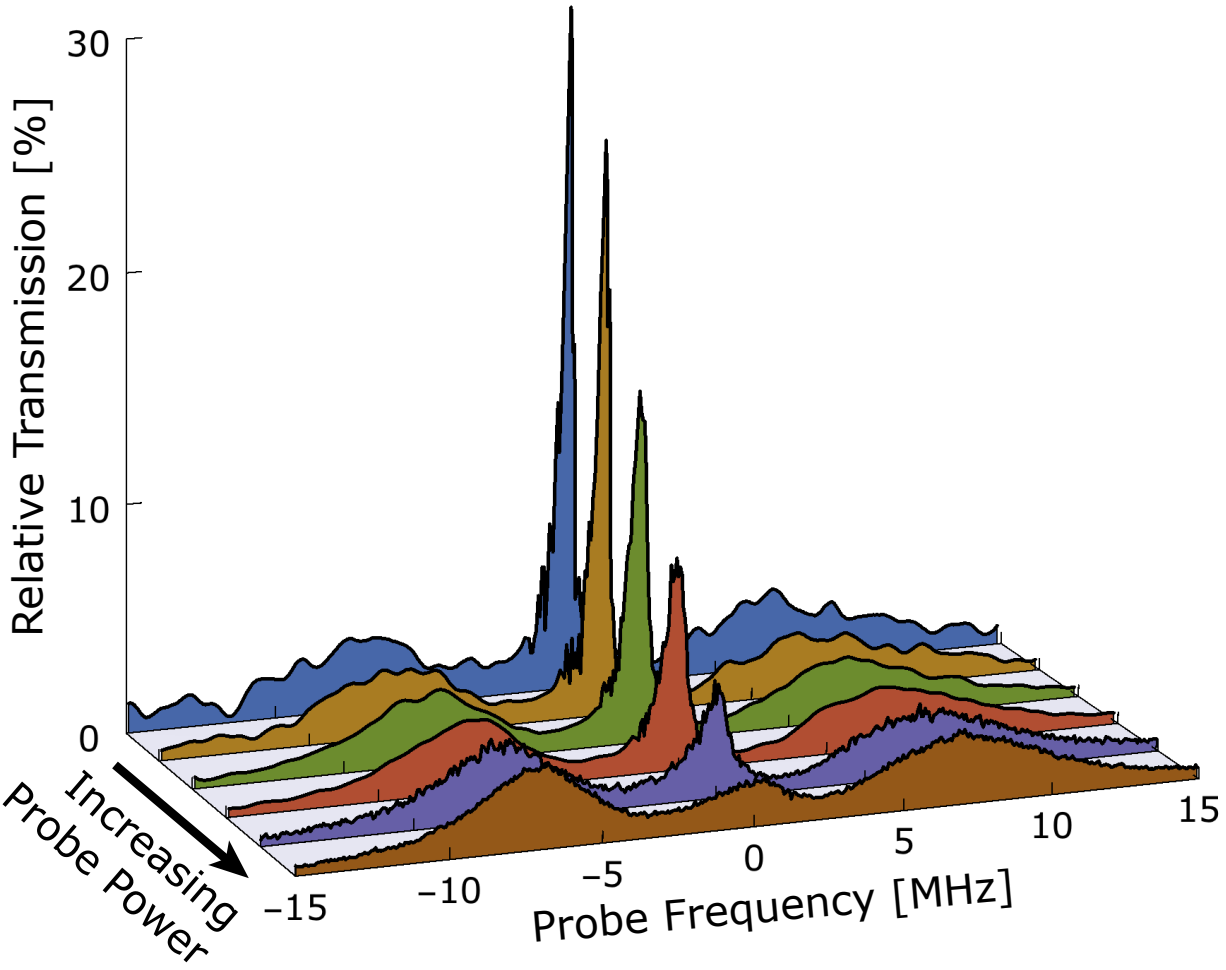

Figure 6.2: **Nonlinear spectroscopy of the quantum dot**. The transmission of the quantum dot is plotted relative to the bare cavity transmission as function of probe detuning for increasing probe power. Since the atomic cloud is still unsliced, it is not fully blockaded transversely or longitudinally; any interactions in the sample are weak. As a result, there's a smooth transition as the probe power increases and we can see the gradual broadening and suppression of the EIT peak. On the other hand, the bright polaritons peak heights and widths stay constant as a function of probe power. This is expected because their Rydberg fraction is extremely small and so they are insensitive to dipole-dipole interactions.

and protect them from trapped charges and a ten-electrode configuration (including the two parts that make up the resonator itself) can very precisely control the electric fields and gradients of the atoms. The DC electric field broadening of the Rydberg atoms is extracted from the quantum dot's transmission spectrum and compared to the broadening measured in the previous iteration of the optical resonator. The improvement is clear: even the lowest probed states in the original setup are as broad as the broadest Rydberg states in the new setup. This new precise electric field background control is an essential ingredient for the observed interactions explored in this chapter.

6.3 Observation of Polariton Interactions

Strong interactions inside the quantum dot can be probed through transport dynamics. Injecting a photon resonant with the dark polariton into the resonator creates a dark polariton. The strong, long-range interactions of this first polariton now shift the resonant frequency of the EIT transition and do not allow additional photons to enter since there is now a frequency mismatch. The figure of merit, or even the smoking gun, for strong interactions is the temporal intensity auto-correlation function $g_2(\tau)$ (Section 3.6), where τ is the delay time. A reduction near $\tau = 0$ indicates that double occupancy of the quantum dot is being prohibited due to interaction-driven loss.

To achieve such interactions, the cloud is sliced so that it is enclosed within a single blockade volume; this ensures that at most one polariton can live in the quantum dot. This leads to a very large suppression ($g_2(0) = 0.27$, shown in Figure 6.4a) of tunneling through the quantum dot for more than one quasiparticle; as long as one polariton is already inside the resonator, it will shift the resonant energy by more its linewidth, precluding additional photons from being injected while the first one still lives in the cavity. The experimental data agrees very well with a master equation theory fit [34].

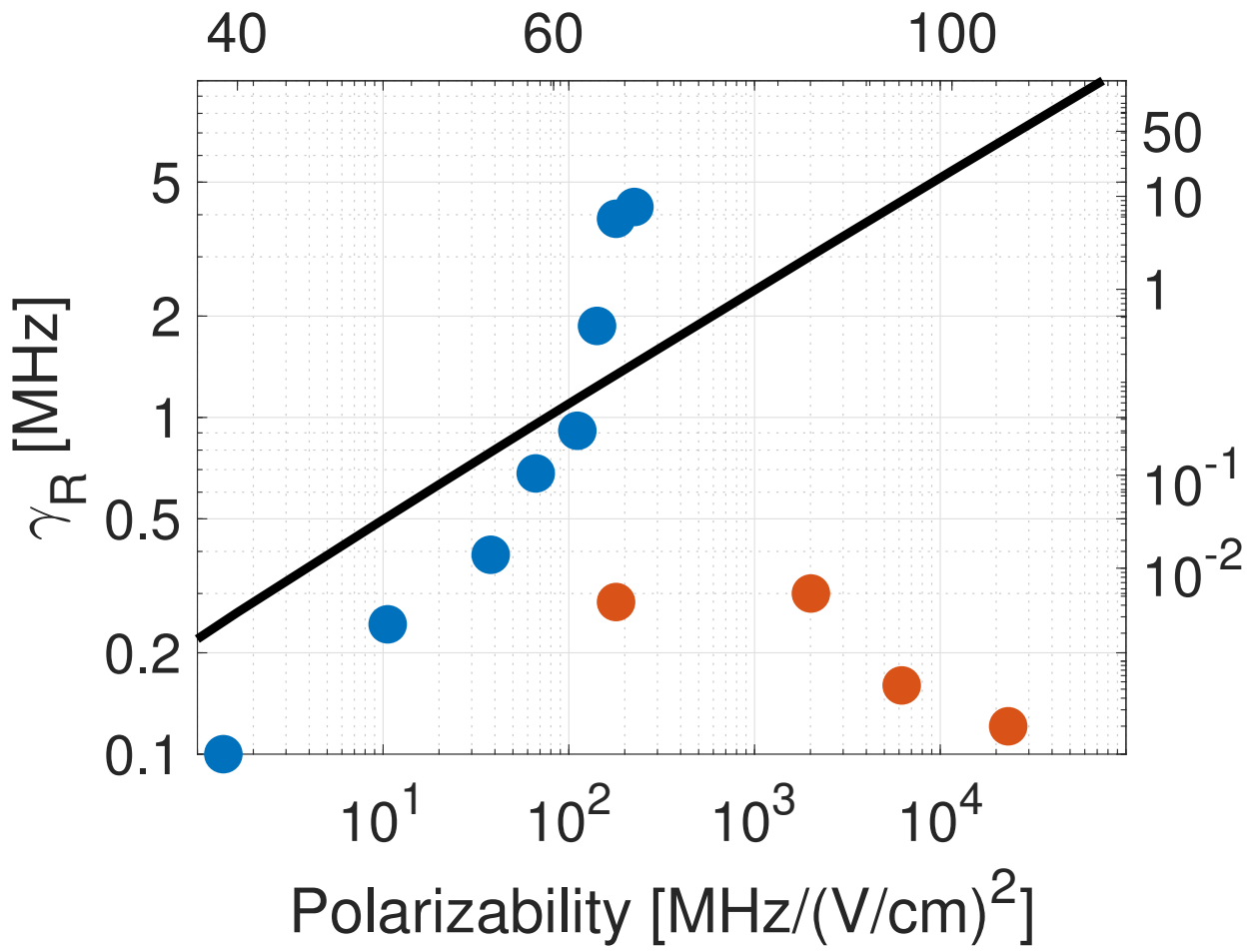

Figure 6.3: **Electric field broadening of the old and new cavities.** The transmission spectra of the resonator EIT allow us to extract the Rydberg linewidth resulting from electric fields. The blue points correspond to the first generation cavity used for our experiments and are identical to the data presented in Figure 5.4b. The red points represent the cavity strcuture. As we can see, compared to the old cavity, the linewidth of the Rydberg atoms not only does not increase with principal quantum number but actually decreases a little. This is great evidence pointing that the new electrode setup and passive field control are working and have been optimized correctly.

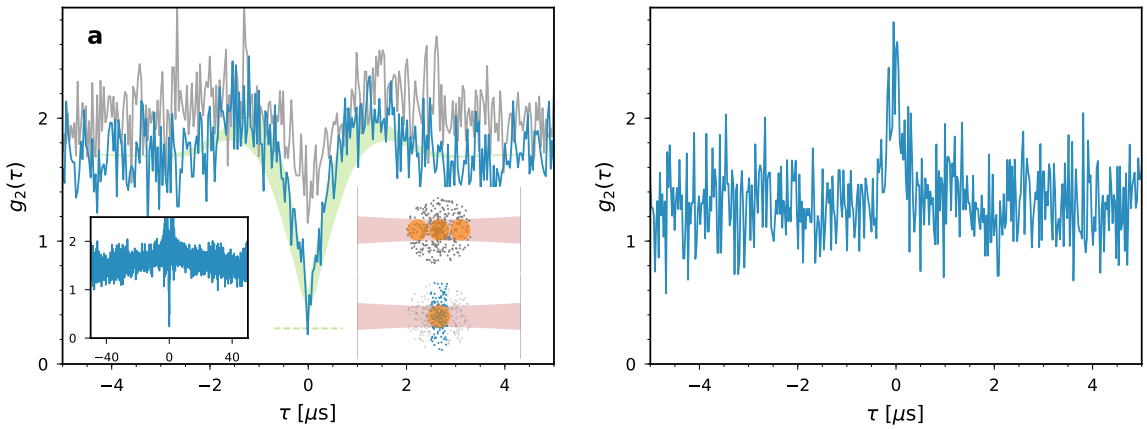

(a) (b)

Figure 6.4: **Polariton blockade in a quantum dot.** **(a)** Strong interactions between polaritons are most clearly indicated by the presence of blockade, suppressing the transport of particles at short timescales. When the cloud is sliced, we observe $g_2(0) = 0.27$ (blue curve), a suppression of five times compared to the long time scale behavior of the autocorrelation function shown in the inset. The green band and green line are a master equation fit [34] and minimum theoretical predicted value (Section 3.6) respectively. The unsliced cloud can support multiple blockade volumes and so its g_2 suppression (grey curve) at zero time is much smaller. **(b)** Probing the two-polariton resonance results in photon bunching. Experimentally, this is done by shifting the resonator resonance by -5 MHz, increasing the control laser frequency by 5 MHz and probing 1 MHz red detuned from the single polariton resonance. $g_2(0)$ is now much greater than 1, indicating that photon pairs now tunnel through the quantum dot.

6.3.1 Weaker Interactions and Photon Bunching

To verify that the observed interactions really come from intracavity polariton interactions and not some other effect we are not accounting for, a few sanity checks are performed. The first is not slicing the cloud before looking at the g_2 function. Since now the cloud can hold approximately three blockade volumes longitudinally, we observe very weak suppression of simultaneous photon tunneling through the quantum dot (shown in Figure 6.4a). Similarly, for the $85S$ Rydberg state, which has a significantly smaller C_6 than the $100S$ state, even a properly sliced cloud only shows a nominal transport suppression; multiple blockade volumes can be supported transversely in this case. Finally, we perform the opposite experiment of

the one that produced blockade: we inject photons with a detuning that accounts for the interaction-driven change in frequency. This results in preferential bunching of photons, since they now prefer to tunnel in pairs (Figure 6.4b).

6.4 Rabi Oscillations and Dark Polariton Saturation

Having only a single resonator modes prevents the photons, and therefore the polaritons, from having transverse dynamics and confines them to at most one dimension. The slicing by itself though is not a guarantee that the polaritons are also longitudinally confined. To explore the dimensionality of the quantum dot, it is probed by short pulses of higher intensity light than the one used for the g_2 measurements. We then observed the ring-up and subsequent ring-down of the cavity. A one-dimensional system that allows for longituninal motion would not be able to contain the excitation as it would travel away before it can removed. On the other hand, in zero dimensions, the drive field would excite and then de-excite the system, since the excitation is trapped and cannot just escape by moving away. Figure 6.5a shows the ring-up and ring-down dynamics of the dark polaritons, exhibiting oscillations between zero and one polaritons at the higher intensities. This is a very strong indication that the quantum dot is supporting zero-dimensional strong interactions within the lifetime of a polariton.

Furthermore, we expect that at high probe intensities, the intracavity dark polariton number should saturate due to interactions. At the same time, any bright polaritons that are off-resonantly excited are linear in probe power, since they are non-interacting particles, and can swamp the signal background. Luckily, they also decay fairly quickly, resulting in a sharp dropoff in the signal of Figure 6.5a, followed by a slower exponential decay due to the remaining dark polaritons. The steady-state dark polariton number can be extrapolated from this slow decay to zero time. The measured saturation value of $n_d = .47$, shown in Figure 6.5b, is indicative of a damped 0D two-level system, while the strong saturation with higher probe powers comes from the strong interactions in the system.

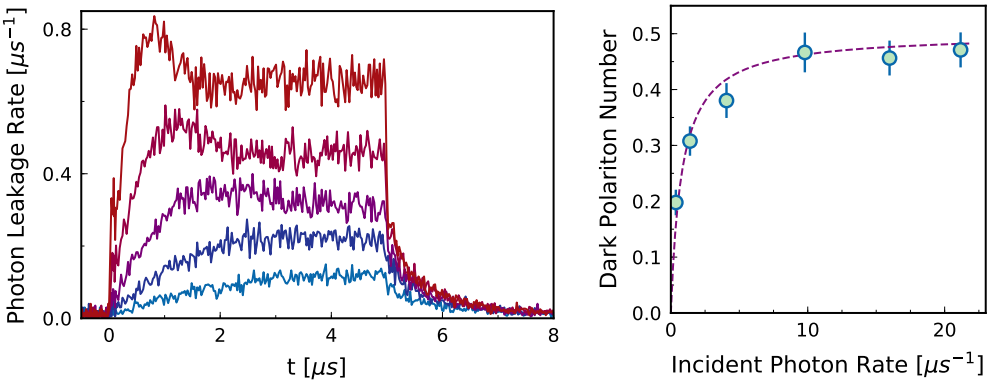

(a) (b)

Figure 6.5: **Ring-up and ring-down dynamics of a quantum dot.** **(a)** When the quantum dot is probed with multiple photons, tunnelling of a single polariton in and out of the dot is coherently stimulated until the dot reaches equilibrium. As the probe power is increased, both the frequency of these oscillations and the transmitted power through the dot increase. Bright polaritons are mostly responsible for this increase in transmission since they do not feel the polaritonic interactions and therefore do no saturate at higher probe strengths. The very fast ring-up (100 ns timescale) indicate off-resonant bright polariton excitation dynamics, while the slow timescale (μs timescale) are a result of the tunnelling between zero and one polaritons inside the dot. The sharp dropoff is due to the fast P-state decay of the bright polaritons, leaving behind the much longer-lived dark polaritons. **(b)** Using the slow exponential decay of the ring-down measurements, we can extrapolate the zero-time number of dark polaritons inside the quantum dot for various probe powers. The dark polariton number saturates to $n_d = 0.47(3)$ at the highest power, consistent with a lossy zero-dimensionaly two-level emitter.

6.5 Summary

Throughout this chapter, I desscribed our efforts to make strongly-interacting cavity Rydberg polaritons and presented evidence of such interactions. By creating a zero-dimensional quantum dot, the particles were confined enough to be within a single blockade volume and preclude more than a single polariton from tunnelling through the dot. The dimensionality of the dot was also shown to produce the correct behavior when multiple photons were injected into the resonator, resulting in damped oscillations and a saturating number of the dark polaritons at higher probe powers.

Combining this system with higher atomic densities and resonator finesse can boost the

OD_B dramatically, paving the way for few-particle synthetic materials and other many-body states [115–117], such as Laughlin puddles and multiple degenerate mode Landau levels. At the same time, strong interactions indicate multiple collision events during the polaritons' lifetime; this is a fundamental requirement for quantum gates [80, 118], making long-lived cavity Rydberg polaritons a promising platform for photonic QIP [119, 120].

CHAPTER 7

CONCLUSION AND OUTLOOK

In this thesis, Rydberg EIT has been employed inside an optical resonator to combine the strong dipole-dipole interactions of Rydberg atoms with the rich dynamics of resonator photons. The properties and interactions of Rydberg atoms were numerically modeled, allowing for easy planning of experimental parameters. At the same time, a formal theory of cavity Rydberg polaritons was developed, along with a numerical renormalized effective field theory for strongly interacting polaritons. This theory agrees very well with full numerics and is extremely timely and important; while it only describes strong interactions in the single-mode regime, it can straightforwardly be extended to many particles and many resonator modes, allowing for true manybody physics modeling.

Experiments were performed on a cold atomic ensemble in the waist of a running-wave four-mirror resonator. The resulting polaritons behaved according to theory, showing properties of both their atomic and photonic constituents. In particular, their frequency follows the cavity detuning but slowed down by a factor of $\cos^2\theta_d$, the photonic part of the polariton. At the same time, both the energy and linewidth of the polariton can be controlled through laser and cavity detunings. Multi-mode EIT was also demonstrated; a resonator designed to have two modes nearly degenerate was used and frequency pulling of the dark polariton resonances was evident in the data. At the same time, no interactions could happen due to the high electric field background causing rapid polariton dephasing.

Once the electric field inside the resonator was controlled, through both passive and active means, and slicing of the atomic cloud, to achieve smaller cloud sizes comparable to the blockade radius of the sample, we managed to observe interactions. This was done by carefully engineering a zero-dimensional quantum dot and recording photons leaking out of the resonator and plotting their temporal correlation. Minimum values of the autocorrelation function $g_2 = 0.27$ were observed, indicating strong suppression of a second simultaneous

excitation inside the resonator. At the same time, we explored Rabi oscillations and a saturation of the dark poalriton number inside the dot, verifying that it is indeed of zero dimensionality.

Combining our strong photonic interactions with more exotic cavities of multiple degenerate modes and non-planar geometries will create the perfect platform to study fractional quantum Hall systems, quantum fluids and emergent crystallization [69, 89, 103, 121, 122]. Cavity Rydberg polaritons are also ripe for applications in quantum information processing [118–120] and quantum repeater protocols [92]. Finally, using strongly-interacting polaritons allows for the exploration of dissipative manybody states [115] and their phase diagrams [89]. At the same time, the fully renormalized effective field theory can be extended to multiple resonator modes and photons to allow for fast, numerical modeling of strongly-correlated quantum states [12, 121], providing the theoretical background for all the experimental realizations that we have unlocked access to through the strongly-interacting cavity Rydberg polaritons.

BIBLIOGRAPHY

1. Bardeen, J., Cooper, L. N. & Schrieffer, J. R. Microscopic theory of superconductivity. *Physical Review* **106,** 162 (1957).

2. Zhang, X., Hung, C.-L., Tung, S.-K. & Chin, C. Quantum critical behavior of ultracold atoms in two-dimensional optical lattices. *arXiv preprint arXiv:1109.0344* (2011).

3. Hung, C.-L., Zhang, X., Gemelke, N. & Chin, C. Observation of scale invariance and universality in two-dimensional Bose gases. *Nature* **470,** 236 (2011).

4. Anderson, M. H., Ensher, J. R., Matthews, M. R., Wieman, C. E. & Cornell, E. A. Observation of Bose-Einstein condensation in a dilute atomic vapor. *Science* **269,** 198–201 (1995).

5. Davis, K. B. *et al.* Bose-Einstein condensation in a gas of sodium atoms. *Physical review letters* **75,** 3969 (1995).

6. Maiman, T. H. *et al.* Stimulated optical radiation in ruby (1960).

7. Boyd, R. W. *Nonlinear optics* (Elsevier, 2003).

8. Kimble, H. J., Dagenais, M. & Mandel, L. Photon antibunching in resonance fluorescence. *Physical Review Letters* **39,** 691 (1977).

9. Freedman, S. J. & Clauser, J. F. Experimental test of local hidden-variable theories. *Physical Review Letters* **28,** 938 (1972).

10. Siegman, A. E. *Lasers* (University Science Books, Mill Valley, CA, 1986).

11. Sommer, A. & Simon, J. Engineering photonic Floquet Hamiltonians through Fabry–Pérot resonators. *New Journal of Physics* **18,** 035008 (2016).

12. Schine, N., Ryou, A., Gromov, A., Sommer, A. & Simon, J. Synthetic Landau levels for photons. *Nature* **534,** 671 (2016).

13. Klaers, J., Schmitt, J., Vewinger, F. & Weitz, M. Bose–Einstein condensation of photons in an optical microcavity. *Nature* **468,** 545 (2010).

14. Horikiri, T. *et al.* High-energy side-peak emission of exciton-polariton condensates in high density regime. *Scientific reports* **6,** 25655 (2016).

15. Maghrebi, M. F. *et al.* Fractional quantum Hall states of Rydberg polaritons. *Physical Review A* **91,** 033838 (2015).

16. Baumann, K., Guerlin, C., Brennecke, F. & Esslinger, T. Dicke quantum phase transition with a superfluid gas in an optical cavity. *Nature* **464,** 1301–1306. ISSN: 0028-0836 (2010).

17. Kollár, A. J. *et al.* Supermode-density-wave-polariton condensation with a Bose–Einstein condensate in a multimode cavity. *Nature communications* **8,** 14386 (2017).

18. Purdy, T. P. *et al.* Tunable cavity optomechanics with ultracold atoms. *Physical review letters* **105,** 133602 (2010).

19. Dudin, Y. & Kuzmich, A. Strongly interacting Rydberg excitations of a cold atomic gas. *Science* **336,** 887–889 (2012).

20. Greiner, M., Mandel, O., Esslinger, T., Hänsch, T. W. & Bloch, I. Quantum phase transition from a superfluid to a Mott insulator in a gas of ultracold atoms. *Nature* **415,** 39 (2002).

21. Vuletić, V., Kerman, A. J., Chin, C. & Chu, S. Observation of low-field Feshbach resonances in collisions of cesium atoms. *Physical Review Letters* **82,** 1406 (1999).

22. Bakr, W. S. *et al.* Probing the Superfluid–to–Mott Insulator Transition at the Single-Atom Level. *Science* **329,** 547–550 (2010).

23. Cheuk, L. W. *et al.* Quantum-gas microscope for fermionic atoms. *Physical review letters* **114,** 193001 (2015).

24. Schauß, P. *et al.* Observation of spatially ordered structures in a two-dimensional Rydberg gas. *Nature* **491,** 87 (2012).

25. Leibfried, D. *et al.* Creation of a six-atom 'Schrödinger cat'state. *Nature* **438,** 639 (2005).

26. Isenhower, L. *et al.* Demonstration of a neutral atom controlled-NOT quantum gate. *Physical review letters* **104,** 010503 (2010).

27. Weimer, H., Löw, R., Pfau, T. & Büchler, H. P. Quantum critical behavior in strongly interacting Rydberg gases. *Physical Review Letters* **101,** 250601 (2008).

28. Peyronel, T. *et al.* Quantum nonlinear optics with single photons enabled by strongly interacting atoms. *Nature* **488,** 57 (2012).

29. Weatherill, K. *et al.* Electromagnetically induced transparency of an interacting cold Rydberg ensemble. *Journal of Physics B: Atomic, Molecular and Optical Physics* **41,** 201002 (2008).

30. Bienias, P. *et al.* Scattering resonances and bound states for strongly interacting Rydberg polaritons. *Physical Review A* **90,** 053804 (2014).

31. Pritchard, J. D. *et al.* Cooperative atom-light interaction in a blockaded Rydberg ensemble. *Physical Review Letters* **105,** 193603 (2010).

32. Fleischhauer, M., Otterbach, J. & Unanyan, R. G. Bose-Einstein condensation of stationary-light polaritons. *Physical review letters* **101,** 163601 (2008).

33. Firstenberg, O. *et al.* Attractive photons in a quantum nonlinear medium. *Nature* **502,** 71 (2013).

34. Jia, N. *et al.* A strongly interacting polaritonic quantum dot. *Nature Physics* (2018).

35. Rydberg, J. XXXIV. On the structure of the line-spectra of the chemical elements. *The London, Edinburgh, and Dublin Philosophical Magazine and Journal of Science* **29,** 331–337 (1890).

36. Bohr, N. I. On the constitution of atoms and molecules. *The London, Edinburgh, and Dublin Philosophical Magazine and Journal of Science* **26,** 1–25 (1913).

37. Schrödinger, E. An undulatory theory of the mechanics of atoms and molecules. *Physical review* **28,** 1049 (1926).

38. Gallagher, T. F. *Rydberg atoms* (Cambridge University Press, 2005).

39. Li, W., Mourachko, I., Noel, M. & Gallagher, T. Millimeter-wave spectroscopy of cold Rb Rydberg atoms in a magneto-optical trap: Quantum defects of the ns, np, and nd series. *Physical Review A* **67,** 052502 (2003).

40. Han, J., Jamil, Y., Norum, D., Tanner, P. J. & Gallagher, T. Rb n f quantum defects from millimeter-wave spectroscopy of cold Rb 85 Rydberg atoms. *Physical Review A* **74,** 054502 (2006).

41. Marinescu, M., Sadeghpour, H. & Dalgarno, A. Dispersion coefficients for alkali-metal dimers. *Physical Review A* **49,** 982 (1994).

42. Theodosiou, C. E. Lifetimes of alkali-metal—atom Rydberg states. *Physical Review A* **30,** 2881 (1984).

43. Noumerov, B. A method of extrapolation of perturbations. *Monthly Notices of the Royal Astronomical Society* **84,** 592–592 (1924).

44. Numerov, B. Note on the numerical integration of $d^2x/dt^2 = f(x, t)$. *Astronomische Nachrichten* **230,** 359–364 (1927).

45. Zimmerman, M. L., Littman, M. G., Kash, M. M. & Kleppner, D. Stark structure of the Rydberg states of alkali-metal atoms. *Physical Review A* **20,** 2251 (1979).

46. Hoogenraad, J. & Noordam, L. Rydberg atoms in far-infrared radiation fields. I. Dipole matrix elements of H, Li, and Rb. *Physical Review A* **57,** 4533 (1998).

47. Tauschinsky, A., Newell, R., van den Heuvell, H. v. L. & Spreeuw, R. Measurement of ^{87}Rb Rydberg-state hyperfine splitting in a room-temperature vapor cell. *Physical Review A* **87,** 042522 (2013).

48. Deiglmayr, J. *et al.* Coherent excitation of Rydberg atoms in an ultracold gas. *Optics communications* **264,** 293–298 (2006).

49. O'sullivan, M. & Stoicheff, B. Scalar polarizabilities and avoided crossings of high Rydberg states in Rb. *Physical Review A* **31,** 2718 (1985).

50. Jackson, J. D. *Classical electrodynamics* 1999.

51. Flannery, M., Vrinceanu, D. & Ostrovsky, V. Long-range interaction between polar Rydberg atoms. *Journal of Physics B: Atomic, Molecular and Optical Physics* **38,** S279 (2005).

52. Singer, K. *et al.* Spectroscopy of an ultracold Rydberg gas and signatures of Rydberg–Rydberg interactions. *Journal of Physics B: Atomic, Molecular and Optical Physics* **38,** S321 (2005).

53. Reinhard, A., Liebisch, T. C., Knuffman, B. & Raithel, G. Level shifts of rubidium Rydberg states due to binary interactions. *Physical Review A* **75,** 032712 (2007).

54. Stormer, H. L., Tsui, D. C. & Gossard, A. C. The fractional quantum Hall effect. *Reviews of Modern Physics* **71,** S298 (1999).

55. Houck, A. A., Türeci, H. E. & Koch, J. On-chip quantum simulation with superconducting circuits. *Nature Physics* **8,** 292 (2012).

56. Anderson, B. M., Ma, R., Owens, C., Schuster, D. I. & Simon, J. Engineering topological many-body materials in microwave cavity arrays. *Physical Review X* **6,** 041043 (2016).

57. Roushan, P. *et al.* Chiral ground-state currents of interacting photons in a synthetic magnetic field. *Nature Physics* **13,** 146 (2017).

58. Tsui, D. C., Stormer, H. L. & Gossard, A. C. Two-dimensional magnetotransport in the extreme quantum limit. *Physical Review Letters* **48,** 1559 (1982).

59. Deng, H., Haug, H. & Yamamoto, Y. Exciton-polariton bose-einstein condensation. *Reviews of Modern Physics* **82,** 1489 (2010).

60. Dean, C. R. *et al.* Boron nitride substrates for high-quality graphene electronics. *Nature Nanotechnology* **5,** 722 (2010).

61. Inouye, S. *et al.* Observation of Feshbach resonances in a Bose–Einstein condensate. *Nature* **392,** 151 (1998).

62. Schreier, J. *et al.* Suppressing charge noise decoherence in superconducting charge qubits. *Physical Review B* **77,** 180502 (2008).

63. Schuster, D. *et al.* Resolving photon number states in a superconducting circuit. *Nature* **445,** 515 (2007).

64. Underwood, D. L., Shanks, W. E., Koch, J. & Houck, A. A. Low-disorder microwave cavity lattices for quantum simulation with photons. *Physical Review A* **86,** 023837 (2012).

65. Owens, C. *et al.* Quarter-flux Hofstadter lattice in a qubit-compatible microwave cavity array. *Physical Review A* **97,** 013818 (2018).

66. Fitzpatrick, M., Sundaresan, N. M., Li, A. C., Koch, J. & Houck, A. A. Observation of a dissipative phase transition in a one-dimensional circuit QED lattice. *Physical Review X* **7,** 011016 (2017).

67. Carroll, T. J., Claringbould, K., Goodsell, A., Lim, M. & Noel, M. W. Angular dependence of the dipole-dipole interaction in a nearly one-dimensional sample of Rydberg atoms. *Physical Review Letters* **93,** 153001 (2004).

68. Gorshkov, A. V., Otterbach, J., Fleischhauer, M., Pohl, T. & Lukin, M. D. Photon-photon interactions via Rydberg blockade. *Physical Review Letters* **107,** 133602 (2011).

69. Sommer, A., Büchler, H. P. & Simon, J. Quantum crystals and Laughlin droplets of cavity Rydberg polaritons. *arXiv:1506.00341* (2015).

70. Parigi, V. *et al.* Observation and measurement of interaction-induced dispersive optical nonlinearities in an ensemble of cold Rydberg atoms. *Physical Review Letters* **109,** 233602 (2012).

71. Stanojevic, J., Parigi, V., Bimbard, E., Ourjoumtsev, A. & Grangier, P. Dispersive optical nonlinearities in a Rydberg electromagnetically-induced-transparency medium. *Physical Review A* **88,** 053845 (2013).

72. Ningyuan, J. *et al.* Observation and characterization of cavity Rydberg polaritons. *Physical Review A* **93,** 041802 (2016).

73. Gullans, M. *et al.* Effective field theory for Rydberg polaritons. *Physical Review Letters* **117,** 113601 (2016).

74. Gorshkov, A. V., André, A., Lukin, M. D. & Sørensen, A. S. Photon storage in Λ-type optically dense atomic media. II. Free-space model. *Physical Review A* **76,** 033805 (2007).

75. Lukin, M. *et al.* Dipole blockade and quantum information processing in mesoscopic atomic ensembles. *Physical Review Letters* **87,** 037901 (2001).

76. Litinskaya, M., Tignone, E. & Pupillo, G. Cavity polaritons with Rydberg blockade and long-range interactions. *Journal of Physics B: Atomic, Molecular and Optical Physics* **49,** 164006 (2016).

77. Grankin, A. *et al.* Quantum statistics of light transmitted through an intracavity Rydberg medium. *New Journal of Physics* **16,** 043020 (2014).

78. Fleischhauer, M., Imamoglu, A. & Marangos, J. P. Electromagnetically induced transparency: Optics in coherent media. *Reviews of Modern Physics* **77,** 633 (2005).

79. Cohen-Tannoudji, C., Dupont-Roc, J. & Grynberg, G. *Atom-photon interactions: basic processes and applications* (Wiley-VCH, New York, 1998).

80. Saffman, M., Walker, T. G. & Mølmer, K. Quantum information with Rydberg atoms. *Reviews of Modern Physics* **82,** 2313 (2010).

81. Sommer, A. & Simon, J. Engineering photonic Floquet Hamiltonians through Fabry-Pérot resonators. *New Journal of Physics* **18,** 035008. ISSN: 1367-2630 (2016).

82. Schine, N., Chalupnik, M., Can, T., Gromov, A. & Simon, J. Measuring Electromagnetic and Gravitational Responses of Photonic Landau Levels. *arXiv:1802.04418* (2018).

83. Simon, J. *Cavity QED with atomic ensembles* (Harvard University, 2010).

84. Ketterle, W., Durfee, D. S. & Stamper-Kurn, D. Making, probing and understanding Bose-Einstein condensates. *arXiv:cond-mat/9904034* (1999).

85. Goodman, J. W. *Introduction to Fourier optics* (Roberts and Company Publishers, Englewood, CO, 2005).

86. Dutta, S. & Mueller, E. J. Coherent generation of photonic fractional quantum Hall states in a cavity and the search for anyonic quasiparticles. *arXiv preprint arXiv:1711.08059* (2017).

87. Umucalılar, R. O. & Carusotto, I. Fractional Quantum Hall States of Photons in an Array of Dissipative Coupled Cavities. *Physical Review Letters* **108** (2012).

88. Ivanov, P. A., Letscher, F., Simon, J. & Fleischhauer, M. Adiabatic flux insertion and growing of Laughlin states of cavity Rydberg polaritons. *arXiv preprint arXiv:1803.04156* (2018).

89. Grusdt, F. & Fleischhauer, M. Fractional quantum Hall physics with ultracold Rydberg gases in artificial gauge fields. *Physical Review A* **87,** 043628 (2013).

90. Grankin, A., Grangier, P. & Brion, E. Diagrammatic treatment of few-photon scattering from a Rydberg blockaded atomic ensemble in a cavity. *arXiv:1803.09480* (2018).

91. Han, Y., He, B., Heshami, K., Li, C.-Z. & Simon, C. Quantum repeaters based on Rydberg-blockade-coupled atomic ensembles. *Physical Review A* **81,** 052311 (2010).

92. Das, S. *et al.* Photonic controlled-phase gates through Rydberg blockade in optical cavities. *Physical Review A* **93,** 040303 (2016).

93. Koch, C. P., Kosloff, R. & Masnou-Seeuws, F. Short-pulse photoassociation in rubidium below the D 1 line. *Physical Review A* **73,** 043409 (2006).

94. Mullins, T. *et al.* Photoassociation and coherent transient dynamics in the interaction of ultracold rubidium atoms with shaped femtosecond pulses. I. Experiment. *Physical Review A* **80,** 063416 (2009).

95. Kojima, K., Kyuma, K. & Nakayama, T. Analysis of the spectral linewidth of distributed feedback laser diodes. *Journal of lightwave technology* **3,** 1048–1055 (1985).

96. Gehm, M., O'hara, K., Savard, T. & Thomas, J. Dynamics of noise-induced heating in atom traps. *Physical Review A* **58,** 3914 (1998).

97. Weiss, D. S., Riis, E., Shevy, Y., Ungar, P. J. & Chu, S. Optical molasses and multilevel atoms: experiment. *JOSA B* **6,** 2072–2083 (1989).

98. Ungar, P. J., Weiss, D. S., Riis, E. & Chu, S. Optical molasses and multilevel atoms: theory. *JOSA B* **6,** 2058–2071 (1989).

99. Dalibard, J. & Cohen-Tannoudji, C. Laser cooling below the Doppler limit by polarization gradients: simple theoretical models. *JOSA B* **6,** 2023–2045 (1989).

100. O'brien, J. L., Furusawa, A. & Vučković, J. Photonic quantum technologies. *Nature Photonics* **3,** 687 (2009).

101. Gorshkov, A. V., Otterbach, J., Fleischhauer, M., Pohl, T. & Lukin, M. D. Photon-photon interactions via Rydberg blockade. *Physical Review Letters* **107,** 133602 (2011).

102. Lukin, M. D. Colloquium: Trapping and manipulating photon states in atomic ensembles. *Reviews of Modern Physics* **75,** 457–472 (2003).

103. Umucalılar, R., Wouters, M. & Carusotto, I. Probing few-particle Laughlin states of photons via correlation measurements. *Physical Review A* **89,** 023803 (2014).

104. Lukin, M. D., Fleischhauer, M., Scully, M. O. & Velichansky, V. L. Intracavity electromagnetically induced transparency. *Optics letters* **23,** 295–297 (1998).

105. Hattermann, H. *et al.* Detrimental adsorbate fields in experiments with cold Rydberg gases near surfaces. *Physical Review A* **86** (2012).

106. Chang, D. E. *et al.* Crystallization of strongly interacting photons in a nonlinear optical fibre. *Nature Physics* **4,** 884–889. ISSN: 1745-2473 (2008).

107. Gopalakrishnan, S., Lev, B. L. & Goldbart, P. M. Emergent crystallinity and frustration with Bose–Einstein condensates in multimode cavities. *Nature Physics* **5,** 845–850. ISSN: 1745-2473 (2009).

108. Otterbach, J., Moos, M., Muth, D. & Fleischhauer, M. Wigner Crystallization of Single Photons in Cold Rydberg Ensembles. *Physical Review Letters* **111** (2013).

109. Kollár, A. J., Papageorge, A. T., Baumann, K., Armen, M. A. & Lev, B. L. An adjustable-length cavity and Bose–Einstein condensate apparatus for multimode cavity QED. *New Journal of Physics* **17,** 043012 (2015).

110. Ryou, A. *Designing, Probing, and Stabilizing Exotic Fabry-Perot Cavities for Studying Strongly Correlated Light* PhD thesis (The University of Chicago, 2017).

111. Mohapatra, A., Jackson, T. & Adams, C. Coherent optical detection of highly excited Rydberg states using electromagnetically induced transparency. *Physical review letters* **98,** 113003 (2007).

112. Goban, A. *et al.* Atom–light interactions in photonic crystals. *Nature communications* **5,** 3808 (2014).

113. Thompson, J. D. *et al.* Coupling a single trapped atom to a nanoscale optical cavity. *Science* **340,** 1202–1205 (2013).

114. Goban, A. *et al.* Superradiance for atoms trapped along a photonic crystal waveguide. *Physical review letters* **115,** 063601 (2015).

115. Hafezi, M., Adhikari, P. & Taylor, J. Chemical potential for light by parametric coupling. *Physical Review B* **92,** 174305 (2015).

116. Ma, R., Owens, C., Houck, A., Schuster, D. I. & Simon, J. Autonomous stabilizer for incompressible photon fluids and solids. *Physical Review A* **95,** 043811 (2017).

117. Lebreuilly, J., Wouters, M. & Carusotto, I. Towards strongly correlated photons in arrays of dissipative nonlinear cavities under a frequency-dependent incoherent pumping. *Comptes Rendus Physique* **17,** 836–860 (2016).

118. Jaksch, D. *et al.* Fast quantum gates for neutral atoms. *Physical Review Letters* **85,** 2208 (2000).

119. Brion, E., Carlier, F., Akulin, V. & Mølmer, K. Quantum repeater with Rydberg-blocked atomic ensembles in fiber-coupled cavities. *Physical Review A* **85,** 042324 (2012).

120. Zhao, B., Müller, M., Hammerer, K. & Zoller, P. Efficient quantum repeater based on deterministic Rydberg gates. *Physical Review A* **81,** 052329 (2010).

121. Carusotto, I. & Ciuti, C. Quantum fluids of light. *Reviews of Modern Physics* **85,** 299 (2013).

122. Bienias, P. Few-body quantum physics with strongly interacting Rydberg polaritons. *The European Physical Journal Special Topics* **225,** 2957–2976 (2016).